Development of a medium-high throughput electrophysiology method to study cellular heterogeneity in the rabbit heart

Quentin Lachaud
BSc (Hons), MRes

Submitted in fulfilment of the requirements for the degree of Doctor of Philosophy

October 2019

Institute of Cardiovascular and Medical Sciences
College of Medical, Veterinary and Life Sciences
University of Glasgow

Abstract

Sudden cardiac death (SCD) is a prominent cause of death worldwide today, mainly occurring as a result of coronary heart disease, cardiomyopathies, and inherited or induced arrhythmia syndromes. Survival following sudden cardiac arrest (SCA) has improved in the past decades, but the majority of cases of SCD remain unwitnessed. Although advances have been made towards the investigation of the mechanisms behind SCD, it remains a poorly understood phenomenon. Environmental factors have been identified and associated with increased arrhythmic risk, and most prominently, drug-induced arrhythmias constitute a serious hurdle to both cardiac and non-cardiac drug development. The past decade has seen pro-arrhythmic screening of new compounds become routine, and develop into a major point of interest for drug development. Specifically, the onset of drug-induced polymorphic ventricular tachycardia, such as torsade de pointes (TdP), is of particular interest to cardiac research. The concept of electrophysiological heterogeneity in cardiac muscle holds exciting potential for explaining the pathophysiology of TdP, but quantifying cellular heterogeneity using conventional methods is a challenge.

This work developed and refined a fluorescence-based, medium/high-throughput electrophysiological assay to process large cell populations (~50-500 cells) from single hearts. Using this novel approach, transmural electrophysiological differences were found between regions of individual hearts, replicating published work with a 3 to 4-fold reduction in hearts sampled, and additionally providing a previously unknown quantification of cellular heterogeneity in isolated cardiomyocyte populations, in both healthy and failing rabbit hearts.

Further classification of electrophysiological differences within smaller regions of the ventricle yielded evidence of repolarisation gradients across the myocardium, with vast overlap in repolarisation duration, challenging the dogma of region-specific repolarisation duration. Lastly, by specifically blocking hERG channels and L-type calcium channels in cardiac subregions (sub-epicardial apex and base) strong evidence was found for heterogeneous electrophysiology response amongst isolated cell populations. Specifically, sub-epicardial action potential shortening using nifedipine was strongly APD dependent, whereby baseline AP duration determined the extent of APD shortening via drug-induced $I_{Ca\text{-}L}$ blockade. Sub-epicardial AP prolongation mediated via IKr block using dofetilide also

produced non-homogeneous cell response in the form of two distinct population responses: (i) The majority (~85%) was made up of normal responding cells, experiencing ~20-30ms AP prolongation not dependent on baseline APD ($P<0.001$), and (ii) hyper-responding cells (~15% of total) experiencing >100ms AP prolongation, beyond the pacing cycle length (>500ms) without any evidence of early-afterdepolarisations.

Large experimental samples of AP parameters gathered in this study can provide real-world data parameter space ranges for mathematical model development, showing that ion channel conductance ranges used today to predict drug responses at the organ level may be too restrictive, or inaccurate. Iterative model adjustment using large experimental datasets can help constrain models and improve their predictive power, saving time by reducing computational power required.

Table of contents

List of Tables

List of figures

Acknowledgements

Congratulations. Your careless hands are currently holding the meticulously assembled, compacted amalgamation of my work over the past four years. Although there are more stars in our solar system than there will ever be voluntary readers of this thesis, I hope you find in it what you are looking for, nonetheless.

In the beginning Godfrey created the grant and the project.
And the PhD was without form and void, for the work was yet to come.
And Godfrey said, "Let there be data."
And there was data. And Godfrey saw that it was good.
He separated the signal from the noise, and assessed the statistical significance.
And it was so.
And on the fourth year Godfrey said unto Quentin, be fruitful and produce thy thesis.
And Godfrey saw all that Quentin had made. And it was good.

Aside from the above silliness, I would like to express endless gratitude toward Professor Godfrey Smith for the continuous support over my entire project, and beyond. A huge thanks to Dr Niall MacQuaide and Dr Francis Burton, for the patient help, advice and explanations, and more reasons than I can enumerate here. My infinite gratitude to Aileen Rankin and Michael Dunne, who aside from keeping the entire lab afloat (a trivial task), cunningly made use of sarcasm and second degree to add that bit of spice to an otherwise potentially lethally monotonous laboratory experience.

What could these past years have been without Sara and Eline endlessly presenting me with opportunities to correct hilarious English. Between "leunch" and the daily (circa 10.43am) hiccupping, not one second has been dull. Sara, you have been the least boring lab partner I could have imagined. I also want to thank you for helping me understand how some situations justify fratricide.

Finally, in the most flagrant of clichés, I say with complete honestly that I would not have completed this thing had it not been for Adriana. You are my rock, and the most dependable, unconditionally loving, compassionate, and smartest person I have ever met. Thank you for everything you have done this past decade. My turn.

Ad meliora

Publications and abstracts

Sala, L. et al. (2017) 'NEW METHODS IN CARDIOVASCULAR BIOLOGY MUSCLEMOTION : A Versatile Open Software Tool to Quantify Cardiomyocyte and Cardiac Muscle Contraction In Vitro and In Vivo', (November). doi: 10.1161/CIRCRESAHA.117.312067.

Conference posters

Lachaud, Q., MacQuaide, N., Burton, F., Smith, G. 'High-throughput Study of Rabbit Ventricle Action Potential Populations in MI Model', Biophysical Journal 114(3):625a. (February 2018). Doi: 10.1016/j.bpj.2017.11.3377.

Lachaud, Q., MacQuaide, N., Burton, F., Smith, G. 'High-Throughput Characterisation of Action Potential Characteristics in Isolated Cardiomyocyte Populations of the Rabbit MI Model', EWGCCE Meeting (June 2017)

Author’s declarations

All surgical procedures on rabbits, as well as enzymatic cell isolation were performed by technical staff (Mrs Aileen Rankin and Mr Michael Dunne). Metal work related to the manufacture of the temperature regulating plate was carried out by Ms Julie Magill. Computer code (R) for cell and heart variation effect on population variation was written by Dr Francis Burton. I declare that all experimental work is my own and has not, in whole or in part, been submitted for any other degree.

Abbreviations

$[Ca^{2+}]_i$	Intracellular calcium concentration
AF	Atrial fibrillation
AM	Acetoxymethyl ester
AP	Action Potential
APD	Action potential duration
APD_{30}	Action Potential Duration at 30% Repolarisation
APD_{75}	Action Potential Duration at 75% Repolarisation
APD_{90}	Action Potential Duration at 90% Repolarisation
AVN	Atrio-ventricular node
BDM	2,3-butanedione monoxime
BSA	Bovine serum albumin
CHD	Coronary heart disease
CICR	Ca_{2+} induced Ca_{2+} release
cLQTS	Congenital long-QT syndrome
CM	Cardiomyocyte
DAD	Delayed afterdepolarisations
di-4-ANEPPS	di-4-butyl-amino-naphthyl-ethylene-pyridinium propyl-sulfonate
diLQTS	Drug-induced long-QT syndrome
DMSO	Dimethyl sulphoxide
Dn90	90% of sarcomere length relaxation
EAD	Early afterdepolarisations
E-C	Excitation-contraction
E_m	Membrane potential
EMA	European Medicines Agency
ERP	Effective repolarisation period
FDA	Food and Drug Administration
FOV	Field of view
FS	Fractional shortening

hERG	human *Ether-à-go-go*-Related Gene
HR	Heart rate
$I_{Ca\text{-}L}$	L-type Ca^{2+} current
I_{KATP}	ATP-Sensitive K^{+} current
I_{Kr}	Inward rectifier K^{+} current (rapid)
I_{Ks}	Slow delayed rectifier K^{+} current
I_{Na}	Sodium current
I_{to}	Transient-outward K^{+} channel
LAD	Left anterior descending artery
LED	Light-emitting diode
LTCC	L-type Ca^{2+} channel
LV	Left ventricle
NA	Numerical aperture
NCX	Na^{+}/Ca^{2+} exchanger
PMT	Photomultiplier tube
PRRP	Post repolarisation refractory period
ROS	Reactive oxygen species
RT	Room temperature
RV	Right Ventricle
RyRs	Ryanodine receptors
SA	Sino-Atrial
SCD	Sudden cardiac death
SERCA	Sarco-Endoplasmic Reticulum Ca^{2+}-ATPase
SNR	Signal-to-noise
SR	Sarcoplasmic reticulum
SV	Stroke volume
TdP	Torsade de pointes
TRise	Upstroke time (ms) from 10% to 90% depolarisation
TTP	Time to peak contraction
UP_{90}	Time to 90% contraction

VF	Ventricular fibrillation
V_m	Membrane voltage
WD	Working distance

Chapter 1: Introduction

1.1 Cardiovascular disease and sudden cardiac death (SCD)

Cardiovascular disease (CVD) is the most common cause of death in industrialised countries (Chappex et al., 2015). As the incidence of obesity, diabetes, and coronary heart disease continues to rise, an increase in the rate of sudden cardiac death (SCD), from complications of coronary disease and heart failure is almost inevitable (Okrainec et al. 2004; Chugh et al. 2008). A limited understanding of fatal arrhythmogenesis has driven research into the mechanisms of SCD caused by congenital heart diseases (Myerburg, 2002), and despite extensive insights gained in the past 30 years, remains extremely challenging to predict or prevent (Myerburg and Junttila, 2012). Additionally, congenital heart disease has also been increasing in prevalence in the past few decades (Khairy, 2016), shifting from a previously paediatric to a predominantly adult demographic (2:1) in the past 10 years, due to increased survival (Marelli et al., 2014). Adults with congenital heart disease are highly prone to arrhythmic anomalies, due to genetic anomalies, as well as scarring, tissue hypoxia and other malformations in the heart conduction system (Khairy et al., 2014). Lastly, SCD prevalence in athletes, whereby otherwise healthy individuals suffer a sudden and unexplained cardiac arrest demands further research into the mechanisms underlying lethal ventricular arrhythmias.

1.2 Cardiac function

1.2.1 Excitation-Contraction coupling

The propagation of electrical activation throughout the myocardium is carried by the action potential. Its shape and duration vary across excitable tissues of the heart, most notably between atrium and ventricles (Figure 1.1). To result in a coordinated muscular contraction expelling blood efficiently, the electrical activation must be coordinated throughout the heart muscle in a spatially and temporally precise way. Activation initiates in the sinoatrial node (SAN) from specialized pacemaker cells and propagates through the atrial tissue. The atrium and ventricles are electrically isolated from one another, ensuring atrial contraction always precedes ventricular contraction. The signal reaches the atrioventricular node (AVN), which in turn relays the impulse through the His-Purkinje system in the heart septum. The inward-facing surface (endocardium) of the ventricles is activated, propagating the signal

transmurally via gap junctions outward to the outer surface (epicardium), resulting in co-ordinated ventricular contraction (systole).

The summated electrical activity of the heart can be observed externally by placing electrodes on the chest and limbs (i.e. 12-lead electrocardiogram) (Figure 1.1). On the ECG trace, the P-wave is caused by the depolarising atria, closely followed by the QRS complex, representing ventricular depolarisation. The T-wave shows the repolarising phase of the ventricles, allowing for K^+ to exit the cells and calcium to unbind, resulting in muscle relaxation (diastole). The QT-interval duration is used as a marker of normal ventricular function. As discussed later, a change, generally positive, in the QT interval duration is a valuable indicator of altered electrical ventricular function, which can result from a change in regulatory proteins and/or ion channel transport and expression, in both acquired and inherited disease (Bartos, Grandi and Ripplinger, 2015).

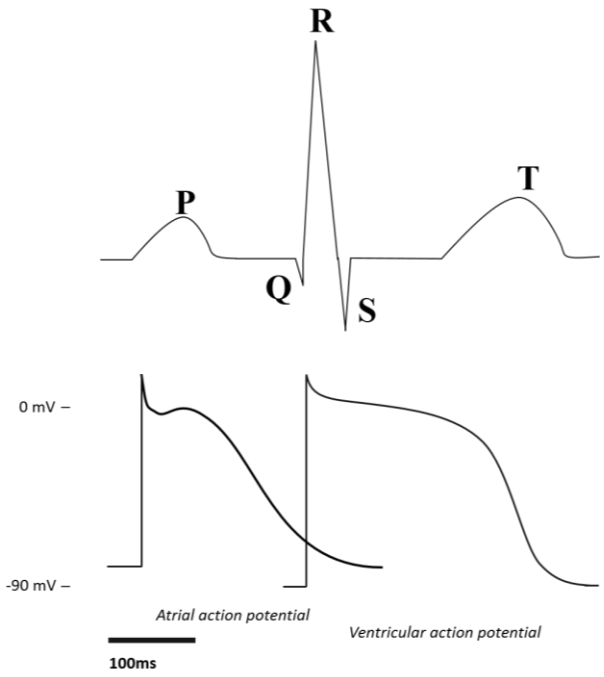

Figure 1.1 Diagrammatic representation of a cardiac electrocardiogram (ECG) demonstrating the respective influence of atrial and ventricular action potentials to the P-wave, and QRS complex + T-wave, respectively.

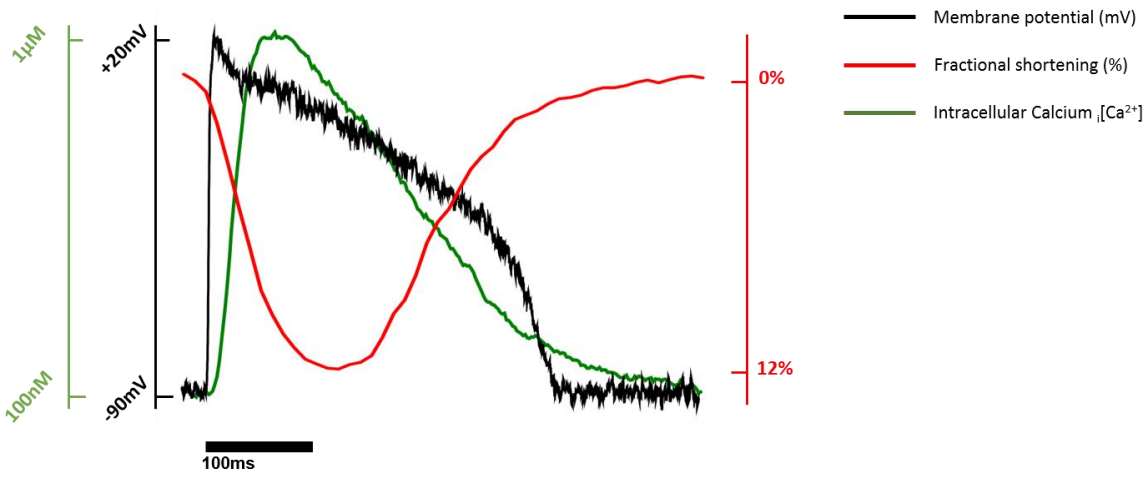

Figure 1.2 Excitation-contraction coupling Example fluorescent signals showing membrane potential (black), Ca^{2+} (green) and sarcomere length overlaid on the same timescale, demonstrating the synergistic relationship between cellular excitation (AP upstroke), Ca^{2+} release, and muscle contraction (cell shortening) contributing to excitation-contraction coupling. (Signals were recorded from a single isolated rabbit ventricular cardiomyocyte)

1.2.2 The ventricular action potential

The action potential is composed of 5 major phases (0-4) shown in Figure 1.3, each phase is the result of a delicate balance of ionic currents caused by ion channels, dynamically controlling the membrane potential (E_m) of the cell.

The duration of an action potential hinges on the balance between inward and outward ionic currents. The voltage-gated Na+ channel mediates phase 0 through rapid activation and de-activation. Phase 1 mediates rapid repolarisation by two components of the transient outward K+ channels ($I_{to,f}$; fast, and $I_{to,s}$; slow). Phase 2 and 3 are the product of competition between inward currents voltage-gated L-type channels and the Na+/Ca^{2+} exchanger (NCX), and outward K+ currents mediated by the voltage-gated delayed rectifier K+ channels, I_K (Carmeliet, 1999).

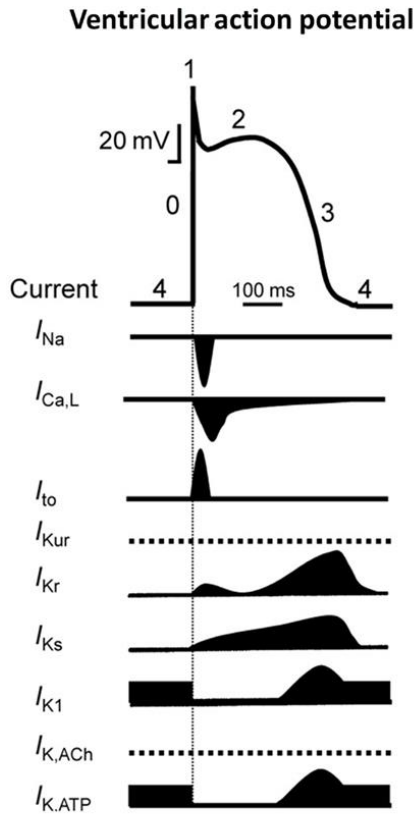

Figure 1.3 Ventricular action potential AP diagram and associated inward (Na^+, Ca^{2+}) and outward (K^+) currents activation and deactivation patterns over the time-course of the action potential. (Diagram taken from Jost, 2009).

The hERG potassium channel was the primary channel of interest in this work, responsible for the dominant component of action potential duration, mediated by the rapid component of the delayed rectifier K+ current (IKr).

1.2.3 Regional electrical differences

The heart is composed of structurally and physiologically distinct regions of myocardium. These are divided in several categories, which can be roughly divided along planes. These respectively separate: atria from ventricles, right- from left-ventricle, apex from base, or transmurally, endocardium from epicardium. Amongst these divisions, the nodal cell (SAN and AVN) electrophysiology differs most markedly from the rest, in that they depolarise spontaneously and drive the intrinsic rhythm of the heart without requiring external activation. Atrial and ventricular action potentials also differ from one another both in AP morphology and duration (see Figure 1.4 and Figure 1.6). The ion channels responsible for these differences are predominantly the voltage-gated Na^+ channels, (Na_v), and K^+ channels (K_v), resulting in a faster upstroke (phase 0) and a longer plateau phase (phase 2) in ventricle cells compared with atrial cells. Different AP morphologies have been identified within the ventricle itself. For example, cells originating from the epicardium of the LV have been shown to have longer action potentials than endocardial LV cells, which may be due to different expressions of K^+ channels (Schram *et al.*, 2002). This endocardium/epicardium difference has already been demonstrated (McIntosh *et al.*, 1998).

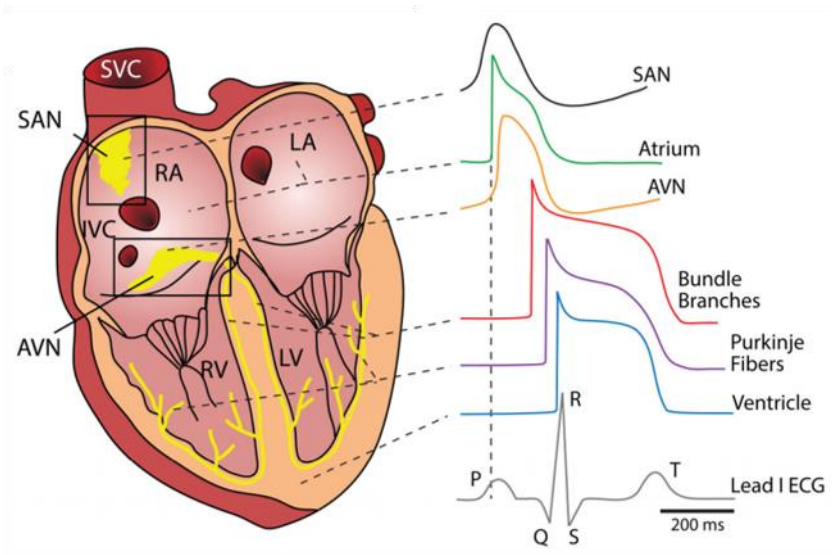

Figure 1.4 Cardiac action potential subtypes Diagrammatic representation of the types of AP duration and morphologies across the major cardiac tissues (Taken from Bartos, Grandi and Ripplinger, 2015).

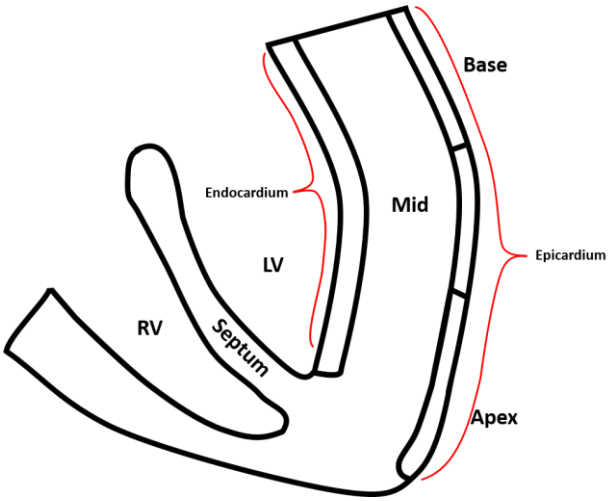

Figure 1.5 Cardiac regions studied in this work Diagram of the left-ventricular regional sub-division which were electrophysiologically compared in this work.

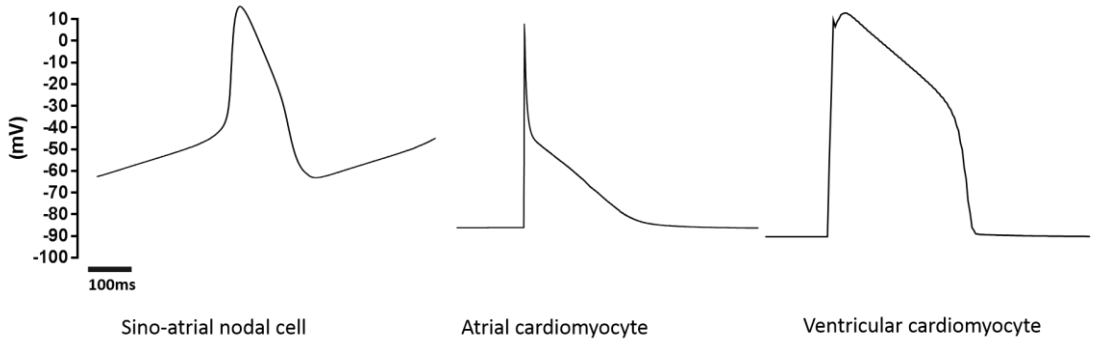

Figure 1.6 Action potentials from SA node, atrium and ventricle of rabbit Example action potential shapes of nodal cell, atrial and ventricular cardiomyocytes generated using the APSim program written by Dr John Dempster. Respective cell models from: (Dokos, Celler and Lovell, 1996; Inada *et al.*, 2009; Davies *et al.*, 2012).

The varying expression and function of ion channels in different regions of the heart strongly drives AP duration and morphology (see Figure 1.7). In the intact heart, action potential heterogeneity is greatly reduced at a local scale by cellular coupling via connexins. In isolated cells, cell-specific channel expression becomes the main driver of AP duration, displaying heterogeneity far exceeding that of coupled tissue. This inherent variation is thought to contribute to the stabilisation of the action potential duration, and in turn of the repolarisation reserve. Down- or mis-regulation of these stabilising currents has been shown to increase the incidence of arrhythmic events (Pogwizd et al., 2001).

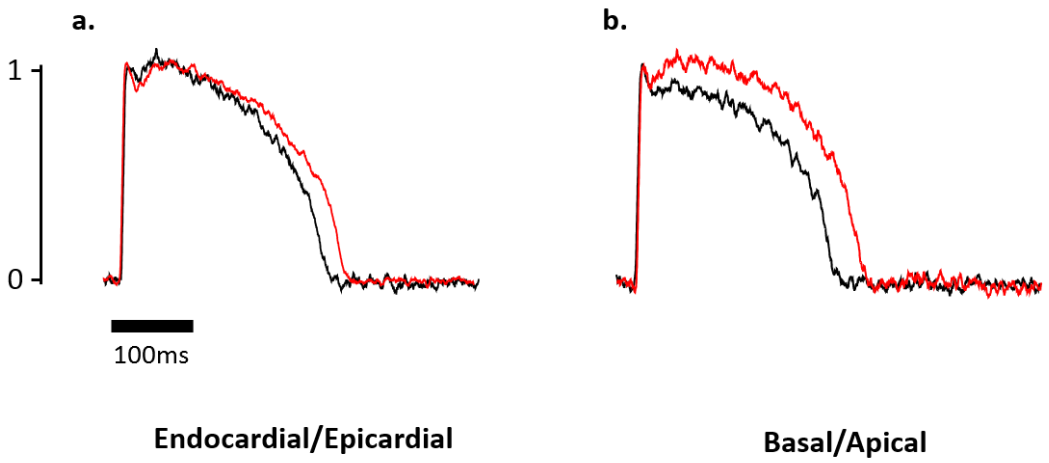

Figure 1.7 Transmural and apicobasal action potentials Example single cell traces of recorded fluorescent action potentials originating from different regions of the heart (acquired in this thesis, and normalised to upstroke maximum). (a) Shows epicardium (black) versus endocardium (red) differences in repolarisation duration. (b) Shows a comparable difference in APD between epicardium base (black) and apex (red).

1.2.4 Calcium and contraction

As the cardiac action potential propagates, it causes rapid depolarisation of the plasma membrane (sarcolemma) of individual cardiomyocytes, which is rapidly carried deep into the cell via transverse tubule (T-tubules) networks (See Figure 1.8). This causes calcium to diffuse into the cell, down its concentration gradient, predominantly through L-Type calcium channels (LTCC). This gradient is due to a high extracellular concentration of Ca^{2+} ions outside the cell (~2 mM) at rest (diastole), contrasted with 80-250 nM inside the cell cytoplasm. This calcium influx causes calcium-induced calcium release (CICR) via ryanodine receptors (RyRs) from the sarcoplasmic reticulum (SR), where calcium is stored at rest. This rapid calcium release transiently increases the intracellular calcium concentration 2 to 4-fold, to ~0.5-2 µM. Calcium ions bind to troponin-C, exposing the actin filaments to myosin. Contraction occurs, and the sarco/endoplasmic reticulum Ca^{2+}-ATPase (SERCA) pumps Ca^{2+} back into the sarcoplasmic reticulum (SR), lowering Ca^{2+} concentration in the cytoplasm, and terminating contraction. Membrane potential, intracellular calcium concentration and fractional shortening were measured from single cardiomyocytes in this work using fluorescent methods (see Figure 1.2).

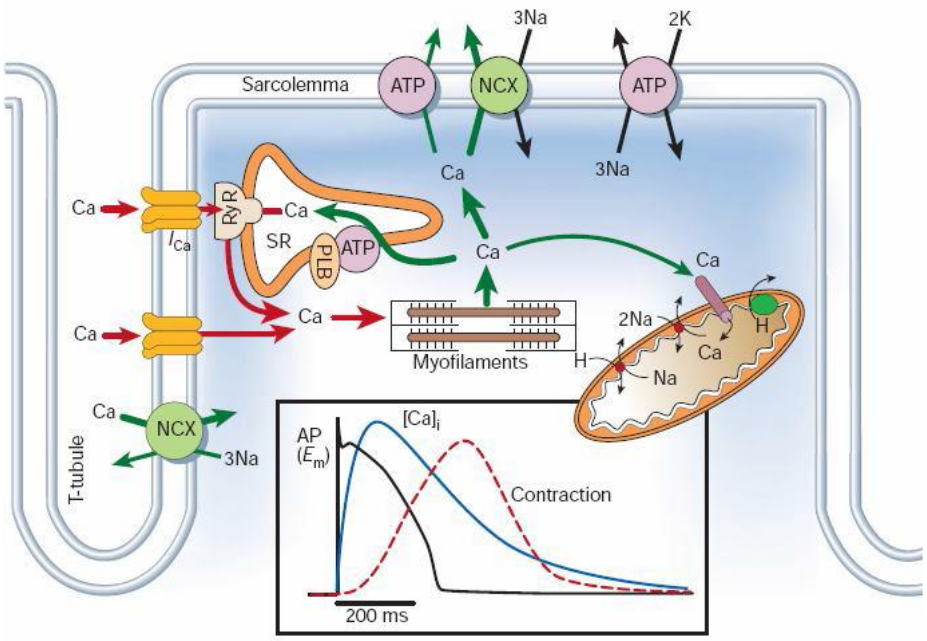

Figure 1.8 Schematic representation of Ca^{2+} entry and role in ventricular myocyte contraction. Inset diagram showing temporal relationship between excitation (action potential, black line), intracellular Ca^{2+} (calcium transient, blue line) and contraction (red dashed line). (ATP, ATPase; NCX, Na^+/Ca^{2+} exchanger; PLB, phospholamban; SR, sarcoplasmic reticulum; RyR, Ryanodine receptor). (Figure taken from Bers (2002) *Nature* 415, 198-205).

1.2.5 The force-frequency relationship

In the healthy myocardium, an increase in stimulation frequency is followed by a change in contractile force. This effect is often referred to as the staircase, Bowditch, or Treppe effect. This relationship is either positive of negative, depending on the species. Positive staircases are seen in human, rabbit and others (Gibbons and Fozzard, 1975; Wang *et al.*, 1988; Maier, Bers and Pieske, 2000), and negative in rat, mouse, most fish and other species (Orchard, 1985; Maier, Bers and Pieske, 2000; Shiels, Vornanen and Farrell, 2002).

An increase in stimulation frequency causes increases Ca^{2+} influx per unit time, due to higher frequency of APs, and subsequent L-type Ca^{2+} channel activation. This increases intracellular Ca^{2+} load, and in particular, SR Ca^{2+} content. The resulting increased Ca^{2+} transient amplitude in turn increases NCX-mediated Ca^{2+} efflux, such that the cell reaches a new steady state of Ca^{2+} flux balance, whereby NCX efflux increases to match L-type Ca^{2+} channel-mediated Ca^{2+} influx.

1.3 Cardiac arrhythmias

Arrhythmias can be defined as disruptions in the rate and/or order of activation and recovery of electrical activation in the heart (Tse, 2016). These occur on a range, from transient, benign events, to fatal conditions. Some arrhythmias can be as simple as bradycardia (i.e. slower than 60 beats.min^{-1}), common and mostly harmless in athletes, to tachycardia (i.e. faster than 100 beats.min^{-1}). The athlete heart can have an intrinsic rhythm as low as 30 bpm (Jensen-Urstad, Saltin and Jensen-Urstad, 1997), less than half the typical rate encountered in untrained individuals, in itself a prime example of the broad range of what can be considered "normal" electrophysiologically. More complex forms of arrhythmic events manifest themselves throughout the myocardium. Broadly speaking, the presence of an abnormal event in the electrophysiology of the heart is either the result of the *de novo* generation of an electrical wave which is not normally present, or the failure to terminate an event which does occur in normal physiology. Ectopic activity describes the former, and afterdepolarisations the latter. Ectopic focus can originate from inappropriate balance in sympathetic/parasympathetic drive, as well as ion channel expression changes in previously non-pacemaker tissue. Early afterdepolarisations (EADs), formerly defined as "oscillations at the plateau level of membrane potential or later during phase 3 of repolarisation" (Volders *et al.,* 2000), and generally occur as a result of L-type calcium channels reactivating at a membrane potential sufficient for re-activation of voltage-gated calcium channels, before the end of the AP (Maruyama *et al.*, 2011). They range from small positive deflections of the plateau phase, prolonging the APD, to full APs overlapping the one preceding them. Delayed afterdepolarisations (DADs) are part of phase 4 and may themselves cause ectopic beats. They are caused by an inward sodium/calcium exchanger (NCX) current induced by spontaneous SR Ca^{2+} release (see Figure 1.9). This is thought to be caused by excess intracellular calcium, which drives the NCX to pump in 3 sodium ions for 1 calcium ion out. This net positive charge builds up and depolarises the cell enough to cause an upstroke. Interestingly, DADs have been reported in the midmyocardium but not either in the epicardial or endocardial layers (Antzelevitch *et al.*, 1991).

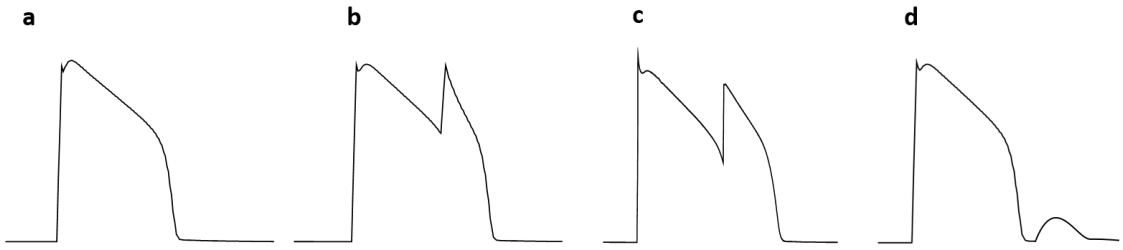

Figure 1.9. Examples of early-afterdepolarisation subtypes a. Diagrammatic representation of ventricular action potential. b. Phase 2 early-afterdepolarisation. c. Phase 3 early-afterdepolarisation. d. Delayed afterdepolarisation.

1.3.1 Long-QT syndrome

The electrocardiogram (ECG) trace reflects summation of action potential depolarisation and repolarisations of cardiomyocytes in the heart (Tse *et al.*, 2017), measured using 3-12 electrodes on the chest and limbs. The P-wave constitutes the depolarisation of the atria, followed by the QRS complex, which marks the depolarisation of the ventricles, followed by the T-wave, where the ventricles repolarise. Measurements made using these waves provides valuable information about the electrical state of the heart. The QT interval is a measure of the time between upstroke (Q-wave) and end of repolarisation (P-wave) (Jaiswal and Goldbarg, 2014). Because the repolarisation time is rate-dependent, QT will vary as a function of heart rate, and therefore requires correction before comparing absolute QT durations. A correction index for QT expressed as QTc is therefore calculated. Several methods exist to calculate QTc, most prominently by dividing QT by a factor related to the R-R interval (Bazett or Friedericia formulae). Generally, however, QT = QTc is assumed at heart rates of 60 beats/min as the aforementioned methods of calculating QTc tend to lose predictive power in strongly brady- and tachy-cardiac states (Jaiswal and Goldbarg, 2014). The necessity for standardisation of QT-interval durations becomes clear when defining upper limits for risk assessment. These limits are defined at 450 ms in males and 470 ms in females (Cubeddu, 2009), although the latest guidelines from the European Society of Cardiology suggest limits of 360 – 480 ms for both females and males (Priori et al. 2015). This gender discrepancy in the form of a reduced repolarisation reserve has been proposed to correlate with oestrogen, supported by higher rates of cardiac events in pre-pubertal boys and adult women (Drici and Clément, 2001).

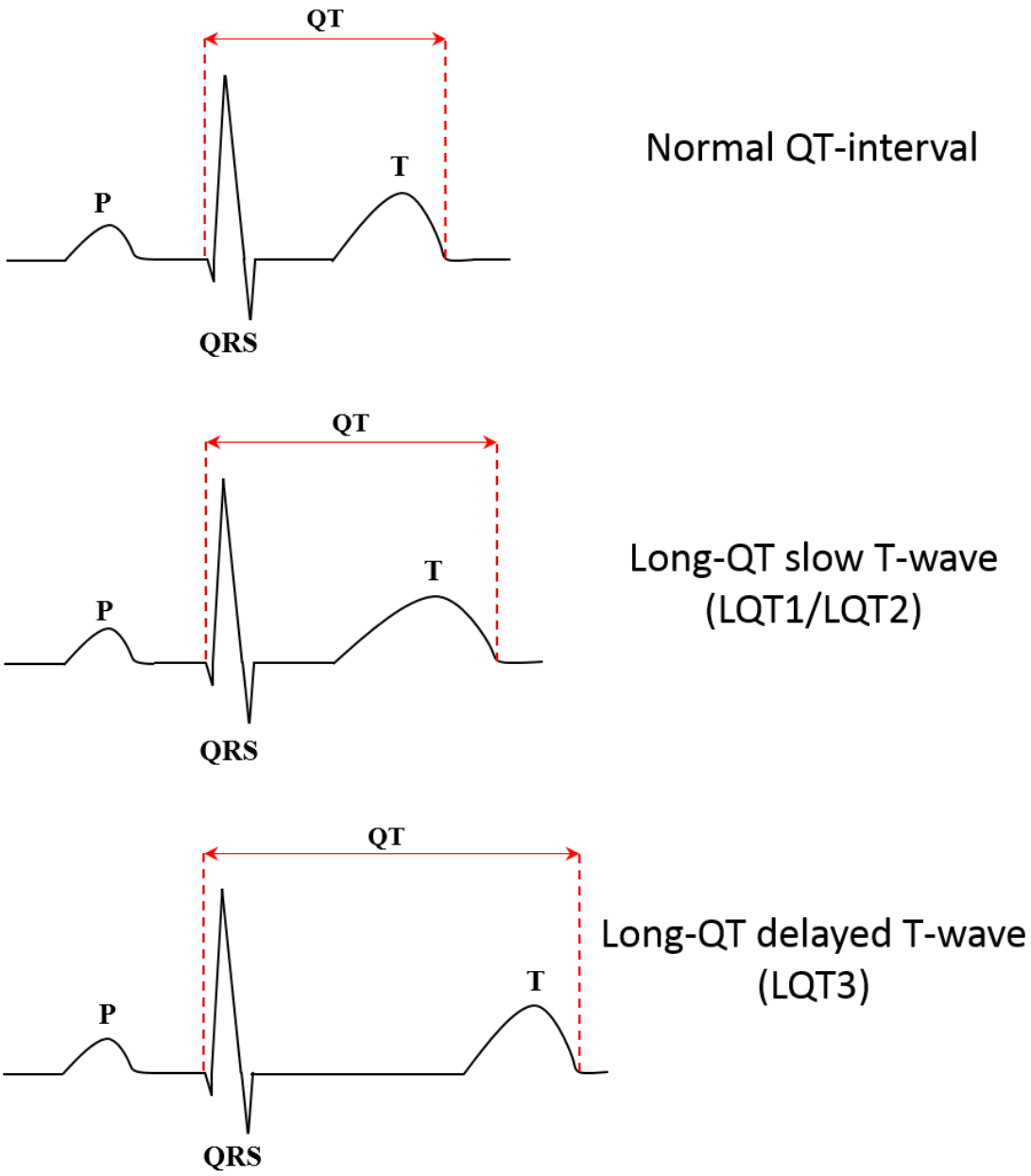

Figure 1.10 Diagrammatic examples of normal and abnormal long-QT ECG traces. LQT1 is represented by a slower and longer T-wave. LQT3 is caused by a delayed normal duration T-wave.

Congenital long-QT syndrome (cLQTS) is characterized by a prolongation of the QT interval in the ECG trace. It is a relatively rare disorder inherited at a rate of 1:5000 to 1:2000 of the general population, and can be caused by either a decrease in repolarising currents or an increase in depolarising currents (Tse *et al.*, 2017). While over a dozen subtypes have been identified, LQT1-3 make up 75% of cases observed (see Figure 1.10), respectively caused by mutations in KCNQ1, KCNH2 and SCN5A genes. LQT1 and LQT2 are both loss of function mutations affecting repolarising potassium currents (I_{Kr} and I_{Ks}, respectively),

while LQT3 causes a gain of function by increasing I_{Na} current function and thus promoting action potential duration (APD) prolongation.

The prolongation of APD, in these examples, is caused by three different mechanisms, which underlines the crucial notion of interplay and redundancy present in cardiac electrophysiology, where different initial states can result in undistinguishable AP morphologies. The simplified net result of these three mutations is a prolongation of the action potential, which decreases the repolarisation reserve (Roden, 2006), in turn increasing the risk of arrhythmia.

1.3.1.1 Acquired LQTS

While genetic mutations described previously are relatively uncommon, acquired LQTS is by far the more prominent form encountered in the clinic, manifesting itself as a result of a variety of factors, but predominantly drug administration (diLQTS)(Kannankeril and Roden, 2007). The female sex, hypokalaemia, atrioventricular block, and bradycardia are amongst the rest of the risk factors for acquired LQTS (Drici and Clément, 2001; Kallergis *et al.*, 2012). Work carried out in by Dessertene and colleagues (Motté et al, 1970) demonstrated symptom reversal was achievable through increased chronotropy and normalising of serum potassium. As described by Roden (2006), the key feature of the acquired form of ventricular arrhythmias resulting from QT prolongation is its unpredictability.

The establishment of drug-induced QT prolongation affirmed itself during the 1970s, as an increasing number of cases of torsade de pointes (TdP) were being reported, notably following quinidine administration, the only drug used for managing atrial fibrillation (AF) at the time (Schwartz et al., 2016; Selzer & Wray 1964; Friedberg 1966). Investigations of the effects of electrolyte imbalance (hypokalaemia) on the arrhythmogenic mechanisms of LQTS, using a hypokalaemia mouse model, found APD prolongation also increased EAD propensity and ensuing triggered activity (Killeen *et al.*, 2007). This occurs by increasing time spent at voltages within L-type Ca^{2+} channel activation ranges increasing $[Ca^{2+}]_i$. EADs can initiate arrhythmias, and can lead to the development of a specific polymorphic ventricular arrhythmia, torsade de pointes (see Figure 1.11). First described in 1966 by Dessertenne (Dessertenne, 1966), TdP is characterised as a “twisting of spikes” ECG trace, and has a high propensity to degenerate into ventricular fibrillation (VF), a major cause of sudden cardiac death.

Figure 1.11 Example trace of Torsades. ECG trace in a patient experiencing an episode of Torsade de Pointes. The distinct pattern of this form PVT is visibly twisting around the isoelectric line.

Although no mention of LQT was originally made by François Dessertenne and colleagues (Selzer and Wray, 1964) with regards to TdP, it is now known numerous compounds causing LQT also increase risk for TdP, as discussed later (Fenichel *et al.*, 2004).

1.4 Potassium channels in arrhythmia

The KCNH2 gene, known as the human Ether-a-go-go-Related gene (hERG), codes for the Kv11.1 protein making up the channel responsible for the rapidly activating delayed inward rectifier (IK_r) current. IK_r is a key player in the repolarisation phase of the action potential, and consequently mediates its duration. Pharmacological blockade of hERG leads to increased AP duration, and consequently increased QT-interval duration on the ECG trace. Many TdP-inducing drugs (Dofetilide, E4031) tend to block IK_r. Mechanisms underlying drug-induced TdP closely resemble the congenital form of long-QT (Schwartz, Woosley and Woosley, 2016). IK_r blockade prolongs the action potential plateau (phase 2) and mimics the genetic loss of function in LQT1/2 seen in congenital long QT syndrome.

Anti-arrhythmic drugs, perhaps ironically, make up the bulk of QT-prolonging compounds; they are however far from unique in this aspect, as several other drug types, including antibiotics (erythromycin), antipsychotics (Thioridazine) and anti-histamines also populate the ever-expanding list of LQT-inducing compound (Niemeijer et al., 2015; Yang et al., 2014; McComb et al., 1984; Kornick et al., 2003).

Much of the inhibitory compounds targeting hERG target its α-subunit. While hERG-blockade is a definite risk factor toward QT prolongation and TdP, not all drugs blocking it produce QT prolongation, nor does it always cause TdP. The basis for this apparent

discrepancy is unknown, and presents a substantial hurdle to drug development, causing withdrawal of clinically important drugs from the market (Day, McComb and Campbell, 1990; Monahan *et al.*, 1990; Schwartz, Woosley and Woosley, 2016).

With regards to the propensity to SCD following LQTS, several groups (Soyka, Wirtz and Spangenberg, 1990; Hohnloser, van de Loo and Baedeker, 1995; Torp-Pedersen *et al.*, 1999) found long-term exposure to QT-prolonging anti-arrhythmic drugs increased incidence of TdP by 1-3%. Amiodarone is an illustrative example of a drug which increases the QT-interval without increasing propensity of SCD, although there is still controversy regarding its benefit over placebo (Al-khatib et al. 2017; Bardy et al. 2005) This highlights the fact that the link between the two may not be a straightforward causal relationship.

The mechanism behind this apparent inconsistency in drug effects, including compounds causing LQT but not TdP, or TdP without LQT may stem from additional interactions, perhaps acting on several ion channels and proteins together, thus amplifying or cancelling out effects depending on local expression levels of involved proteins.

1.4.1 Torsade de Pointes (TdP)

Torsade de Pointes was first described by Dessertenne in 1966 as a twisting of the QRS complex around the isoelectric line. It is now classified as a form of polymorphic ventricular tachycardia. Although it can terminate spontaneously, it does not necessarily do so predictably, as the initiating electrical event can be identical to the terminating one (Kriklerl *et al.*, 1976). It can recur, and potentially degenerate into ventricular fibrillation.

The mechanisms underlying the pathophysiology of TdP are still unexplained. Despite being extensively studied, and known to severely undermine drug development, TdP prediction and prevention is still a major problem today. Its incidence in patient populations is also difficult to measure, because it requires an ECG to be taken during such an episode, which is often transient, and is known to spontaneously terminate. Furthermore, it is estimated that roughly 1 in 20 cases of TdP could currently be misinterpreted and reported as VT, VF or unexplained death, as the patient may die prior to an ECG being taken (Molokhia *et al.*, 2008).

1.5 Pharmacological screening for pro-arrhythmic potential

The importance of successfully identifying new drugs likely to cause long-QT, and, potentially, increase risk of TdP cannot be understated. Regulatory agencies such as the Food and Drug administration (FDA) and European Medicines Agency (EMA) now routinely require screening of new compounds for potentially dangerous LQT-induced effects (Shah, 2005). Anti-arrhythmic drugs are traditionally divided into four main classes, specific to their main target channel subtype. Na^+ channel blockers are classified as type I, with Ia being less specific, and additionally prolonging APD through IKr block. Ib are more specific to the Na^+ channel, and benefit from fast association and dissociation kinetics, shortening the AP but prolonging the post repolarisation refractory period (PRRP). Class Ic block Na^+ channels with slower kinetics, mimicking functional loss of peak Na^+ (Meregalli *et al.*, 2006), and do not affect APD. Class II are β-blockers, decreasing cardiac sympathetic input via β1-adrenergic receptors. Class III antiarrhythmics inhibit K^+ channels (primarily IKr), causing APD prolongation and a reduction in the effective repolarisation period (ERP). Class IV compounds act on L-type Ca^{2+} channels, and are sometimes used for the treatment of AF. L-type blockers such as nifedipine cause APD shortening and decreased inotropic effects by lowering $[Ca^{2+}]_i$ (Grunnet, 2010).

A drug is considered QT-prolongating when either a QT interval of 500 ms or above is reached, or if it causes an increase of 60-70 ms from baseline, the latter accounting for naturally short-QT individuals.

A common feature shared by TdP-inducing drugs is hERG channel blockade. Curiously, hERG blockade and QT-prolongation alone are not good predictors of TdP incidence. It is posited that the disparity in compound metabolisation in the body could explain, in part, why certain drugs perform unpredictably *in vivo* (Niemeijer *et al.*, 2015). It is likely that compounds with a low potency for hERG blockade may not reach high enough plasma levels for comparable degrees of hERG blockade *in vitro* or *in silico*, such as terfenadine or astemizole (Schwartz, 2016). In contrast, certain concomitant conditions like impaired metabolism may exacerbate TdP with ordinarily safe compounds. To underline this, patients with a long history of treatment with a particular hERG blocker only developed TdP following a change in their medical condition, like reduced renal excretion (Anderson and Prystowsky, 1999; Reiffel and Appel, 2001). Patient-specific risk assessment must therefore be carried out on a case-by-case basis, and be an integral part of the treatment process.

1.6 Methods of study for electrophysiology

Difficulties in screening and preventing TdP, as well as other lethal arrhythmias, drive the search for understanding the mechanisms underlying tissue electrophysiology. Studying whole heart electrophysiology requires a systems-level approach: from a single ion pump/channel to the whole cell, from a cardiac region to the whole ventricle, and how this coordinated electrical stimulation and calcium release triggers contractile proteins and finally generates blood flow through the heart chambers, to the body. Studying each aspect in isolation has proved problematic, as computer models often fail to accurately replicate what is observed *in vivo*. Such models routinely make assumptions of tissue homogeneity, either constrained by a ceiling in computational power, or simply because experimental data (i.e. cellular variation) is missing (Ponnaluri *et al.*, 2016). Various methods used to study cardiac electrophysiology are discussed below, outlining advantages and limitations or current techniques, incorporating the work carried out in this thesis and its relevance the field.

1.6.1 Action potential mathematical modelling

In 1952, Hodgkin and Huxley studied electrical current flow through the membrane of the giant squid axon. Its unusually large diameter (typically 0.5 mm) constituted a convenient medium for electrophysiological study. Using a capillary threaded into the axon with an additional wire, they performed voltage clamp experiments, which led to the formulation of the now famous Hodgkin-Huxley model (Hodgkin and Huxley, 1952). Composed of just three currents (K^+, Na^+, leak (other ions)), it allowed them to predict the shape of action potentials with striking accuracy. This work pioneered the field of electrophysiology and earned both the Nobel Prize in Physiology and Medicine in 1963. Based on this seminal model, many mathematical models have been developed to describe action potentials in cardiac cells, tissues and species. These models are comprised of a set of nonlinear differential equations for voltage and a set of gating variables and ionic concentrations. The list of available models is steadily growing, each building on previous iterations of itself or using other models to improve predictive power and fidelity to experimental data (Shannon *et al.*, 2004; Mahajan *et al.*, 2008; Grandi, Pasqualini and Bers, 2010; O'Hara *et al.*, 2011; Gong and Sobie, 2018).

1.6.2 Patch clamp

Patch-clamping excitable cells or tissue using a glass micropipette is considered the gold standard measurement of cellular electrophysiology. Another joint Nobel Prize in Physiology or Medicine was awarded to Erwin Neher and Bert Sakmann in 1991 for developing this technique (Neher & Sakmann, 1976) . Patch clamp allows the direct recording of the electrical potential inside the cell, by applying gentle suction via a mouthpiece connected to a blunt glass micropipette. Several variations of the technique have been developed to record on-cell, whole cell, as well as inside-out and outside-out transmembrane membrane potential (Richardson and Xiao, 2010). Patch clamp allows for the study of individual cell action potentials in response to stimuli (e.g. drugs) through sequential changes in bath solutions; however, it is terminal, and the cell cannot survive the measurement, narrowing protocol complexity and limiting throughput.

Three main aspects render this technique particularly difficult. Firstly, experimental experience is indispensable to success. While the precision of the equipment used does play a part, careful application of pressure to the cell, and the precise amount of suction is challenging. Successfully forming a tight seal (giga-ohm seal) with the cell membrane is a challenging task (Scanziani and Häusser, 2009). Maintaining a seal with the membrane also presents a challenge. Unwanted vibration and movement of the glass micropipette can cause leakage between glass and membrane, or tear into the cell entirely, which allows calcium to flow inwards and hypercontracts the cell. The electrical resistance of the micropipette, a critical aspect for successfully achieving a seal with the cell membrane, is a function of its manufacture. The protocols used to achieve the desired micropipette properties (e.g. tip diameter and sharpness) rely on heating and pulling a thin glass tube with both accuracy and consistency. Glass micropipette resistance can notably be influenced by the material properties of the glass, ambient temperature and humidity. Finally, the quality and fragility of the cell membranes on the day of cellular isolation can negatively impact the quality of the seal, and consequently further reduce throughput. The combination of the above factors has contributed to patch clamping being regarded as much of an art as a science, given its capricious nature.

1.6.3 Optical methods

While patch clamping cells yields excellent quantitative measurements of electrical potential across the cell membrane at a high temporal resolution (up to 50kHz), it is a difficult

technique to implement, even with experience and skill. Seasoned electrophysiologists will successfully patch no more than 10 cells per individual heart. This poses a problem, as it further reduces the experimental yield, already jeopardized by variations in cell viability due to enzymatic digestion. The use of less invasive techniques, like fluorescent dyes, to measure intracellular processes has capitalised on this. These cellular dyes are designed to change their fluorescent properties following specific processes (i.e. changes in membrane voltage (V_m) and $[Ca^{2+}]_i$). They currently provide excellent spatial and temporal resolution from the whole heart (i.e. epicardial surface) to individual cells (neurons, cardiomyocytes) to organelles (e.g. SR-specific).

Voltage-dyes can be broadly separated into two main categories, fast- and slow-response. While slow-response dyes, based on voltage-dependent accumulation can benefit from large relative increases in brightness to changes in membrane potential (up to 80%ΔF/F per 100 mV), (González and Tsien, 1997), the drawback is their slow response time, due to their reliance on the redistribution of the dye within the lipid membranes, much slower than certain cellular events such as fast Na^+ entry into cells (Miller, 2016).

Commonly used probes sensitive to fast voltage changes include the ANEP dyes developed by the Loew group (Fluhler, Burnham and Loew, 1985), such as di-4-ANEPPS and di-8-ANEPPS (Matiukas *et al.*, 2006). Dyes with high fluorescent response per mV coupled with fast response entail certain caveats. Cytotoxic effects, from either the molecule itself, or ROS generation following exposure to light are a common limitation to their use (Schaffer et al., 1994; Herron et al. 2012). Through ongoing innovation, fluorescent dyes have improved over the past decade. The search for fast and bright voltage-sensitive dyes led to the recent development of VoltageFluor dyes (Miller *et al.*, 2012). Their basic mechanism uses photoinduced electron transfer (PeT) (Li 2007) as a direct competitor with fluorescence emitted by the molecule. The interaction between an electron donor and acceptor linked by a molecular wire is highly localised (in the order of nanometres). Consequently, the change in observed fluorescence following changes in V_m is extremely fast, and lends itself to resolving fast physiological events such as action potential upstroke, occurring in the millisecond range.

The proprietary voltage sensitive dye FluoVolt (Thermo Fisher Scientific) was primarily investigated and used in this thesis. Minimising cell toxicity, while achieving a high signal-to-noise ratio was one of the primary aims to optimise fluorescent measurements recorded for this work.

Calcium-sensitive molecular probes such as Fura-4F and Fluo-4 have been used for several decades (Bootman et al., 2013). Much like other fluorescent molecules inserted in membranes (Indo- and Fluo- dyes), they alter their fluorescent properties in response to changes in cytosolic changes in $[_{i}Ca^{2+}]$.

Using combinations of dyes in the same sample presents its own challenges. As the excitation and emission spectra of cellular dyes shift transiently with $[Ca^{2+}]_i$ and/or V_m changes inside the cell, creating crosstalk (mutual distortion) between wavelength channels, separating each fluorescent signal from each other becomes critical. This is achieved through the selection of dye with non- or minimally overlapping spectra combined with optical filters allowing separation of signals, or through spectral deconvolution, a form of post-processing to retrieve individual signals from a compound light emission. While there are pros and cons associated with either method, combining fluorescent dyes is rarely ideal. Near-infrared (>700 nm) dyes have been developed to avoid interference with endogenous chromophores, and for deep tissue imaging, by shifting their spectra towards longer (red to infrared) wavelengths (Matiukas et al. 2006; Salama et al. 2005). Expanding the range of wavelengths used also addresses the issues arising with spectral overlap, by allowing more than one fluorophore to be used simultaneously in the same sample with minimal interference (Herron, Lee and Jalife, 2012).

1.6.4 *In silico* methods

Understanding arrhythmia demands a stratified approach to the respective functions, and interactions of cardiac tissue, cells, and proteins. Mathematical models have been extensively used toward the better understanding of electrophysiology, both in health and disease. Comprising a set of differential equations that describe the respective "states", (probability of being open or closed) of known channels, currents and variables such as intracellular ionic concentrations, recent models aim to describe the cell behaviour and to simulate health and disease through iterative calibrations with new experimentally acquired datasets.

While proving useful in specific cases, these models are intrinsically limited by the data on which they are based. This essentially confines the span of possible predictions made by a hypothetical model to a subset of the total physiological range. Data collection tends to summarise findings as the average cellular behaviour observed experimentally, which greatly limits, and arguably incapacitates models with regards to predictions of population

variation. This could explain the limitations currently encountered in drug development. The mechanisms responsible for disparate drug effects from within subject populations are still elusive, forcing groups to investigate entire populations of models in order to build a more comprehensive picture of population response to stimuli (Britton et al., 2013).

Mathematical models typically output a predicted value for a given set of input variables. If population variation becomes a factor of interest, the output must also be represented as a "spread" of output values in the predicted output space (Kannankeril et al., 2010). These notions led a number of groups to pioneer the investigation of population variation within individual hearts (Sobie, 2009; Britton *et al.*, 2013; Muszkiewicz *et al.*, 2016).

Experimentally determining the discrete effect of each variable change is made challenging when several changes are taking place concurrently, and challenged further when they influence one another dynamically. The relative weighting certain parameters (i.e. I_{Na}, I_{Kr}, $I_{Ca\text{-}L}$) carry in each respective model can vary significantly, and potentially skew the predictions made depending on the model used (Sarkar, Christini and Sobie, 2012). A straightforward approach to testing this is to vary each input parameter one at a time, and record how the output (e.g. repolarisation) is affected by each. This essentially yields a measure of parameter sensitivity. Sensitivity analysis of specific parameters was used by Romero et al. on a human ventricular cell model, by varying one parameter at a time by ±15% and ±30% from baseline, to investigate its involvement on arrhythmic risk (Romero *et al.*, 2009). Providing a robust measure of APD variation in controls experimentally will increase the relevance of parameter expression ranges expressed in electrophysiological models.

Going one step further, models assessing model-model variation provide insight into the respective strengths and weaknesses of each. The implicit goal of cellular models is first to replicate experimental findings and then to predict subsequent findings. As prediction variation in any single model can be high, it could be minimised by assessing populations of predictions from separate models. As the number of developed models grows each year, the need for standardisation emerges, and several groups are attempting to address this problem (Terkildsen *et al.*, 2008; Cooper *et al.*, 2011).

It is clear there exist limitations to both modelling and experimental investigation of cardiac arrhythmia. A combined approach to minimize weaknesses inherent to each could therefore

improve the prospects of the field by creating better, more versatile models capable of making testable predictions using medium/high-throughput experimental methods.

1.7 Aims

The primary aim of this thesis was to develop a medium/high-throughput method to study electrophysiological variation and E-C coupling in cell populations of the rabbit left ventricle.

Using this technique, the secondary aims were to carry out regional comparisons of cellular electrophysiology between healthy and MI hearts, and quantify cellular and animal variation. Lastly, assessment of ion channel blockade on cellular sub-regions of the heart using same-heart cell populations.

1.7.1 Specific aims

1. Develop and refine a medium/high-throughput methodology to study electrophysiology and E-C coupling of isolated cell populations in the rabbit left ventricle. (Chapter 3)

2. Rigorously quantify physiological heterogeneity across populations of ventricular myocytes. (Chapter 4 and 5)

3. Measure and quantify heterogeneity in response to IKr and L-type Ca^{2+} channel blockade in populations from sub-regions of the rabbit left ventricle. (Chapter 6)

4. Infer from data how ion transport mechanisms vary and co-vary across populations. (General discussion)

Chapter 2: General Methods

2.1 Animals

Animals used in this work were male New Zealand White rabbits (2.5-3.5kg) sourced from Envigo (Huntingdon, UK). Following a seven day quarantine/acclimatisation period, animals used at the University of Glasgow were killed in accordance with the Home Office Guidelines of the Animals (Scientific Procedures) Act 1986.

2.2 Coronary artery ligation procedure

The coronary artery ligation technique was performed as previously described (Pye and Cobbe, 1996; Ng *et al.,* 1998; McIntosh, Cobbe and Smith, 2000) The operative procedures and echocardiographic assessment of the animals was performed by senior technician Michael Dunne at the University of Glasgow. Rabbits (12 weeks old) were pre-medicated with 0.4 mL/kg intramuscular Hypnorm (0.315 mg/mL fenatyl citrate: 10 mg/mL fluanisone; Janssen Pharmaceutica, Beerse, Belgium) and given antibiotic prophylaxis with 100 mg intramuscular Ampifen (Mycofarm UK Ltd, Cambridge, UK). The marginal ear vein was cannulated, and anaesthesia induced using 0.25-0.5 mg/kg midazolam (Hypnovel; Roche, Basel, Switzerland). The animal was intubated, and anaesthesia was maintained with 1% halothane in a 1:1 ratio of oxygen to nitrous oxide, delivered by Harvard small animal ventilator. (Harvard Apparatus Ltd., Edenbridge, Kent, UK). Access to the heart was obtained by a left thoracotomy through the fourth intercostal space. The marginal branch of the left anterior descending (LAD) artery, supplying the left-ventricular wall, was identified and ligated mid-way between the atrioventricular groove and apex. This produces a homogeneous infarcted area comprising 40-50% of the left ventricle. A dose of 10mg/kg quinidine (Sigma-Aldrich Company Ltd., Poole, Dorset, UK) was administered prophylactically as an antiarrhythmic agent, but in approximately 30% of cases ventricular fibrillation occurred, requiring a 5-10J epicardial direct current shock to restore normal sinus rhythm. After ensuring the animal was stable, the thorax was closed, and animals were administered 20 mL intravenous saline to replace operative losses. Analgesia was administered (0.04% intramuscular buprenorphine hydrochloride; Reckit Benckiser Pharmaceuticals Inc, Richmond VA, USA) immediately following the operation and the next morning. During recovery the animals were monitored for signs of distress. Sham-procedure animals underwent identical surgical procedures, with the exception of the coronary tie.

2.3 Physiological extracellular solutions

2.4 Extracellular bath solution

All work performed on isolated cardiomyocytes used Krebs solution as an incubating bath solution for experimentation. All chemicals were obtained from Sigma-Aldrich (Saint Louis; MO, USA) unless otherwise stated.

2.4.1 Isolation medium

130 mM NaCl, 4.5 mM KCl, 3.5 mM $MgCl_2 6H_2O$,0.4 mM NaH_2PO_4,5 mM HEPES, 10 mM glucose. Solution pH was adjusted to 7.25 at 37˚C using 1 M KOH.

2.4.2 Krebs solution

120 mM NaCl, 20 mM HEPES, 5.4 mM KCl, 0.52 mM NaH_2PO_4, 3.5 mM $MgCl_2 6H_2O$, 20mM taurine, 10 mM creatine and 11.1.mM glucose hexahydrate. Solution pH was adjusted to 7.4 at 37˚C using 1 M NaOH.

2.4.3 Kraft-Bruhe (KB) solution

70 mM KOH, 40 mM KCl, 50 mM L-glutamic acid, 20 mM taurine, 20 mM KH_2PO_4, 3 mM $MgCl_2 6H_2O$, 10 mM glucose, 10 mM HEPES, 0.5 mM EGTA, pH 7.4 at 37˚C using 1 M KOH.

2.4.4 Enzyme

Collagenase enzyme (powder; Worthington Biochemical Corporation) was added to KB solution (217 IU/mL) and re-circulated through the perfusion system for ~5 minutes until the heart tissue began to moderately swell and lighten in colour.

2.4.5 Langendorff and cardiomyocyte isolation

All animal handling and procedures including surgical interventions and Langendorff procedures (see Figure 2.1) were carried out by laboratory technicians Aileen Rankine and Michael Dunne. Male New Zealand White rabbits (2.5-3kg) were euthanised with an intravenous (IV) injection of 0.5mL/kg Euthatal (200 mg/mL, Sodium pentobarbitone, Rhone Merieux Inc, Athens, GA, USA) mixed with 500IU of heparin (CP Pharmaceutical

Ltd, Wrexham, UK) via the left marginal ear vein. Once absence of pain reflexes was confirmed, hearts were quickly excised with ~0.5cm of the ascending aorta, and placed in ice-cold KB solution to inhibit muscle contraction. Prior to starting perfusion, the system was primed with KB solution to avoid air bubbles entering the system and potentially compromising heart muscle perfusion. Excess tissue was trimmed away and the heart was connected to a Langendorff system, and retrogradely perfused with calcium-free oxygenated KB (37°C) using a peristaltic pump at a constant flow rate of 20ml/min for 5 minutes (Skrzypiec-Spring *et al.*, 2007; Bell, Mocanu and Yellon, 2011). The heart was then perfused with enzyme solution, which was collected and re-circulated. After 3 min, 100 mmol/L $CaCl_2$ solution was added to achieve a final calcium concentration of 0.05 mmol/L. Digestion was continued for 5-6 minutes, until the heart began to soften to the touch and lighten in colour. The heart was perfused with KB solution containing a 10g/L bovine serum albumin (BSA) containing 0.075 mmol/L calcium. In infarcted hearts, the apex and a 3-5 mm rim around the infarct zone were removed. This step removed a large portion of the scar tissue, and has also been shown to remove peri-infarct border zone myocytes (Burton, McPhaden and Cobbe, 2000). The equivalent apical region was removed in Sham animals. Perfusion was stopped and the heart was dissected. The ventricles were cut into ~1 mm^2 segments in BSA solution. Using fine forceps and scissors, both epicardial (epi) and endocardial (endo) regions were isolated by cutting sections ~1 mm deep into either side of the LV, excluding the mid-myocardial region. Basal and apical regions were obtained from top and bottom of the LV, with a separation of 1 cm along the longitudinal axis of the heart (see Figure 1.5). Tissue pieces were placed in a 15 mL culture flask and placed on a shaker for 20 min. Cells were gently triturated with a Pasteur pipette to further dissociate myocytes, and the supernatant was filtered through polyamide mesh (250 μm pore size) prior to resuspension in KB solution.

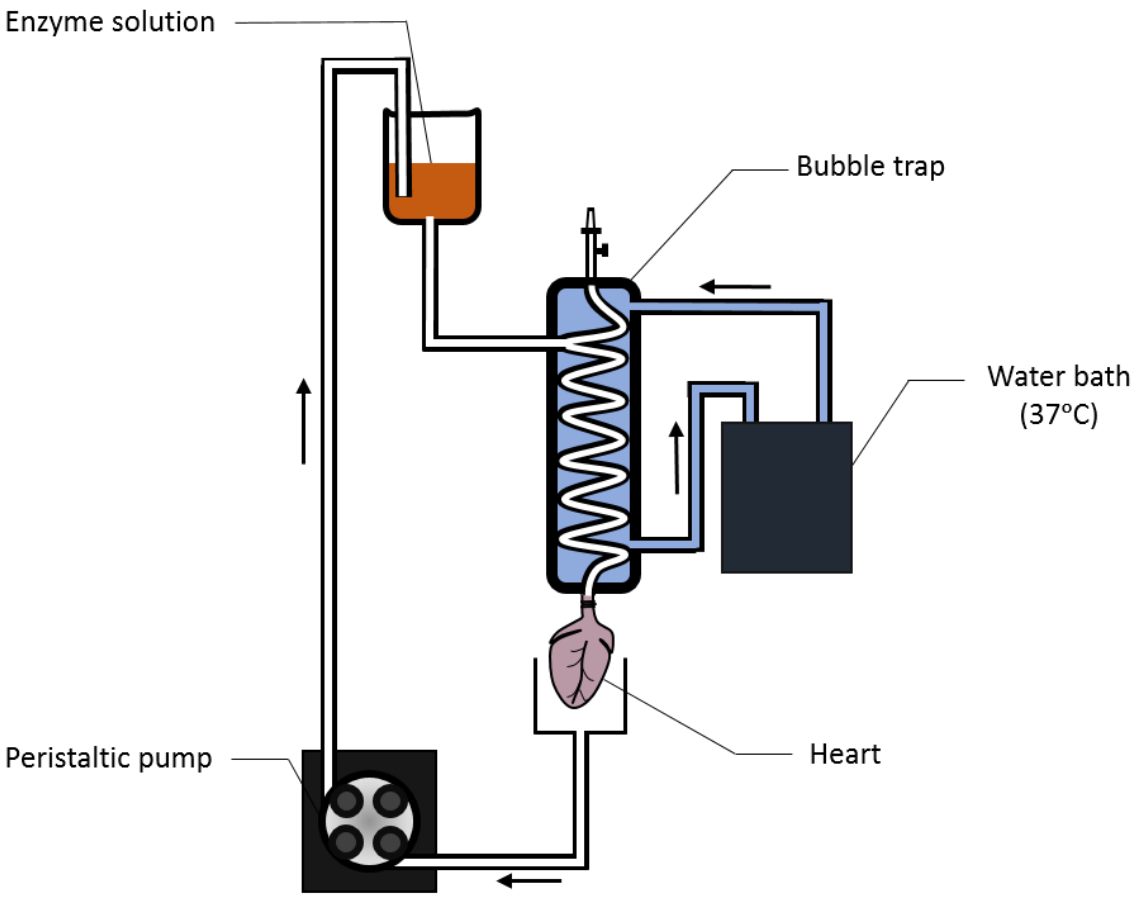

Figure 2.1 Diagram of Langendorff setup for cell isolation. Simplified diagram of Langendorff setup using peristaltic pump and water bath system for retro-perfusion of coronary arteries with enzyme solution at 37°C.

2.4.6 Cell preparation for experimentation

Cells underwent serial incubations in Krebs solution baths containing increasing concentrations of Ca^{2+} (using 1 molar $CaCl_2$). Cells were left to settle with gravity for 10min in 15mL Falcon tubes containing Krebs and increasing calcium concentrations: 100 µM, 300 µM, 1 mM, and 1.8 mM $CaCl_2$, respectively. Experiments were only performed on cells with clear striation and showing no signs of abnormal electrical behaviour, such as EADs, alternans, or irregular beats.

2.5 Optical apparatus setup

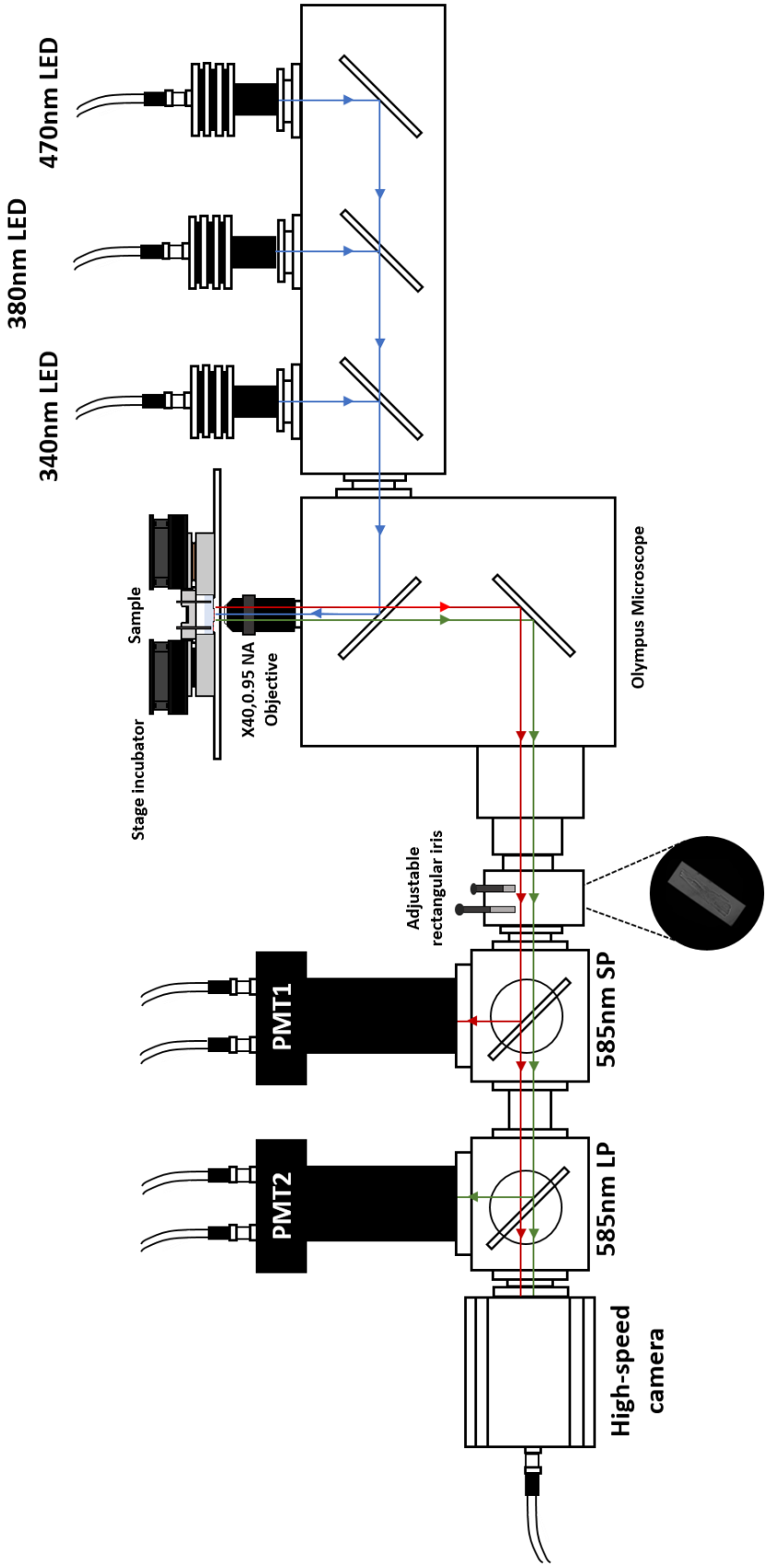

Figure 2.2 Optical apparatus diagram. Simplified diagram of optical system used for fluorescence measurement of action potentials and calcium transients in isolated cardiomyocytes (CM).

Light from excitation LEDs (340nm, 380nm, or 470nm) excites the sample in the custom stage incubator (see Chapter 3). Emitted fluorescence is reflected from the sample onto a 45° 585nm short-pass and a long-pass dichroic mirror to photomultiplier tubes. The light signal intensity, amplified via photo-multiplier tube, is converted to a voltage signal (Cairn Research Ltd). The output is then passed through an analog-to-digital converter (National Instruments UK), and displayed on the monitor using the CellOPTIQ program designed by Dr Francis Burton.

2.5.1 CellOPTIQ

The software used to control hardware, as well as perform trace analysis used in these fluorescence experiments was designed and written by Dr Francis Burton. The CellOPTIQ® platform was used throughout this work to collect fluorescent measurements from isolated cardiomyocytes loaded with fluorescent dyes.

CellOPTIQ controlled the XY position of the bath system using a motorised stage, allowing cell locations to be saved for repeated measurements (e.g. before and after drug incubation). It also provided flexible control of the excitation LED protocol used for cellular dye excitation (see Chapter 3). Finally, CellOPTIQ was used to analyse fluorescent traces acquired for each cell, by averaging action potential and calcium transient trains. Descriptive values of action potentials and calcium transients were generated and exported to a summary table for statistical analyses.

2.6 Fluorescence spectroscopy

Optical dyes which display transient changes in fluorescence intensity at a fixed wavelength in response to changes in substrate availability (e.g. V_m, $[Ca^{2+}]$) are referred to as single wavelength. In contrast, ratiometric indicators change the shape of their excitation or emission spectra in response to changes in calcium concentration. Expressed as a ratio, their relative fluorescence measured at two different wavelengths provides a robust measure of substrate change without being negatively impacted by disparate dye loading, uneven illumination or movement (Wokosin, Loughrey and Smith, 2004).

2.6.1 Voltage-sensitive dyes

The dyes used in this study were selected based on their excitation emission spectra. The apparatus used has previously been optimised for di-4-ANEPPS, excited at 470 nm (see

Figure 2.3). Di-4-ANEPPS has been widely used to monitor changes in membrane potential (Morad and Salama, 1979). While it was reported to yield ~7-10% ΔF/F per 100mV, di-4-ANEPPS is rapidly internalized into cells, limiting its uses to short experiments (Herron, Lee and Jalife, 2012). The recording of membrane potential in adult cardiomyocytes in this work was achieved using established voltage-sensitive fluorescent dyes di-4-ANEPPS, and the more recently developed FluoVolt.

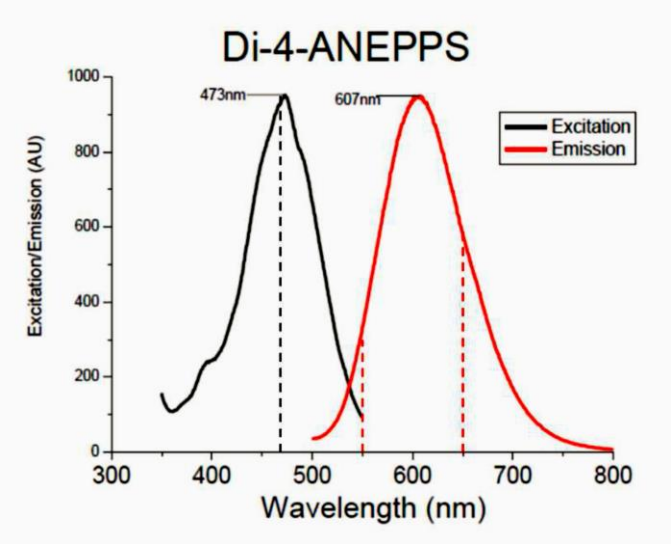

Figure 2.3 Di-4-ANEPPS spectra. Excitation(black) /Emission (red) spectrum of di-4-ANEPPS.

As voltage potential increases inside the cell from a resting potential (e.g. from -85 mV to -40 mV), di-4-ANEPPS emission peak shifts left toward shorter wavelengths. Measuring emitted light at two wavelength bands (dashed red lines at 550nm and 650nm, respectively.) consequently allows a quantitative measure of the membrane potential by calculating the fluorescence ratio of these emission bands.

2.6.2 FluoVolt excitation/emission spectra

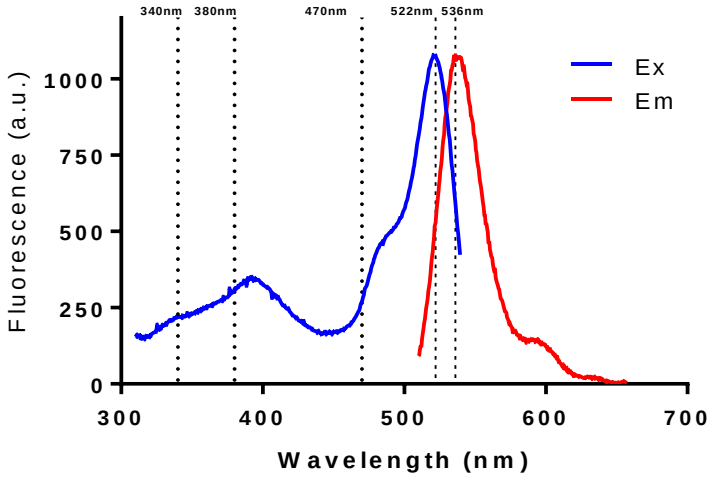

Figure 2.4 FluoVolt Spectra. Excitation-emission spectra of FluoVolt®. Excitation peak is at 522nm, with peak emission at 536nm. Also displayed for reference are the excitation wavelengths used for both voltage (470nm) and calcium (340nm/380nm) in this thesis.

The excitation-emission spectrum of the FluoVolt molecule has not been made publicly available. Using a spectrophotometer (LS 50b, Perkin-Elmer), the FluoVolt excitation and emission spectra were determined (see Figure 2.4). Transparent cuvettes (1.5 mL) were filled with FluoVolt-loaded cell suspension in Krebs solution. Background fluorescence was assessed using a dye-free cell suspension. Using a 15 nm slit width, combined with a 150 $nm.min^{-1}$ scan speed produced the most detailed spectra, free of signal saturation. All spectra shown in this work were background-subtracted, eliminating the contribution from cell membrane autofluorescence. The same excitation wavelength (470nm) as that used to excite di-4-ANEPPS was used with FluoVolt, as the resultant emission signal brightness was satisfactory, and consequently did not require modifications to be made to the experimental apparatus.

While information about the FluoVolt molecule is still proprietary, Woodford et al. (2015) describe voltage-sensitive molecules (VoltageFluor dyes) with strikingly similar Ex/Em peaks to what we found for FluoVolt. One molecule, VF2.1.Cl (see Figure 2.5), is the best fit with reported peaks at 522nm/536nm, and a reported $\Delta F/F$ of 27% per 100mV.

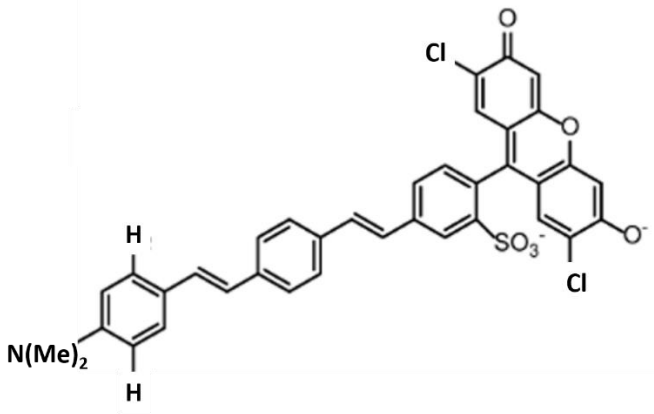

Figure 2.5 VF2.1.Cl molecule. Proposed FluoVolt molecular structure from literature (Woodford et al. 2015).

2.6.3 Intracellular calcium ion indicators

Calcium ion (Ca^{2+}) indicators are molecules based on the structure of a Ca^{2+} chelator (BAPTA) and allow the measurement of calcium transients via a change in the intensity or wavelength of the emitted light (Grynkiewicz, Poenie and Tsien, 1985).

The following work used Fura-4F, in its acetoxymethyl (AM) ester form (Life technologies, Thermo Fisher Scientific; Waltham, MA USA). The AM modification allows Fura-4F to permeate cellular membranes. The lipophilic groups tail is cleaved by non-specific esterases intracellularly, leaving a charged form of the dye which exits the cell at a slower rate than the non-AM form (Grynkiewicz, Poenie and Tsien, 1985). Fura-4F alters its excitation spectrum when bound to calcium (see Figure 2.6). The bound form has an excitation peak at 380 nm, contrasting 340 nm for the unbound form. Fura-4F(AM) was consequently excited at these two different wavelengths in rapid succession (340 nm and 380 nm, respectively) using LEDs. The emission fluorescence was recorded at a single wavelength band (>585 nm) and expressed as a ratio of the two resulting signals. Following precise calibration of dye fluorescence relative to local presence of Ca^{2+} in solution (see Chapter 3), accurate Ca^{2+} measurements could be made in live single cells at a temporal resolution of 2 ms (500Hz sampling rate).

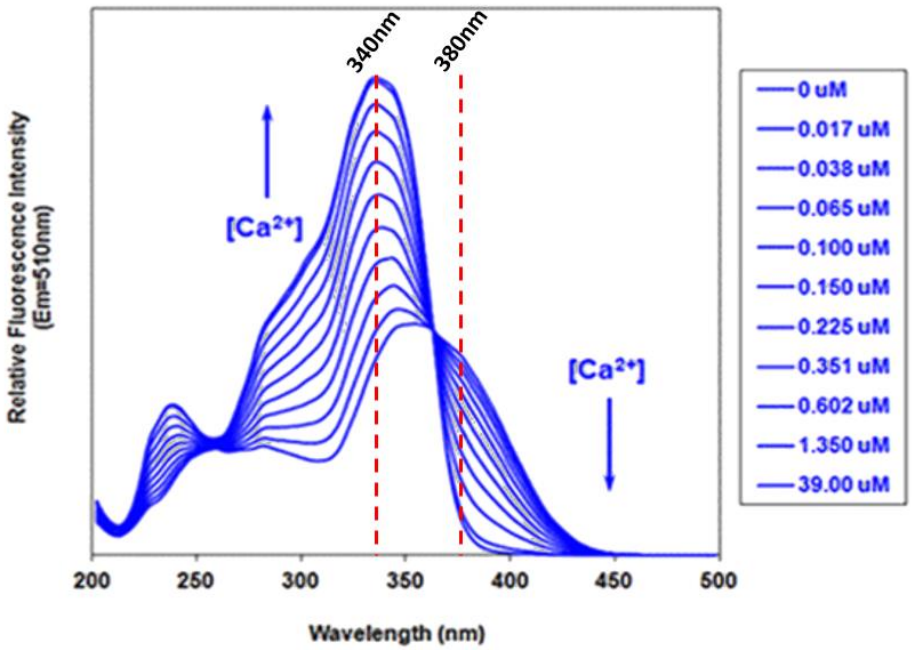

Figure 2.6 Excitation spectrum of Fura-2 overlaid at 10 incremental concentrations of Ca^{2+} (0-39 µM). It is identical to Fura-4F and consequently excitation wavelengths used in these experiments are outlined at 340 nm and 380 nm (dotted lines). The isosbestic point (360 nm) denotes where emission intensity at 510nm is not a function of [Ca^{2+}], and remains constant at any concentration. Figure taken from (Bioquest, 2018).

2.6.4 Dye loading protocols for isolated CMs

2.6.4.1 Di-4-ANEPPS loading procedure

Cells were incubated for 1 min in 6 µM di-4-ANEPPS, then gently centrifuged to form a loose pellet and resuspended in 1.8mM Ca^{2+} Krebs solution. 1mL cell suspension was added to 1 mL of clear Krebs to a 35mm, glass-bottomed dish (MatTek, 35 mm, 14 mm microwell).

2.6.4.2 FluoVolt cell-loading procedure

The FluoVolt (Thermo Fisher) molecule size and molar mass is not currently available in literature due to commercial restrictions. Concentrations used are expressed as µl of FluoVolt dye per mL of Krebs solution. Manufacturer recommendation is 1:1000 (1 $\mu l.mL^{-1}$) for 25 min at room temperature (RT). As described later, initial experiments used manufacturer-recommended protocols, however these were altered following optimisation. Optimised protocols used 1 µl in 6 mL Krebs, resuspending cells halfway through the 25min incubation period. After settling down, the supernatant was removed, and cells were resuspended in clear Krebs. 1 mL cell suspension was added to 1 mL Krebs in a 35mm dish.

2.6.4.3 Fura-4F loading procedure

Unless stated otherwise, a stock solution of 2 mM Fura-4F(AM) was prepared by dissolving 50 µg Fura-4F(AM) in 25 µl anhydrous dimethylsulphoxide (DMSO), stored at 4°C. For cell loading, 15 µl of the stock was added to 5 mL Krebs (1.8mM $CaCl_2$) solution for a final concentration of 6 µM, in which cells were incubated at RT for 20 min, and resuspended after 10 min to promote dye interaction with cells, and for Fura-4F(AM) to undergo de-esterification. The supernatant was removed, and cells were resuspended in clear Krebs solution. 1 mL cell suspension was added to 1 mL of clear Krebs to a 35 mm dish and cells could settle onto the glass.

2.6.4.4 Pluronic acid (F-127)

Emulsification of Fura-4F(AM) was facilitated using 20%(w/v) pluronic acid (F-127, in 100% DMSO). Pluronic acid facilitates the solubilisation of water-insoluble dyes in cellular media by breaking up droplets of dye and coating them in polar globules, promoting dye delivery into polar membranes. Pluronic acid was later added directly to Fura-4F powder (25 µg) up to 2mM stock, to further minimise cell exposure to DMSO. The use of pluronic acid improved cell loading of AM dyes, whereby all cells loaded with the pluronic-AM dye solution produced fluorescent signals, which was not the case when using Fura-4F(AM) alone.

2.6.4.5 Dual-loading with Fura-4F(AM) and FluoVolt dyes

Pluronic acid F-127 (20% in DMSO, Thermo Fisher Scientific) was heated gently to decrease its high RT viscosity. Fura-4F(AM) powder (50 µg) was dissolved into 20% Pluronic acid F-127 (in DMSO) to the desired concentration and thoroughly vortexed in a 0.5 mL Eppendorf. FluoVolt (1 µl) was added to 3 µl of Fura-4F-AM/Pluronic mix and vortexed again until the colour turned to homogeneous orange. This mixture was added to 6mL of Krebs (1.8mM $CaCl_2$) to achieve a 1:6000 concentration of FluoVolt and 1 µM Fura-4F(AM) concentration. Cells were incubated in this solution for 25min at RT and resuspended halfway, identically to other dye-loading protocols.

2.6.5 Excitation-Contraction (E-C) uncoupling

2.6.5.1 E-C uncouplers

E-C uncouplers are commonly used in cardiac optical mapping/conduction experiments for suppression of motion artefact. The primary action of these is to suppress and inhibit muscle contraction without altering electrical activity across the myocardium. Several compounds are available including cytochalasin D (Cyto D), 2,3-butanedione monoxime (BDM) and more recently blebbistatin. BDM is non-specific, and is known to affect SERCA2 activity, limiting its usefulness (Herron, Lee and Jalife, 2012). Conversely, blebbistatin is specific to myosin II , inhibiting adenosine triphosphatases (ATPases) in an actin-detached state (Kovács *et al.*, 2004; Allingham, Smith and Rayment, 2005; Fedorov *et al.*, 2007). Its behaviour in this unbound state is advantageous because it prevents any stiffness which may result from a constant actin-myosin crosslink. Additionally, it has been extensively used in zebrafish, mouse, rabbit, human, and several other species.(Jou et al. 2010; Dou et al. 2007; Mironov et al. 2008; Fedorov et al. 2010). While blebbistatin has been reported not to cause noticeable effects on cardiac electrophysiology in the past (Fedorov *et al.*, 2007), it has more recently been shown to have some minor effects on ECG parameters and atrial and ventricular electrophysiology. Additionally, a recent study suggests that blebbistatin may have adverse effects in whole heart rabbit experiments, including APD prolongation and reduced VF threshold (Brack *et al.*, 2013). These effects are minimal compared with other E-C uncouplers (e.g. BDM) (Lou, Li and Efimov, 2011).

Another more serious disadvantage to using blebbistatin is its photosensitivity and phototoxicity. Studies have shown that both UV and blue light photo‑inactivate blebbistatin, resulting in toxicity from the production of free radicals, causing oxidative damage locally (Kolega, 2004; Sakamoto *et al.*, 2005). This E-C uncoupler was used exclusively for testing the contribution of movement to fluorescent traces in contracting single cells, and not for any physiologically relevant phenomena. While investigating the impact of motion artefact on fluorescence recordings, cells were incubated in blebbistatin solution (3 μM, for 25 min).

2.6.6 Fluorescence recordings

2.6.6.1 Lens aperture and light collection

The amount of light collectable by a microscope objective is expressed as *numerical aperture* (NA). Numerical aperture is a measure of the broadness of the light cone from the focused sample able to enter and diffract through the front lens. NA is the product of the refractive index of the medium through which the sample is observed (e.g. air, oil) and the maximum angle of light entering the lens with the sample in focus (Equation 1).

$$NA = n.sin\theta$$

Equation 1 Numerical aperture equation. Equation for Numerical aperture, where n is the refractory index of the medium between the objective and the sample (air = 1.00) and θ denotes half the maximum angle of light entering the objective with the sample in focus.

The visual field brightness (B) of the microscope is proportional to both the numerical aperture and the magnification of the objective used (Equation 2). The maximum NA available for air objectives is 0.95. Water- or oil-immersed objectives are required to further increase light collection efficiency, by increasing the refractory index of the medium between the objective and the sample. Figure 2.7 shows a comparison of light collection between two objectives. The higher NA (0.95) objective was used throughout this thesis.

$$\mathbf{B} \propto \frac{NA^2}{M^2}$$

Equation 2 Relationship of brightness index respective to aperture and magnification. Brightness index equation, demonstrating increased aperture or decreased magnification increases overall brightness.

2.6.6.2 Selection of optics

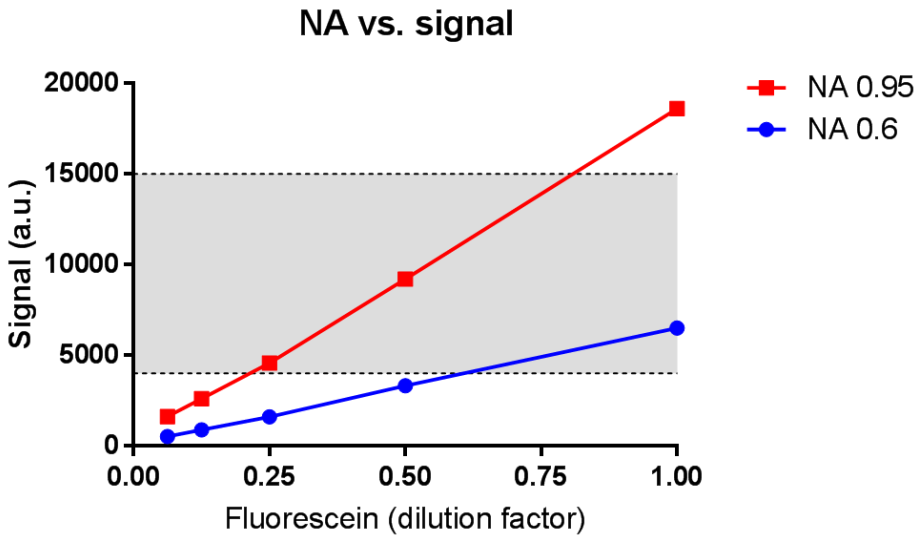

Figure 2.7 Light collection efficiency of high NA lens. Fluorescein signal (a.u.) with incremental dilutions was compared between two 40X objectives (UPlanSApo, cat no. AMEP4754). Under identical 470 nm illumination, the high aperture objective (red; NA 0.95) collects over 3 times more light than the lower aperture objective (blue; NA 0.6) at all dilutions tested. Typical signal intensity encountered experimentally shown in grey.

As shown in Figure 2.7, solutions of serially diluted fluorescein (1, 1/2, 1/4, 1/8, 1/16) were used to compare light-collection efficiency between two objectives of identical magnification. The highest concentration of fluorescein was selected close to the saturation point of the light-sensing apparatus to compare each lens over the full range of the signals typically encountered experimentally. Using higher NA objectives allowed lower concentrations of fluorophores to be used, along with lower excitation power, in turn resulting in less photodamage and cytotoxic effects for a given signal-to-noise ratio (SNR).

See section 3.6.2 for lens selection rationale.

2.6.6.3 Voltage recordings

Following excitation at 470 nm wavelength, fluorescent signals emitted by voltage-sensitive dyes (di-4-ANEPPS and FluoVolt) were respectively sampled above 585 nm at 10 kHz with photo-multiplier tubes (PMTs). This sampling rate is very high and allows sub-millisecond temporal resolution of voltage changes (dye response being in the µs range), provided subsequent trace filtering is chosen appropriately. This was essential to accurately capture the upstroke of the ventricular action potential, which routinely occurs in the range 1-4 ms.

2.6.6.4 Calcium recordings

The calcium-sensitive dye Fura-4F(AM) was excited alternately at 340 nm and 380 nm, and the resulting emissions at 510 nm recorded using a PMT as described above. The sampling rate for Ca^{2+} fluorescence was 500 Hz, allowing a 2 ms temporal resolution of Ca^{2+} kinetics inside the cell. The reason for this 20-fold lower rate compared to voltage is to allow for sequential excitation of the fluorophore at each wavelength without causing cross-excitation (See Figure 2.8).

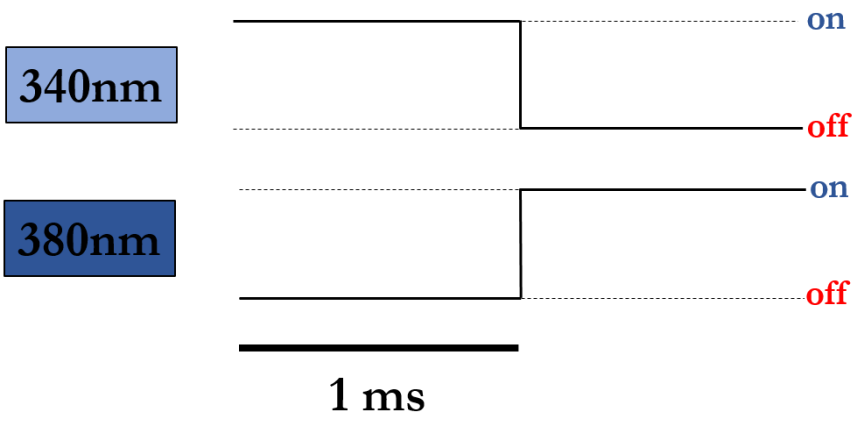

Figure 2.8 Fura-4F dual-wavelength excitation protocol. Excitation protocol for Fura-4F(AM). 340m LED is switched on for 1 ms, immediately switched off as the 380nm LED is switched on for 1 ms. The resulting ratio can consequently be sampled at a maximum resolution of 1 point every 2ms (500Hz).

While excitation occurred for a duration of 1ms, signal was recorded in the last 0.5 ms interval to allow the LED to reach steady state.

2.6.6.5 Simultaneous voltage and calcium recordings

A new excitation protocol was devised for cells loaded with both voltage- and calcium-sensitive dyes (FluoVolt and Fura-4F(AM)). Excitation at each wavelength (i.e. 470 nm, 340 nm, 380 nm) was achieved sequentially. Obtaining voltage and calcium information nearly simultaneously constrained the sampling rate of each recording. Triple-excitation traces were recorded at 333Hz, recording a fluorescence value every 3ms for all three channels, respectively (see Figure 2.9).

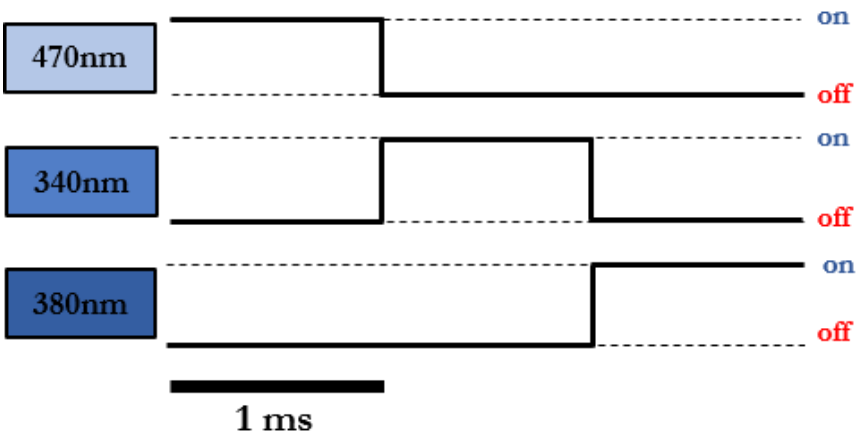

Figure 2.9 Triple excitation protocol. Triple excitation LED protocol for Fura-4F and FluoVolt. Each LED (470 nm, 340 nm, 380 nm) is turned on for 1 ms and off for 2 ms in immediate succession. This excitation protocol reduces the maximum temporal resolution to 333 Hz.

2.6.6.6 Fluorescent signal analysis: Voltage and Calcium

Trace analysis was conducted using CellOPTIQ software. The raw, unfiltered trace was baseline-subtracted (fitting and subtracting an exponential decay), filtered using 3-point, 15 pass filter (moving 3-point average, applied 15 times). This was the lowest level of filtering possible without compromising measurements of the AP upstroke (See Figure 4.3). The upstroke and repolarisation phases were filtered adaptively to a target smoothness, measured by the number of curve inflections. A 3-point boxcar was used as it is the smallest symmetrical odd number (5, 7…etc could also be used). Averaging points on either side of each point preserved the time-base (i.e. an average of only 2 adjacent points would artificially create a value in time in between them). The number of passes of the boxcar for all experiments (15) was selected as it was the minimum filtering required for the vast majority of signals to be analysable. Lastly, applying incrementally larger boxcars repeatedly is quickly outperformed computationally by applying a small 3-point average iteratively. Values used in analysis were T_{Rise} (upstroke time from 10% to 90% depolarisation), and $APD_{30,50,90}$ values, representing time (ms) from upstroke to several degrees of repolarisation.

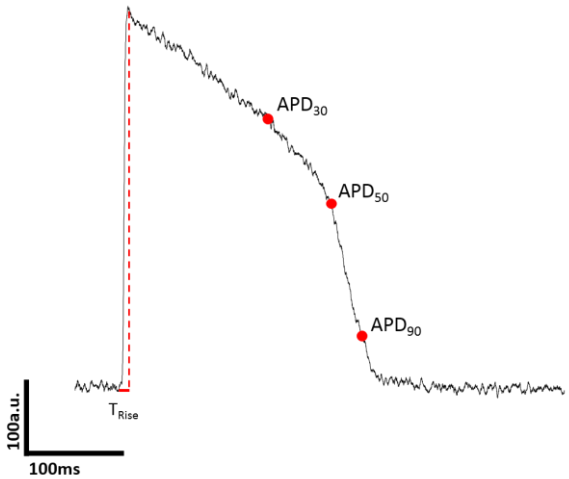

Figure 2.10 Action potential recorded parameters. Example of averaged action potential labelled with main variables recorded. TRise was measured from 10% depolarised to 90% depolarisation of maximal amplitude. APD values (e.g. APD_{90}) represent time from upstroke to % repolarisation from peak fluorescence.

To describe the general shape of phase 3 (repolarisation phase), an index of triangulation was calculated using an early (APD_{30}) and a late (APD_{90}) repolarisation metric (see Figure

2.10). This index was normalised for AP duration as follows: Triangulation index = $\frac{APD_{90}-APD_{30}}{APD_{90}}$, demonstrated in Figure 2.11.

This index is commonly seen in literature, generally expressed as the difference between APD_{90} and APD_{30} in ms (Hondeghem, Carlsson and Duker, 2001; Grunnet, 2010; Trenor *et al.*, 2013; Zhu *et al.*, 2016). Not accounting for action potential duration can, however, be misleading, and while this method is appropriate for comparing the shape of action potentials with similar APD_{90}, it quickly fails with relatively small differences in duration, over-reporting triangulation in long APs and equally under-reporting triangulation in short APs. In this way, normalising the index for APD ensures it remains sensitive to changes in shape, irrespective of duration. Some groups do report APD-corrected triangulation (Blinova *et al.*, 2018), however there is a need for standardisation of this index, frequently used to describe the arrhythmogenicity of AP wave-forms.

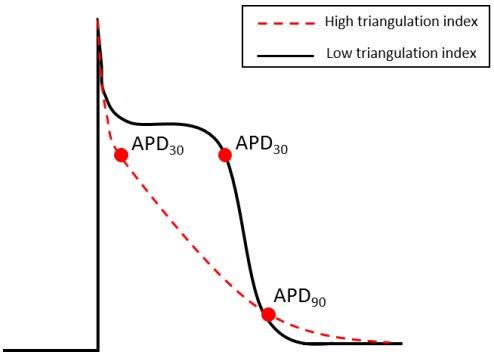

Figure 2.11 Diagram of AP triangulation case. Diagram of two action potentials with identical APD_{90} values. The black trace has a low triangulation index compared to the dashed red AP. The index provides information about the degree of plateau present, normalised for APD.

Calcium traces were subjected to the same process as described above, 340nm and 380nm traces expressed as a ratio $\frac{340nm}{380nm}$. Values extracted from this analysis were baseline, TRise,

amplitude, and CD values (calcium decay), representing decay of calcium following contraction, in percentage from maximum (see Figure 2.12).

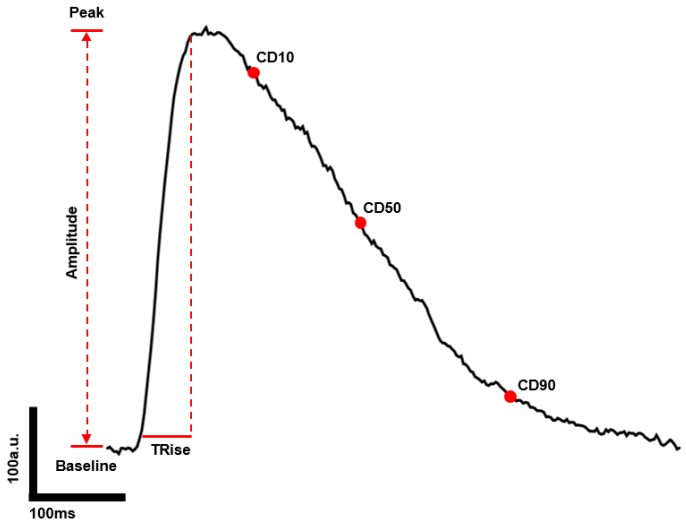

Figure 2.12 Calcium transient recorded parameters. Example of an averaged calcium transient labelled with variables of interest. Baseline denotes "resting" diastolic Ca^{2+}. Peak is the maximum fluorescence value, or systolic calcium peak. TRise describes time (ms) from baseline to maximal Ca^{2+}. CD values time to 10,50,90% Ca^{2+} decay.

2.6.6.7 Analysis of cell contraction using ImageJ

Contraction measurement in cardiomyocytes was achieved using sarcomere length measurement. High-speed (100 fps), high resolution (2048x2048 pixel) video was recorded using a Hamamatsu camera and a 40X, 0.95 NA objective (Inverted Olympus microscope). Image sampling durations were chosen to allow a minimum of 5 beats to be recorded and subsequently averaged for analysis, at all pacing frequencies.

Using the macro SarcomereLength created in ImageJ by Dr Francis Burton, each stack of images (typically 500) was analysed by manually placing a linear selection perpendicular to the cell sarcomeres, to capture the cleanest isotropic contraction possible. Line length was controlled by the operator and varied depending on cell size (minimum of 100 pixels). Line width was kept constant at 50 pixels, reducing influence of pixel noise by averaging pixels across the width (see Figure 2.14).

2.6.6.8 Sarcomere length analysis

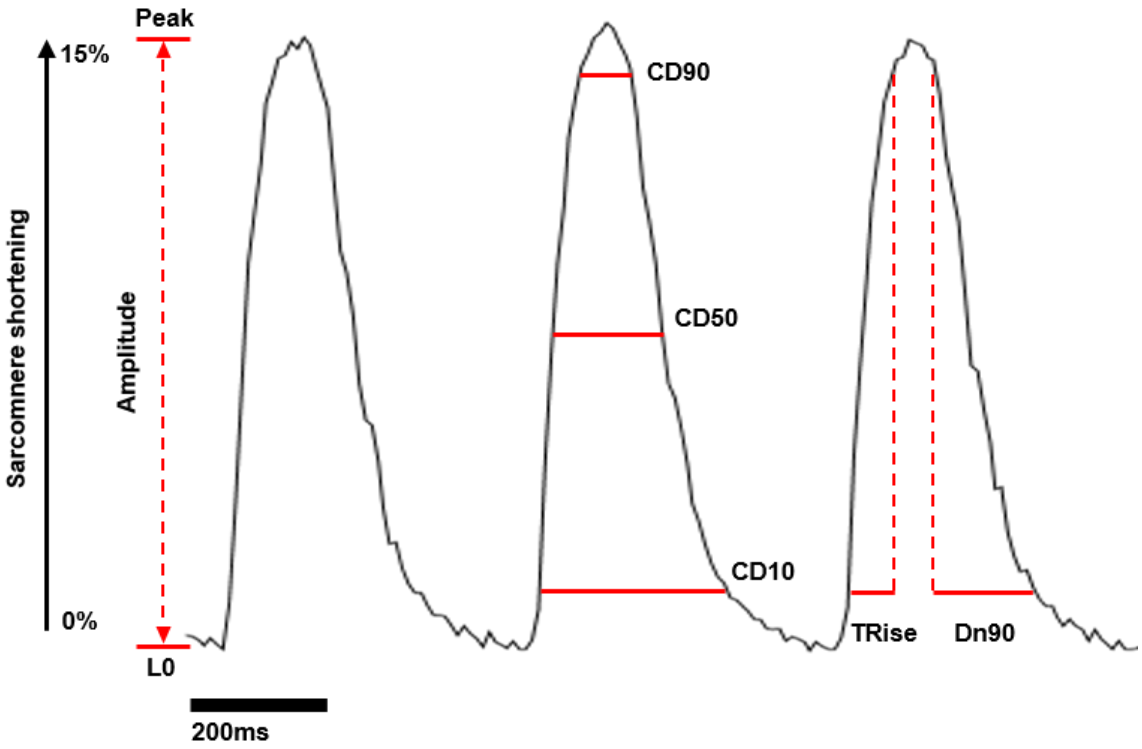

Figure 2.13 Contraction profile recorded parameters. Example train of 3 contractions listing variables recorded for contraction analysis. **L0** Mean distance between sarcomeres in the cell at maximal relaxation (µm). **Amplitude** Extent of sarcomere shortening (expressed as µm or % relative to peak). **CD10** Duration from 90% contraction to 10% relaxation (ms). **TRise** Time from 10% contraction to 90% (ms). **Dn90** Time from 90% contraction to 90% relaxation (ms).

a.

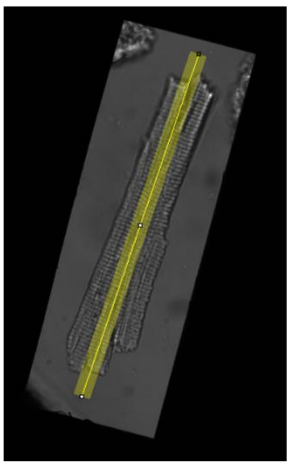

b.

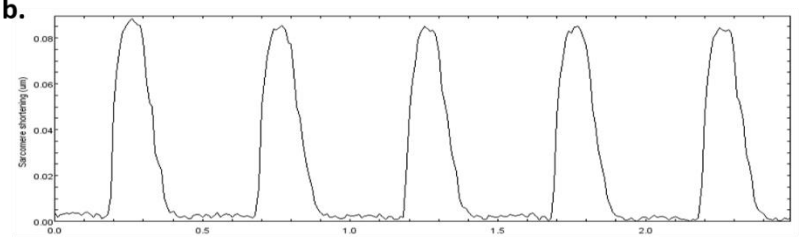

c.

	Label	T0	Interval	L0	Amp	TTP	Up90	Dn90	CD10	CD25	CD50	CD75	CD90
1		160.000	500.000	1.967	0.087	100.000	35.764	71.248	181.952	164.377	133.710	95.015	74.941
2		670.000	480.000	1.966	0.084	100.000	40.850	76.924	191.287	164.973	133.226	96.827	73.513
3		1160.000	500.000	1.967	0.084	90.000	43.481	76.364	187.829	167.038	133.750	91.963	67.984
4		1670.000	470.000	1.968	0.085	100.000	40.535	74.249	188.422	163.548	130.174	98.116	73.638
5	Mean	915.000	487.500	1.967	0.085	97.500	40.157	74.696	187.373	164.984	132.715	95.480	72.519
6	SD	648.100	15.000	5.546E-4	0.001	5.000	3.213	2.572	3.916	1.489	1.711	2.668	3.092
7	Min	160.000	470.000	1.966	0.084	90.000	35.764	71.248	181.952	163.548	130.174	91.963	67.984
8	Max	1670.000	500.000	1.968	0.087	100.000	43.481	76.924	191.287	167.038	133.750	98.116	74.941
9	Average			1.967	0.085	100.000	41.299	76.186	188.896	164.745	130.765	95.880	71.411

Figure 2.14 Measurement of sarcomere length. Diagram showing cell contraction analysis. (a) Shows a cardiomyocyte and the line placement perpendicular to the sarcomeres. (b) Shows the 5 second trace generated using the ImageJ plugin. (c) Table of contraction kinetics values derived from the plotted trace. The mean kinetics of 5 contractions was collected for data analysis.

2.6.6.9 Calibrating intracellular calcium using ratiometric dye Fura-4F (AM)

Using the ratiometric properties of Fura-4F, the absolute concentration of calcium in cells can be calculated by calibrating the dye fluorescence at both excitation wavelengths (340 nm and 380 nm, respectively), expressed as a ratio. To measure absolute intracellular [Ca^{2+}], a calibration curve was generated using precise concentrations of free calcium ions ranging from nM to mM. By knowing the dissociation constant of Fura-4F (K_d), as well as the ratio value for maximum and minimum fluorescence emitted by the dye in presence of 0 mM Ca^{2+} and 10 mM Ca^{2+}, the absolute calcium concentration inside the cell can be calculated (Equation 3).

The K_d value is dependent on excitation and sampling efficiency of Fura-4F fluorescence (i.e. LED power, excitation range (nm)). For that reason, it is sensitive to different optical setups and consequently is *specific* to the optical setup it is measured by.

2.6.7 Optical system Kd calculation

Three solutions containing 20 µM of the calcium ionophore calcimycin (A23187) were prepared. R_{MIN} solution contained 5 mM EDTA. R_{MID} solution contained EDTA and CaEDTA at a 1:1 ratio, and R_{MAX} solution contained 10 mM CaEDTA.

To calculate the free calcium present in solution based on these solutions, the free-calcium calculator REACT was used (Smith, 1983).

$$[Ca^{2+}] = K_d * \beta * \frac{(R - R_{\min})}{(R_{max} - R)}$$

Equation 3 Kd equation. Calibration equation for calcium concentration as a function of fluorescence recorded from the sample at 3 points (Rmin, Rmid, Rmax). (Equation from (Grynkiewicz, Poenie and Tsien, 1985)

Adult CMs were isolated and remained in KB solution (0 mM Ca^{2+}) at 37°C. Cells were seeded at low density onto 35 mm MatTek dishes and left to settle. The background fluorescence was recorded by shaping a rectangular iris to fit the cell, and recording the Fura-4F ratio of the area immediately next to it. The cell was then illuminated with the 340 nm/380 nm excitation protocol previously described. Half the volume (1 mL) of the dish was removed and replaced with a 2X R_{MID} solution. The same protocol was applied for R_{MAX}, with a final concentration of calcium of 10 mM.

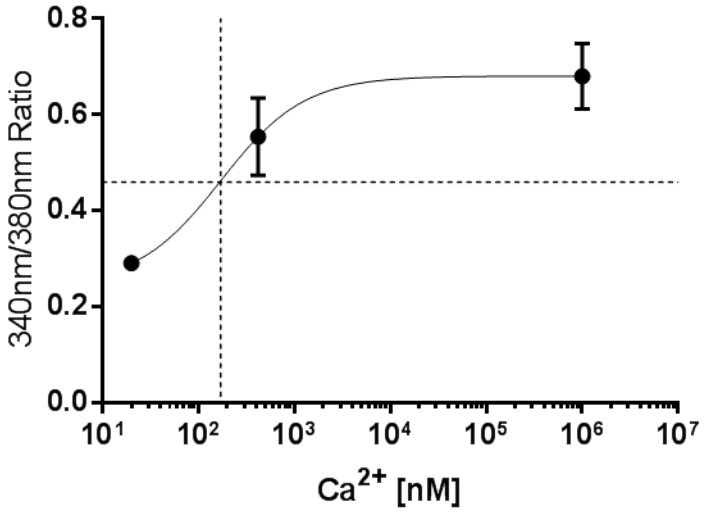

Figure 2.15 Fura-4F fluorescence vs. [Ca^{2+}]. Background-subtracted fluorescence ratio (340 nm/380 nm) of Fura-4F at three known calcium concentrations. (Rmin = ~20nM; Rmid = 420nM; Rmax = 10mM). Kd estimate shown by dotted lines.

The relationship between calcium concentration inside the cell and the ratio of emitted light from Fura-4F at 340nm and 380nm excitation is shown in Figure 2.15. Using the midpoint ratio along the sigmoidal relationship, the Kd was found to be 177 µM. This value is however likely to be a product of the β value (system-specific) and the Kd of Fura-4F. More work is required to calculate the absolute calcium concentration in cells using ratiometric Fura-4F measurements, however the kinetics of calcium transients recorded are unaffected by this.

2.6.8 Statistical analyses

2.6.8.1 Standard statistical tools

Data are presented as mean ± standard error of the mean (SEM) unless otherwise stated. Statistical analyses were performed using GraphPad Prism 7. Single comparison of means was conducted using standard 2-tailed t-test (paired where appropriate). For parametric data, one-way ANOVA followed by multiple comparison tests were used to compare three or more groups of data. For non-parametric, independent datasets, Mann-Whitney U test was used. All tests were set at a significance threshold of $P \leq 0.05$. (Significance stars: *, **, *** denote a p-value less than or equal to 0.05, 0.01, and 0.001, respectively).

2.6.8.2 Hierarchical Statistics

The statistical approaches listed above assume independence in datasets and ignore potential clustering of datasets, however when comparing two populations of cells within the same heart (e.g. endocardium and epicardium), these regions may well be more similar to one another than to another animal's, and consequently cannot be considered independent. This concept of data clustering requires higher-level analysis, considering both the data clustering present within sets, but also the size of each set relative to the total sample size, to avoid skewing the results towards the set with the highest number of measurements. Sikkel et al. (Sikkel *et al.*, 2017)have demonstrated that in multi-level datasets, and more specifically isolated CM studies, improper statistical approaches can lead to false-positive results, as well as abnormally small P values to be reported. Conversely, false negatives can and do occur just as easily (i.e. when the difference between sets is overshadowed by the intrinsic variation in higher level sets.).

For example, Coulibaly, Chen-Izu and Izu, (2017) have outlined the issue of over-estimating experimental N-numbers, by counting multiple measurements from the same heart as independent. To illustrate this point, they use the example of three rats, each of which provides 10 measurements of blood glucose (see Figure 2.16). To describe the mean rat population blood glucose, we should use n = 3, and not n = 30, as each group of 10 measurements only describes variation within one animal.

In this context it is quite clear that the number of measurements taken from each rat, no matter how large, can only give a better estimation of this specific animal's blood glucose, and not be counted toward the total population mean as more than one measurement. By

increasing the sample size of each animal, the standard error of the mean of the whole population would tend to zero, artificially increasing the probability of statistical difference with another group.

In the context of AP duration in a population of cells from specific subregions of the same ventricle, increasing sample size does cause a reduction of the SEM, but additionally (i) allows better estimation of the true mean of the population and (ii) provides a representative measure of the variation present *between cells*.

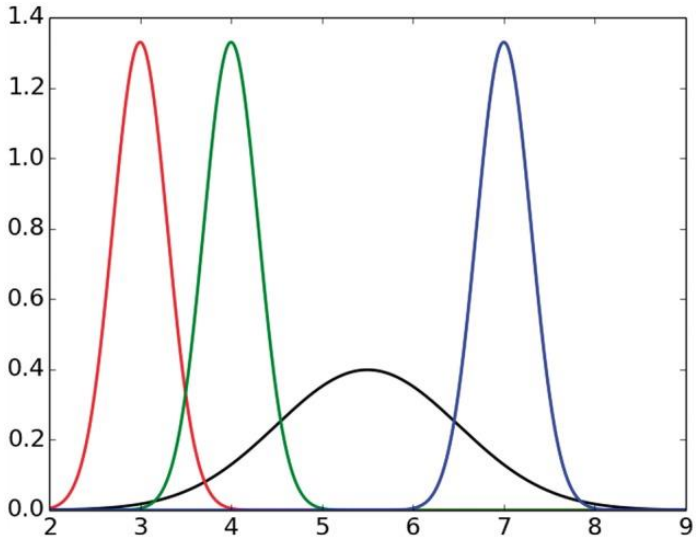

Figure 2.16 Illustrative example of clustered datasets Hypothetical distribution of glucose concentrations in three rats (red, green and blue curves) and of the population. (Figure taken from Coulibaly et al. 2017)

In this thesis, hierarchical testing was used to assess the statistical differences between clustered sets (cells originating from different regions of the same heart) using published code written in R (Sikkel *et al.*, 2017). Sikkel et al. propose a hierarchical analysis of clustered datasets as a significant improvement over conventional approaches, shown by the χ^2-2LL (deviance) criterion (i.e. provides a superior description of the data than t-test or ANOVA). The hierarchical test is compared to the "common test", which assumes data collected from each animal is independent (i.e. endocardial cells considered independent from epicardial cells within the same heart), and determines whether the latter better fits the data using χ^2-2LL. Once it has been established the data is clustered in nature, the p-values generated by comparisons of pairs of variables (e.g. endocardium vs epicardium) are multiplied by the number of comparisons (animals) per dependent variable. A comparison-weighted p-value is then generated, more accurately representing the difference present between compared sets. (Code available in Appendix, p139)

Chapter 3: Development of a medium-throughput, optical voltage and calcium measurement technique

3.1 Background

Increasing sample size per experiment is highly sought-after in the field of single-cell electrophysiology. Current methods yield high-quality measurements, but lack efficiency in their use of resources, especially animals and time. Studying isolated cardiomyocyte populations from individual animals is problematic. Firstly, cellular isolation via enzyme dissociation is widely known to be both challenging and unpredictable (Louch, Sheehan and Wolska, 2011). Isolation of cardiomyocytes from cardiac tissue was developed over 40 years ago (Powel and Twist, 1976). It allowed the study of cell mechanics, electrophysiology, calcium dynamics, along with various staining techniques (IHC, protein biochemistry) to be applied to isolated cardiomyocytes from various species. The main motive for developing a technique to isolate cardiomyocytes was the impractical nature of tissue preparations for voltage clamping experiments (Louch, Sheehan and Wolska, 2011). Single cells allowed complete control over the membrane potential, and additionally permitted the study of cells deep in the myocardium which were then optically out of reach (e.g. mid-myocardial cells). A major limitation of enzymatic dissociation is membrane damage. Cells are highly sensitive to contaminants during the dissociation process, which increases the danger of membrane perforation and leakage. Regulation of age/weight of the animal, solution pH and temperature, as well as the batch of collagenase enzyme used are also variables to be considered and controlled for a successful cell isolation (Kruppenbacher *et al.*, 1993; Wolska and Solaro, 1996). Our group conducted cell isolations at 37°C both to reduce cell-exposure to non-physiological parameters, and for relevance to available literature (Bers, Lederer and Berlin, 1990; Zhou *et al.*, 2000).

As discussed previously, the extent of digestion of the heart is assessed through colour and feel of the tissue as well as time elapsed, which are arguably qualitative assessments requiring a certain degree of experience, and thus prone to experimental error. Immortal cardiac cell lines such as HL-1 have been created, however newly dissociated cells from fresh hearts are accepted to be more physiologically relevant to the myocardium than cells which have been in culture for prolonged periods (Gizak *et al.*, 2009).

3.2 Cell isolation shortcomings

Cardiomyocytes used in this work were consequently obtained through the most successful method to date, namely retrograde coronary perfusion of collagenase enzyme solution, followed by tissue dicing and agitation. This technique is thought to be superior to the

"chunk" method, where tissue is diced and agitated in enzymatic solution without perfusing through existing vasculature (Louch, Sheehan and Wolska, 2011). Despite undergoing substantial improvements over the past few decades, the available techniques were until now unable to measure the variability of cell quality following isolation due to low throughput. This being the case, patch clamping techniques have now been refined to allow high-content experiments to be carried out on individual cells. Allowing high-fidelity recordings of the membrane potential in excitable cells, the study of cardiomyocytes has largely benefitted from this.

In healthy tissue, electrical coupling of neighbouring cells via gap junctions reduces the variability of electrical behaviour observed, contrasting with a highly pronounced variability in AP durations from isolated cells from the same tissue, as demonstrated in this thesis. Quantifying this heterogeneity requires populations of cells to be sampled from individual animals, which the manual patch-clamping techniques currently do not permit. Automated patch clamping devices have become more widely available in the past 5 years, albeit at prohibitive costs, and limited to a single recording per cell, as it is a terminal procedure, mechanically breaching the cell membrane.

The following experiments used optical techniques to study isolated CM electrophysiology at higher throughput than had ever been done previously. To achieve this, the new voltage-sensitive dye FluoVolt was used to measure real-time membrane potential. Its properties were compared with the well-established voltage indicator di-4-ANEPPS. Protocols were optimised to use FluoVolt at concentrations yielding maximal signal-to-noise without causing obvious cell damage. Optics were specifically selected to further reduce photo-induced damage and increase SNR. Finally, a custom-designed stimulator/incubator bath system was developed to best accommodate the new working distance of the new objective while maintaining stable temperatures, and further improve throughput.

3.3 Section Aim

The work outlined in this chapter aimed to improve on current approaches for studying isolated CM electrophysiology, namely developing a medium/high-throughput technique to sample large cell populations (n=100-500 cells) from individual hearts by optimising optical dyes and optics, and combining the apparatus with an automated microscope stage to precisely record individual cell locations for multiple measurements. This contrasts with

current methods (e.g. patch-clamping, low-throughput optical methods) which are currently limited by small sample sizes, and single recordings per cell (i.e. 5-10 cells per day).

3.4 Hypothesis

Optimising several separate aspects of a fluorescent-based voltage measurement technique will lead to substantial increases in sample size per heart.

3.4.1 Incubator/stimulator

In collaboration with the Bioelectronics department at Glasgow University (Nosrat Mirzai and Jakub Czyzewski), we co-designed an aluminium-body stage incubator (see Figure 3.1) built to accommodate two glass-bottomed dishes (MatTek, 35 mm). Accurate temperature modulation (±0.1°C) was achieved using two Peltier units and 50 mm cooling fans. A thermistor was installed inside the incubator and a thermostat-loop controlled temperature within 1°C. The lid of the device was also machined out of aluminium for adaptable heat-modulation. Two graphite electrodes (2cm x 5cm x 2mm) were inserted through the lid and secured using either Teflon or plastic (3D-printed PLA) inserts and immersed in the cellular medium. A pacing stimulator (MyoPacer, Ionoptix) was used to generate 2 ms, 40 volt pulses at the desired frequency (1 – 3Hz).

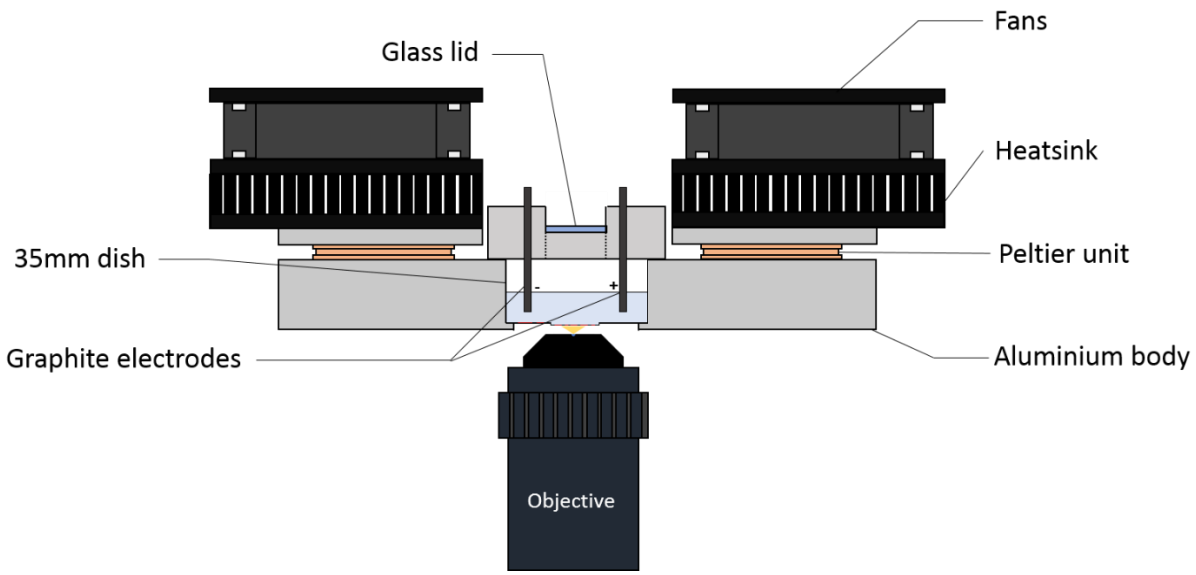

Figure 3.1 Diagram of stage stimulator/incubator bath. Two Peltier elements accurately regulate plate temperature and 50 mm fans radiate excess heat. Graphite electrodes are used to generate field stimulation inside the dish medium.

3.5 Results

3.5.1 Temperature calibration and modulation

Action potential duration (APD) is strongly influenced by slight changes in temperature. The temperature of the incubating plate was consequently thoroughly calibrated to achieve a stable temperature in the dish (37°C). The custom-built temperature incubator was incrementally heated and calibrated for dish temperature using three separate methods. The plate itself was fitted with a temperature probe, accurate within ±0.1°C. A temperature sensitive sticker was placed in the dish (±1°C; LabTemp 40), in 2 mL Krebs solution. Finally, a temperature probe (±0.1°C; Oko-labs) was submerged in the medium. The temperature setting of the plate was set as a thermostat with upper and lower limits of 1°C. The starting temperature was set at 37°C (upper limit= 38°C; lower limit = 36°C), and the dish was equilibrated for 10 min prior to each recording, incrementally to 46°C. The final plate thermostat was set to 42°C to achieve 37°C in the dish (Figure 3.2).

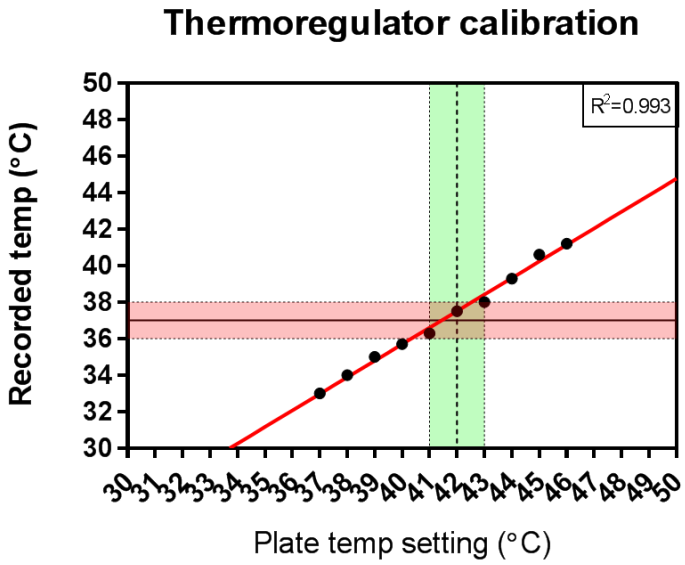

Figure 3.2 Temperature regulation of dish incubator. Calibration of plate temperature with recorded cellular medium temperature using temperature probe. XY plot shows plate temperature setting (thermistor) against actual recorded temperature inside dish using Oko-Labs probe. Incremental temperature measurements were taken from 37°C to 46°C thermistor temperature. In *red* is the acceptable temperature range for experimentation, and in *green* the upper and lower thermostat limits imposed on the temperature controller.

Testing the thermoregulating plate showed the temperature of the Peltier elements required was strongly linearly correlated with the dish temperature, however due to thermal losses, a

+5°C offset was required to achieve 37°C in the dish. Temperature regulation was thermostatically regulated within 1 degree Celsius (e.g. For 37°C, plate temperature was set to Low = 41°C; High = 42°C).

As the temperature-sensitive stickers agreed with the Oko-Labs probe, they were used as a convenient method to ensure successful temperature equilibration prior to each experiment.

3.5.2 Temperature dependence of action potential duration

To test temperature modulation and repeated voltage measurements in isolated cells, a group of FluoVolt-loaded isolated cardiomyocytes were serially paced at 2 Hz at five incremental temperatures. Cells were equilibrated for 10 min at each temperature step prior to recording (see Figure 3.3 below).

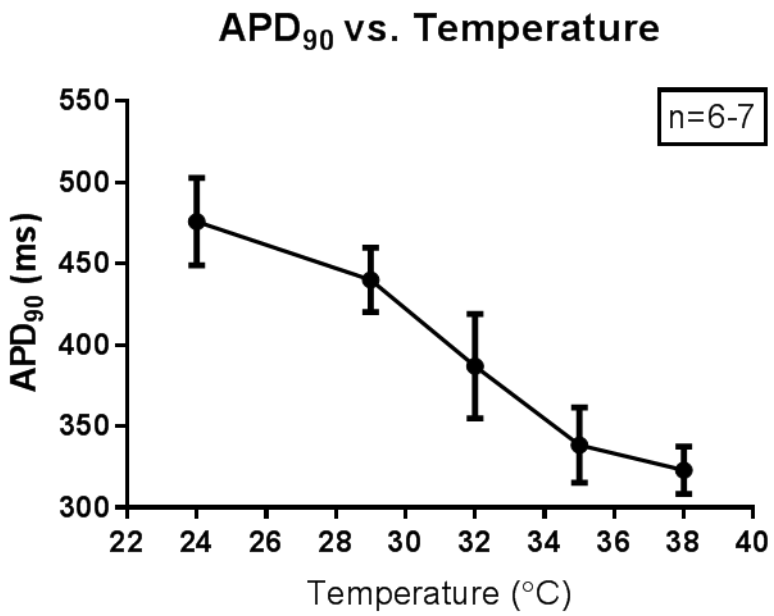

Figure 3.3 Demonstration of APD temperature dependence. X-axis shows incubating plate temperature (mean ± SD shown).

A group of seven cells were paced at 2Hz at 5 incremental temperatures, ranging from 28°C to 38°C (Figure 3.3). Action potentials were recorded at each time-point to demonstrate the critical importance of accurately controlling the temperature of the dish during the experiment. This simple demonstration illustrates the importance of accurate temperature modulation in this type of experiment. Furthermore, this shows the reliability of this method

by performing repeated fluorescent measurements of the same cell 5 times over a 60 min period without causing cell death or APD prolongation.

3.5.3 Temperature equilibration period

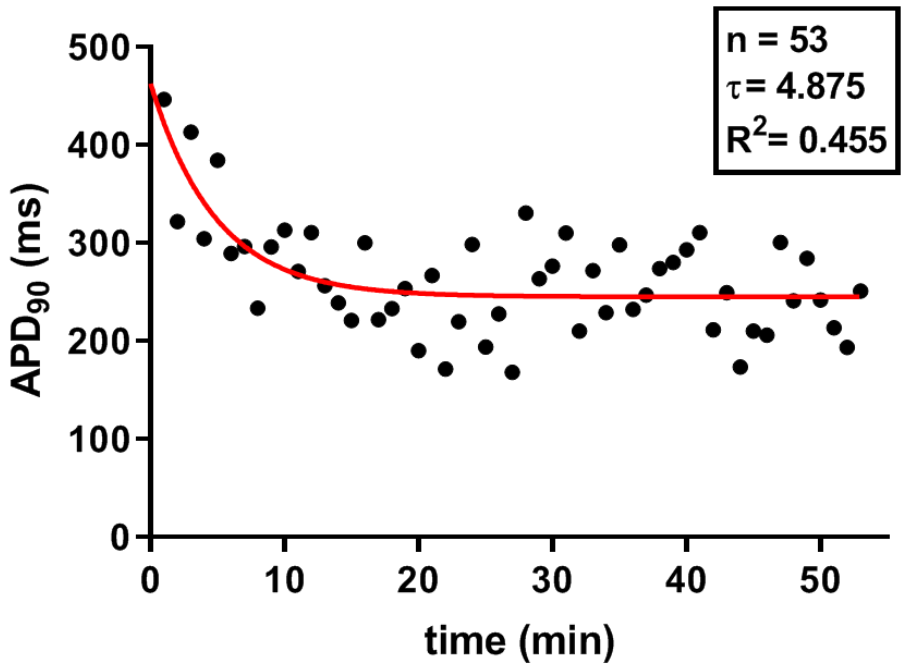

Figure 3.4 Temperature equilibration effect on APD. Example of temperature equilibration effect on APD measurements over time (Temperature plate set at 37°C). A single-phase exponential decay regression was fitted to sequential cell recordings illustrate the initial temperature equilibration in the dish in the first 10 min.

Figure 3.4 outlines the importance of temperature equilibration prior to making measurements of APD_{90} in isolated cardiomyocytes. The experimental protocol was subsequently standardized to begin with a minimum of 10 min incubation, and 5 min electrical stimulation prior to recording (see Figure 5.3).

3.5.4 Experiment duration and APD drift

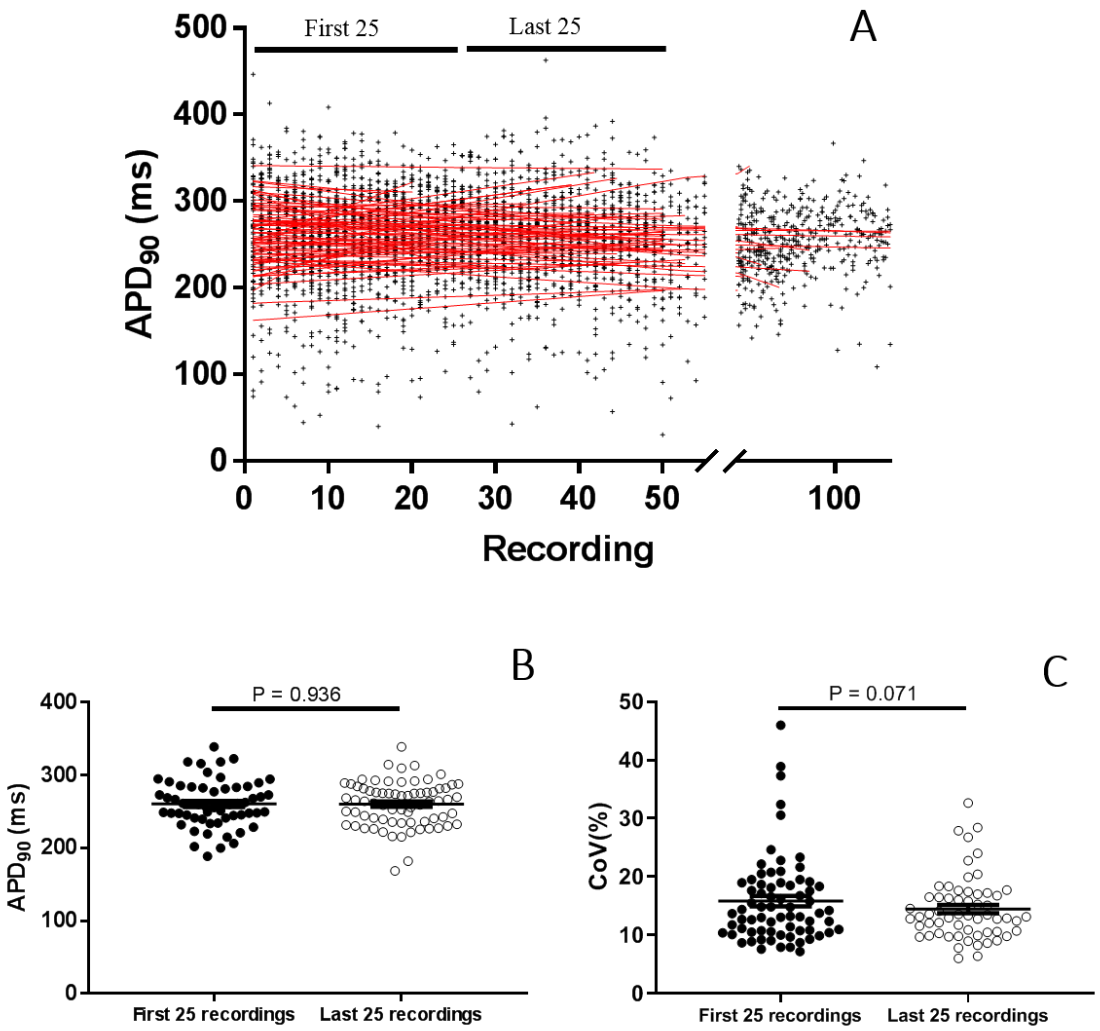

Figure 3.5 APD stability over variable experimental time. **A.** Action potential duration plotted against recording order in 75 separate incubations (n_{cells} = 3776) of variable duration (15min – 180min). A linear regression was fitted to the APD in each dataset. There is no evidence of APD drift as a function of time spent incubating. The segmented x-axis (>100) shows the few cases where over 100 recordings were made in a single dish, with an emphasis on the vast majority of experiments (≤50), where ~50 recordings were made before changing cell batch. **B.** The APD_{90} of the two groups was compared and no difference was found (P>0.05; paired t-test). **C.** Heterogeneity was assessed by comparing the coefficient of variation of the 1st to the 25th recording and the 26th to the 50th, respectively. No difference between groups was found (mean ± SEM shown, paired t-test).

Cell viability and AP consistency over the duration of experimental time was assessed using all single-cell optical recordings acquired throughout this thesis, whereby each cell dish yielded cell APD recordings (from ~30 to >100) made in series over time . The AP duration was plotted in order of recording (each cell typically took ~20s – 60s to locate and record)

and no drift or change in variability was observed across hundreds of cells in several hearts (see Figure 3.5, panel A). In each experiment, a linear regression was fitted to each APD_{90} population of recordings from individual cells which were chronologically recorded. In ~70% (50/71) cases, the slope was not significant from zero (i.e. no APD drift over time). In the remaining 30% of cases where it was significantly different from zero, 47% (10/21) had a positive slope and 53% (11/21) had a negative slope. As it was suspected that time post isolation would affect cellular health and potentially APD, and consequently during experiments involving regional comparisons, a maximum of 30 min (~50 recordings) per dish was used to minimise potential cell deterioration during incubation. Furthermore, in experiments comparing several conditions (e.g. endocardial vs. epicardial cells) the order was randomized for each experimental repeat, ensuring time was not a function of any differences found between groups. As cellular heterogeneity was also later assessed, the variability of APD over time was assessed by comparing the mean APD_{90} and coefficient of variation of the early recordings versus the later recordings within a same incubation (see 3.5.4, panel B and C, respectively). There was no significant change in APD or heterogeneity as a result of incubation duration.

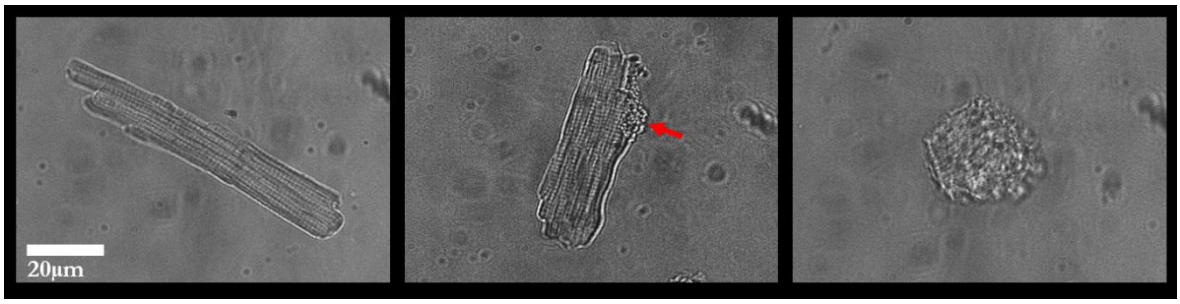

Figure 3.6 Progressive stages of cell deterioration. Intact cell (**left**) with clearly identifiable cell edge and parallel sarcomeres. (**center**) Cell edge is beginning to show signs of membrane blebbing (arrow). (**right**) Hypercontracted cell. These balled-up myocytes would often still display signs of electrical activity and must consequently be entirely excluded from the field of measurement.

After cells are enzymatically isolated, they begin to gradually deteriorate over several hours (see Figure 3.6, center). A large proportion of the total number of cells isolated die from membrane damage, and consequently a common criticism of isolated cell studies is that the surviving population of cells may not be representative of the total population present within cardiac muscle. The selection of surviving cells in the dish was made based on the most dependable characteristics indicating CM health *in vitro*. Namely, these are rod-shape, clear

striations, sharp cell edges, quiescence in normal Ca^{2+} conditions, and synchronous response to electrical stimuli (Louch, Sheehan and Wolska, 2011).

3.5.5 Dye excitation and AP prolongation

Illumination of dye-loaded cells necessary for dye excitation induces photodamage through formation of reactive-oxygen-species (ROS) and free radicals (Schaffer *et al.*, 1994). While antioxidants have been used to reduce the oxidative photo-damage associated with fluorescent probes, a far more efficient method to overcome this problem is to reduce dye concentration and improve light collection. Optimising dye concentration was therefore critical to prevent damage induced APD prolongation (see Figure 3.7). Manufacturer-recommended 1:1000 FluoVolt concentration proved far too high, and caused action potential prolongation and cell quiescence or hyperpolarisation within seconds of illumination. Using FluoVolt at 1:6000 did not prolong the action potential, following up to a full minute of continuous illumination, while retaining a superior SNR than di-4-ANEPPS.

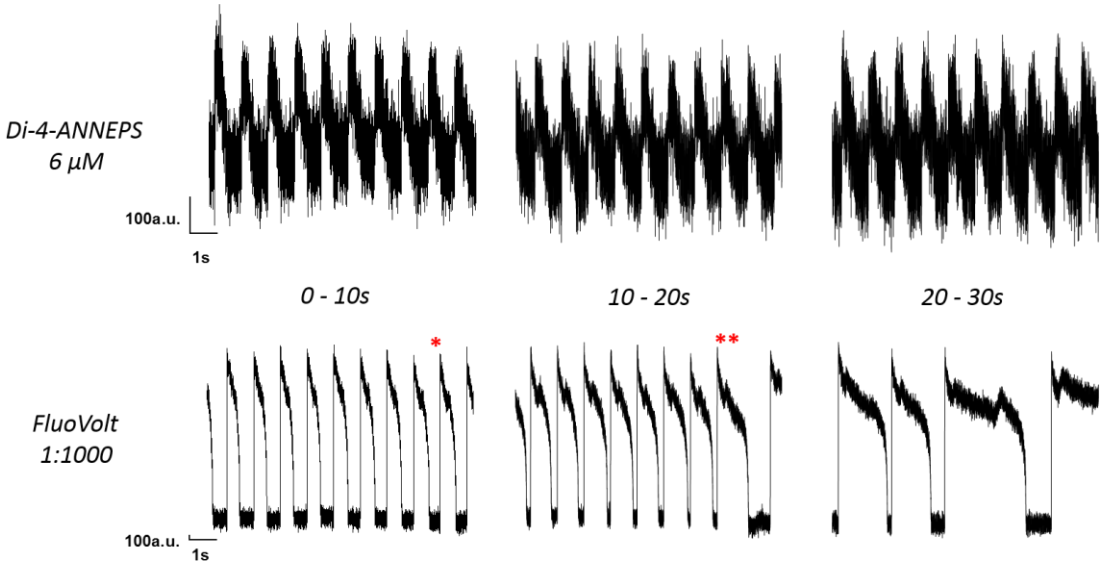

Figure 3.7 APD prolongation with FluoVolt. Example AP train of two cells (top & bottom, respectively) separately loaded with 6 µM di-4-ANEPPS or 1:1000 FluoVolt. (*) FluoVolt show superior SNR, however over only 10s there is evidence of AP prolongation. (**) The AP continues to prolong, exceeds 1000ms (CL) after less than 20s, and consequently fails to repolarise before the pacing stimulus. From 20s to 30s, action potentials prolong beyond several seconds, eventually leaving the cell in a permanently hyperpolarised, inexcitable state.

Figure 3.7 shows two cells subjected to three immediately sequential, 10-second illuminations using 470 nm LED light. All traces were filtered identically (10-point

averaging). Di-4-ANEPPS displays poor signal-to-noise compared to FluoVolt, and APD does not appear prolonged following 30 seconds total illumination.

3.5.6 SNR testing: di-4-ANEPPS vs. FluoVolt

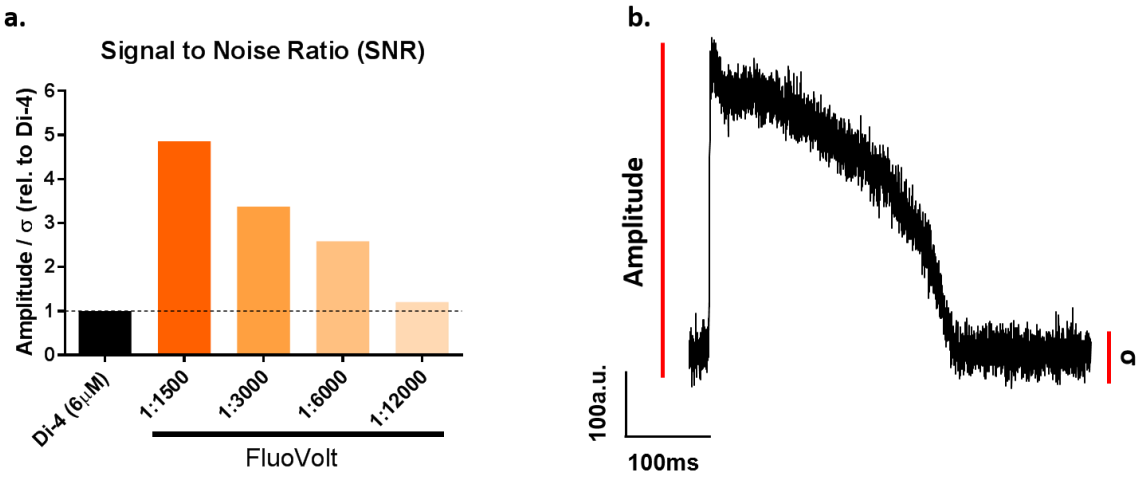

Figure 3.8 Comparison of Di-4-ANEPPS and FluoVolt signal-to-noise. (a) Signal-to-noise ratio (amplitude/noise) expressed as a relative comparison to di-4-ANEPPS (6µM) and several dilutions of FluoVolt. FluoVolt was superior at every tested concentration with respect to SNR. (b) Example action potential trace showing amplitude and noise (standard deviation of noise).

Discerning signal from noise is easier when using fluorophores with high ΔF/F per mV. The more efficient the fluorophore, the smaller amount of illumination required to produce an analysable signal. Comparing the new voltage-sensitive dye FluoVolt to an established dye (di-4-ANEPPS) determined FluoVolt was over 4 times brighter at the recommended concentration (1:1500) than di-4-ANEPPS (6 µM) (see Figure 3.8). Due to the known AP prolonging effects demonstrated previously, 1:6000 concentration was chosen as it did not cause AP prolongation with increased illumination time

3.5.7 Positive staircase testing

Adult cardiomyocytes exhibit a positive gain in fractional shortening with increased pacing frequency. This is called the positive staircase effect, or Bowditch effect in the whole heart. It is also known as the Treppe effect (Treppe is German for stairway). Generally following increased sympathetic stimulation, diastole decreases in duration, which overwhelms the Na^+/K^+ ATP-ase in its ability to extrude the Na^+ brought in by the sodium-calcium exchanger (NCX). One of the mechanisms through which the staircase effect occurs is through a build-up of calcium within the cell. NCX brings 3 Na^+ ions down their concentration gradient (inwards) in exchange for one Ca^{2+} ion to flow out. In this case, unusually high concentrations of Na^+ inside the cell decreases the efficiency of NCX, increasing intracellular Ca^{2+} concentration, where it can trigger CICR and activate myofilaments more readily, thus increasing inotropy. In isolated myocytes undergoing no external forces from neighbours as they would in tissue, this translates to increases in fractional shortening with increasing pacing frequency. This effect has been observed at the organ level, at the tissue level in papillary muscle and trabeculae, as well as in single cells. (Gibbons and Fozzard, 1975; Wang *et al.*, 1988; Shiels, Vornanen and Farrell, 2002).

To assess the impact of FluoVolt on cell physiology, the staircase effect was used as a gauge of cellular health. Cells loaded with fluorescent dyes were subjected to a triple-frequency pacing protocol, during which both voltage and contractility metrics were recorded (see Figure 3.9).

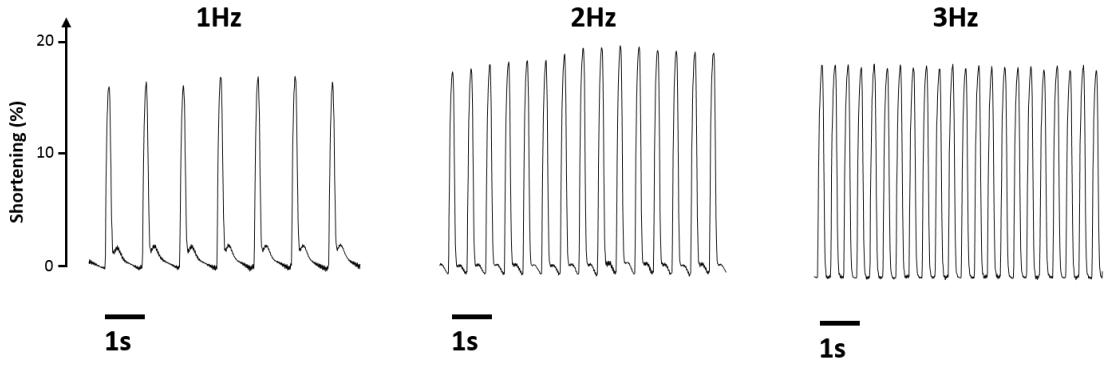

Figure 3.9 Positive staircase effect in isolated rabbit CM. Example traces of fractional shortening in a field-stimulated cardiomyocyte at 3 incremental frequencies. The amplitude of contraction increases from 1 Hz to 2 Hz, and does not significantly increase in all cells from 2 Hz to 3 Hz (See Figure 3.10)

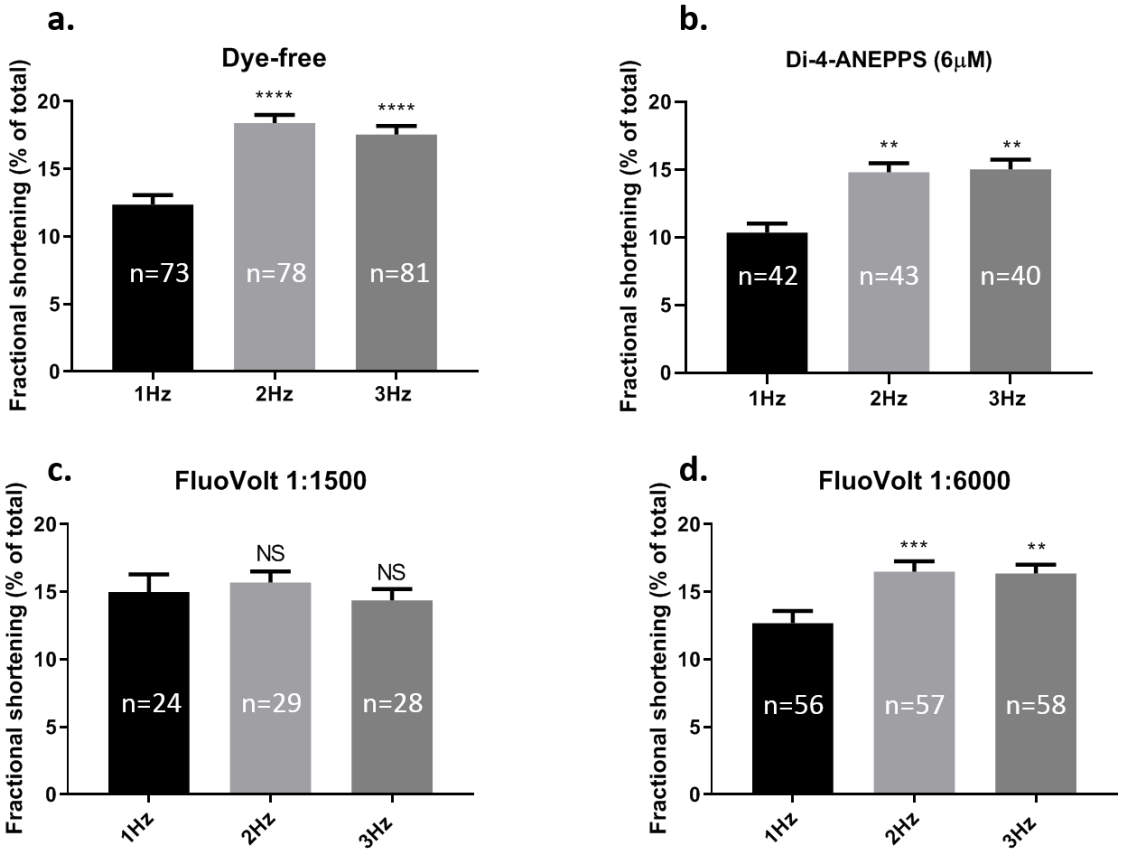

Figure 3.10 Effects of voltage-sensitive dye-loading on staircase effect. (**a**) Control cells (dye-free) show an average increase in shortening amplitude with an increase in pacing frequency from 1Hz to 2Hz, but not 2Hz to 3Hz. (**b**) Cells loaded with 6 μM di-4-ANEPPS also display a positive inotropic effect ($P<0.01$). (**c**) Cells loaded with 1:1500 FluoVolt do not increase their fractional shortening with increased frequency ($P>0.05$). (**d**) Cells loaded with 1:6000 FluoVolt display a clear positive staircase, effectively identical to controls. Fractional shortening is expressed as *extent* of shortening at each beat. (e.g. 15% fract. short. means the cell is 85% as long during systole as it is at rest.)

The staircase effect in rabbit (LV) isolated cardiomyocytes. Fractional shortening increases in cells paced sequentially at 1 Hz, 2 Hz, and 3 Hz. Fractional shortening significantly increases from 12.8 % to 18.4 % (1 Hz to 2 Hz) ($P<0.001$). There was no significant change in shortening from 2 Hz to 3 Hz.

Cells loaded with 6 µM di-4-ANEPPS also displayed a positive staircase, similarly to controls. Cell shortening increased from 9.4 % to 12.8 % (1 Hz to 2 Hz) ($P=0.002$). No change in fractional shortening was observed between 2 Hz and 3 Hz.

Cells loaded with 1:1500 FluoVolt did not exhibit a staircase effect, indicating cellular damage and disruption of physiology. There was no change in fractional shortening at any frequency ($P>0.05$). Interestingly, some of the cells displayed decreased contraction amplitudes with increased stimulation frequency (2Hz to 3Hz).

Cells loaded with 1:6000 FluoVolt displayed a preserved staircase effect, with a significant shortening increase from 12.7% to 16.9% (1 Hz to 2 Hz) ($P<0.001$). Once again there was no significant difference between 2 Hz and 3 Hz.

3.5.8 Removal of motion artefact using blebbistatin

Using fluorescent probes to record membrane potential relies on collection of light at a specific wavelength from the field of view. However, the transient changes in fluorescence observed may not always be a factor of the observed variable (e.g. V_m, Ca^{2+}). This is particularly important for optically mapping the heart using single wavelength dyes, as motion artefact is one of the most prominent issues encountered in accurately measuring fluorescence changes on the surface. Fluorescent tissue moves in and out of the field of view as the heart contracts and relaxes, causing fluctuations in fluorescence which are independent of voltage changes in the tissue. To remedy this, E-C uncouplers have been extensively used in whole heart experiments to inhibit the contractile proteins responsible for contraction, without significantly affecting electrical activity in the tissue.

The mechanical uncoupler blebbistatin was chosen for these sets of experiments. It inhibits myosin II ATPase and prevents actin-myosin motility, thereby inhibiting contraction (Kovács *et al.*, 2004). Having been used in rabbit and rat, (Farman et al., 2008; Fedorov et al., 2007). it has also been demonstrated, unlike other uncouplers such as BDM to have minimal effects on ECG parameters and atrial or ventricular electrophysiology. While it was deemed innocuous enough at the concentrations and for the purposes of this work, it is worth noting recent research shows potential APD prolongating properties of blebbistatin in whole heart experiments (Brack et al, 2013). These findings used 5 µM Blebbistatin for 60 min in whole hearts, while single cell work in this thesis used 3 µM for 20 min.

Motion artefact in the form of a positive deflection in phase 2 and 3 was identified in almost all cells loaded with FluoVolt (1:6000). Incubation with 3 µM blebbistatin reduced the amplitude of the artefact but did not completely eliminate it (see Figure 3.11).

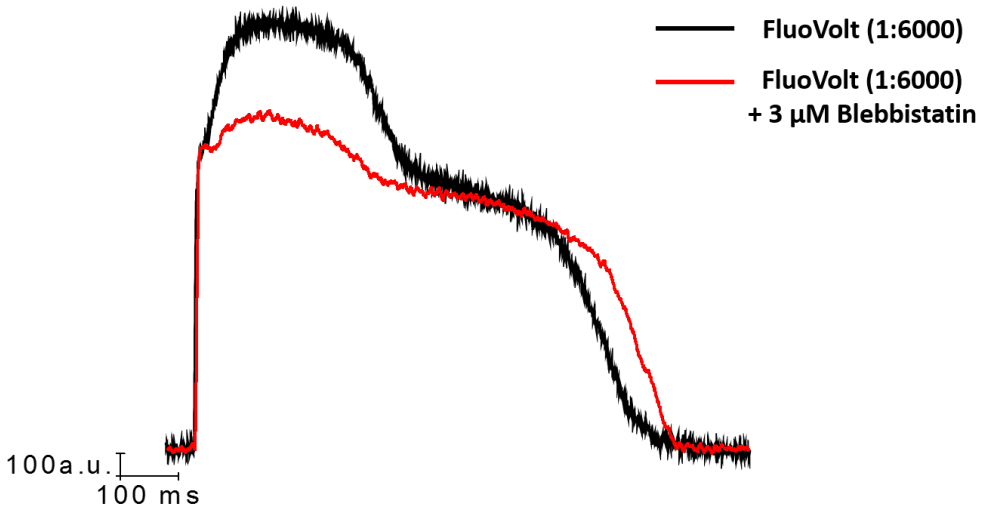

Figure 3.11 Motion artefact reduction with blebbistatin. Example trace of fluorescent AP recorded in the same cell before and after blebbistatin incubation. The “bump” artefact observed in the baseline recording (black) is reduced with blebbistatin, but still prominent. Furthermore, the was evidence of moderate APD prolongation in cells treated with blebbistatin, however motion artefact prevented reliable quantification of this.

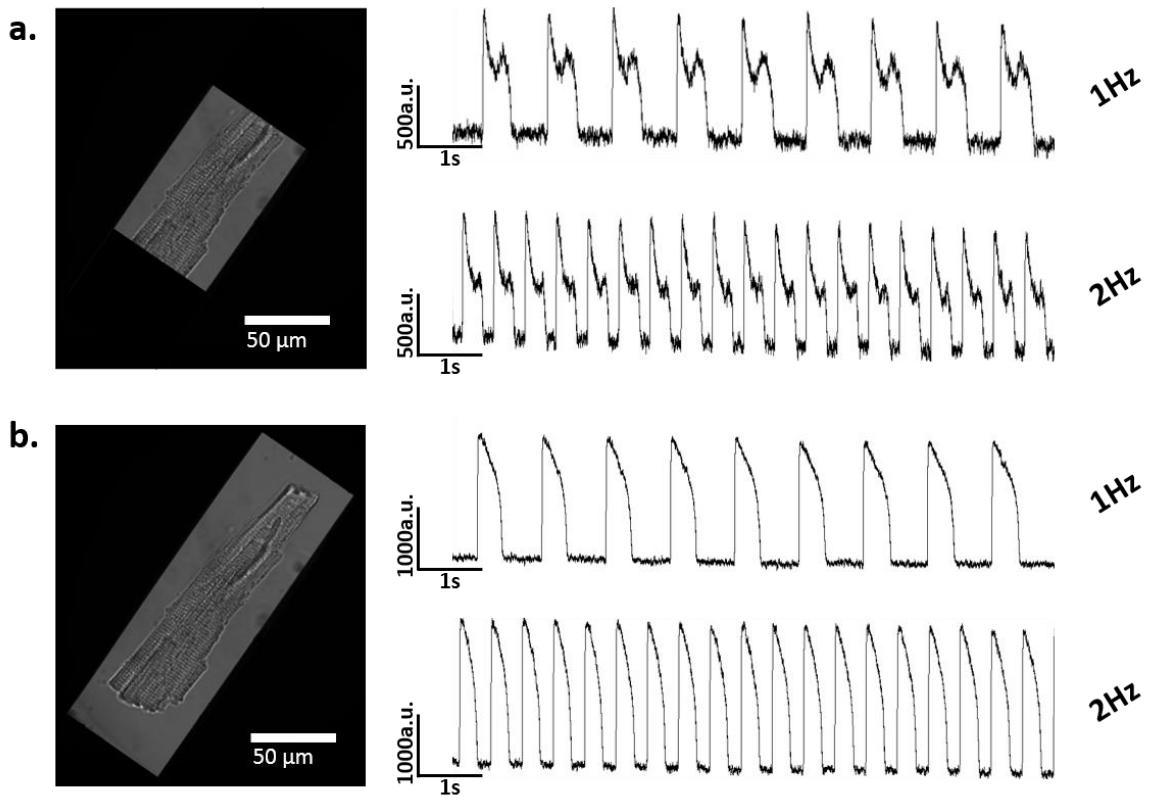

Figure 3.12 Exaggerated motion artefact with improper iris placement. Effect of rectangular iris placement on single wavelength fluorescent recordings in the same cell. (a) Incorrect iris placement. Part of the beating cell is coming in and out of the FOV, which creates fluctuation in fluorescence associated with the surface of the cell exposed to the light - sensing equipment (PMT) rather than a change in membrane voltage. (b) Correct iris placement. The whole cell is visible during contraction, entirely removing the artefact.

It is worth noting the contraction and motion themselves are not a factor in artefact creation, if the illumination power is constant across the sampling area. Unlike whole-heart imaging, where illumination across a field of several cm will almost inevitably be non-homogeneous, fluorescent recordings in single cells across a few hundred µm is unaffected by this, and was consequently not an issue in this thesis. The proper shutter placement, indicated in Figure 3.12(b) was used throughout this thesis.

3.6 Discussion

3.6.1 Post-isolation cell viability

Ion current run-down is a known phenomenon in patch clamping, whereby the calcium current of the patched cell decreases over time, caused by a rise in intracellular calcium and a loss of high-energy compounds such as ATP (Belles *et al.*, 1988). The rate of decay varies depending on the technique; in whole cell patch, the seal can be maintained for short periods, but if the seal fails or tears through the cell membrane, the cell cytosol comes in direct contact with the outside, and the cell dies. With on-cell patching (intact membrane), single cell experiments can last substantially longer. Using fluorescent techniques, the experimental throughput gradually increased with each iteration of the recording protocol, and experiment duration followed suit. Experiments initially lasted approximately ~1 hour, yielding ~5-20 cells. After optimising our protocol, provided the cell isolation yielded a reasonably high live:dead cell ratio, experiments then lasted for to 4-8 hours after isolation. While this was a positive development, cells still eventually deteriorated over time after enzymatic isolation. Counter-intuitively, keeping cells incubating at 37°C and 5% CO_2 prior to experiment dramatically reduced the survival rate. Cells kept in Ca^{2+}-free Krebs solution at room temperature survived longest and did not show signs of deterioration in terms of membrane blebbing and inexcitability (see Figure 3.6). Batches of cells were therefore kept at ~0 mM Ca^{2+} until immediately prior to recording.

The potential risk of using cells to record physiological parameters several hours after being removed from the heart was investigated by plotting the AP duration as a function of time, using recordings from a sample of 18 experiments, acquired over a span of 24 months. There was no evidence of APD drift, up to 8 hours post-isolation.

3.6.2 Plate design and temperature regulation

Unlike commercially available stage incubator systems, our system enabled access to a higher aperture objective, previously hindered by its narrow working distance (WD=0.18 mm), by machining a wide enough opening on the bottom of the plate, and adjusting the plate temperature to account for the resulting heat loss.

While light collection efficiency could have been further improved, by further increasing aperture >1.0 by using a water or an oil-immersed lens, this would have likely caused a localized heatsink effect, requiring more complex, less efficient methods for regulating

temperature such as objective heat-sleeve or microscope enclosure. Furthermore, this would have added another variable to the system, requiring optical calibration with temperature changes.

Signal-to-noise ratio of FluoVolt

Manufacturer recommended concentrations for FluoVolt were determined unsuitable for isolated CM study. At recommended concentrations, FluoVolt caused cell damage and was found to negatively affect the staircase effect in isolated CMs. Reducing the concentration used to ~1/6th resulted in a higher signal-to-noise ratio than previously used dyes, and did not affect cell survival, AP duration, or contraction kinetics. Furthermore, using FluoVolt caused a net reduction in potential photo-damage, by permitting a reduction in excitation light power due to its increased brightness, combined with increased light collection efficiency.

3.6.3 Motion artefact reduction

Using FluoVolt for measurement of membrane potential caused an artefact in the early to late plateau phases of the action potential (phase 2 and 3), originally thought to be caused by movement of the cell *within* the FOV. this artefact was found to be caused by a portion of the cell membrane moving *in and out* of the FOV. Through systematic placement, this artefact was removed entirely, and did not require the use of a myosin inhibitor, by standardising the placement of a rectangular iris in the optical path (Figure 2.2) such that the whole recorded cell was visible during its entire contraction cycle (see Figure 3.12).

Chapter 4: Signal processing and deconvolution

4.1 Background

4.1.1 Fluorophores

Using fluorescent molecules to study biological mechanisms harnesses the process of raising the energy state of a molecule using light of wavelength λ_1 and recording the emitted light of a wavelength λ_2 originating from the fluorophore as it returns to its original energy state, where $\lambda_1 < \lambda_2$ The energy of the emitted photons (λ_2) from the fluorophore must be less than that of the excitation light used (λ_1), as some energy is inevitably absorbed by the fluorophore itself to undergo conformational change. This is known as the Stokes shift (Ronzhina and Cmiel, 2012). Exposing the sample to light of a specific wavelength can be achieved through various methods including a xenon/mercury arc lamp, halogen lamp, light emitting diodes (LED), or lasers (Efimov, Nikolski and Salama, 2004; Fast, 2005). It is worth noting this process is not perfect, as many factors affect the efficiency of light re-emission by a fluorophore. Each fluorophore has a specific quantum efficiency (Φ), defined as a ratio of emitted light divided by absorbed light. The wavelengths used for excitation will affect the quantum efficiency, for example lower energy (red) light can penetrate deeper into tissue without being absorbed, forming the basis for 2-photon microscopy. Resonant energy transfer also affects the emission efficiency, by either causing an adjacent molecule to emit light (FRET), or absorb it. Fluorophore bleaching is particularly problematic and often requires post processing, such as the fitting and subtraction of a linear or exponential decay curve to the recorded fluorescent trace, to correct for it.

4.2 Section Aims

Explore the limitations of the optimised optical system (Chapter 3) and develop a protocol for deconvolving wavelength emissions from spectrally overlapping fluorescent dyes.

4.2.1 Limitations of fluorescent measurements

Fluorescent measurements, like other indirect measurements of biological events, have limitations. The most basic of these is the correlative factor of fluorescent change to change in the variable of interest. If fluorescence emitted by a fluorophore is a function of something other than the variable - e.g. pH, temperature, background fluorescence - the accuracy and relevance of the measurement decreases, and must be accounted for. This creates a strong incentive to choose fluorophores reasonably specific to a singular variable. Secondly, fluorophore resistance to bleaching must be optimised or else accounted for, for the duration

of the measurement. Thirdly, the type of fluorophore used, either single (non-ratiometric) or dual wavelength (ratiometric), should be selected where appropriate, because single-wavelength dyes emit light as a function not only of the concentration of fluorophore present in the sample, but also of the light intensity used for excitation, and length of the optical pathway (Fukano, Shimozono and Miyawaki, 2008). Ratiometric dyes (Fura-2, Indo-1) overcome this problem by shifting either excitation or emission spectra as a function of substrate availability. Light sampled from two different wavelength bands allows the ratio of these signals to determine the absolute concentration of substrate in the sample at a given time. Lastly, a common issue arising when using multiple fluorophores in the same sample is light contamination and generation of mixed wavelength light from two or more fluorescent molecules, either native to the sample (notably background fluorescence) or artificially inserted via other fluorophores.

4.2.2 Noise and sampling rate

Detecting sufficient amounts of fluorescence in response to small changes in substrate without interfering with physiology is paramount to quantifying substrate changes accurately. Dye response must also be reasonably fast to resolve events in the millisecond range. To measure voltage changes in isolated cells in our experiments, the new voltage-sensitive dye FluoVolt was used. FluoVolt is a single wavelength dye, reportedly displaying 25% fluorescence increase per 100mV increase, with a sub-millisecond response time (Thermo Fisher).

Fast dye response combined with high sampling rate constitutes increased temporal resolution. We measured voltage at a rate of 10 kHz, or one measurement every tenth of a millisecond. Although the theoretical ceiling of our temporal resolution was therefore 0.1 ms, trace filtering reduced this, as discussed later.

Calcium measurements made using Fura-4F were sampled at 500 Hz. This 20-fold reduction in sampling rate does not affect the reliability of calcium measurements as the fastest events we recorded ranged in the 10-20 ms range.

4.2.3 Upstroke temporal resolution

Fast events such as the upstroke of the action potential are difficult to resolve temporally. The sampling rate of 10 kHz provided 0.1 ms resolution as discussed previously, however due to the noise present in any fluorescent traces, adjacent filtering was applied to recordings for analysis. A standard 3-point boxcar filter applied 15 times was consistently applied, meaning the fastest fluorescent change observable using these settings was 1.5 ms (Figure 4.1). The advantage of 15 passes of a 3-point average over a single pass 15-point average was better fit of the inflection points of the upstroke.

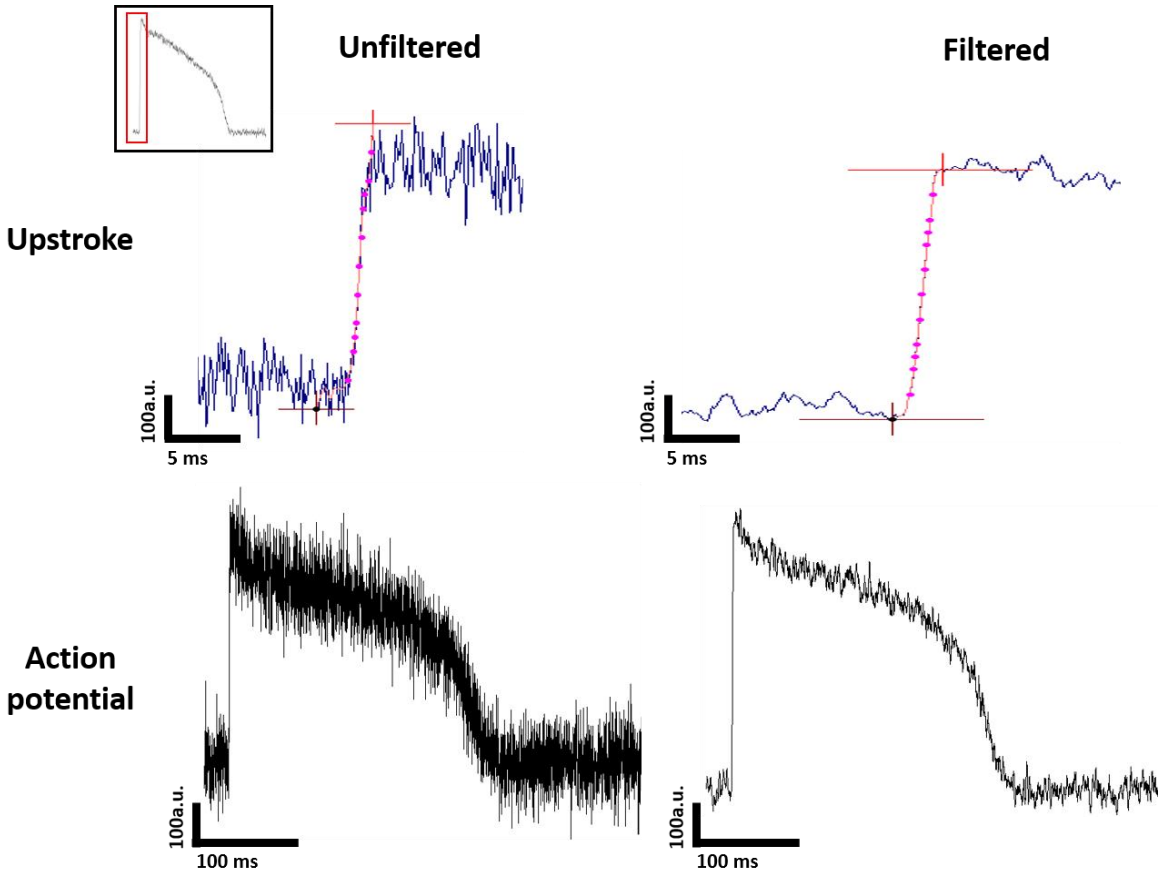

Figure 4.1 Signal noise and upstroke resolution. Example of an action potential upstroke. An unfiltered trace (left) and a filtered trace (15-pass 3-point averaging, right). The signal noise impairs the accuracy of baseline and peak detection. Consequently, this filtering level was used for consistency in results, chosen as an optimal point between fast sampling and accurate baseline and peak detection.

Filtering smoothes the trace and reduces the noise at baseline and peak of the upstroke, but also causes the slope to slant forward, and thus become artificially prolonged. Conversely, minimal or no filtering of the trace conserves high temporal resolution but makes the detection of the baseline and maximum peak of the upstroke equally difficult to assess. A

"sweet spot" filtering was selected for consistency with typical experimental SNR, without negatively impacting measurements.

Detecting and quantifying events in the millisecond range requires high signal-to-noise and sampling rates. The upstroke of action potentials in typical cells is in the order of 0.5-1.5 ms (Berecki *et al.*, 2010). Our theoretical maximal resolution was 0.1 ms, allowing at best 5 to 30 points to be recorded during an average upstroke. While this is theoretically possible, smoothing was applied to accurately determine the start and end of the upstroke, and the impact on other measurements such as repolarisation duration (APD_{90}) was assessed (Figure 4.4).

4.2.4 Signal deconvolution

The excitation spectrum of Fura-4F and FluoVolt overlap in the 380 nm range (See Methods). Exciting Fura-4F using 380 nm wavelength light consequently also excited FluoVolt, albeit less efficiently than the dedicated 470 nm wavelength. The resulting calcium transient recordings consequently consisted of a combination of both emissions, which required spectral deconvolution to extract one from the other. To achieve this, the relative effect of each excitation light used was plotted against the corresponding FluoVolt response (Figure 4.7). In turn, this allowed a corrective factor to be applied to the traces to remove the stray voltage signal from the calcium signal, as shown below.

$$Corrected\ Fura\ 4F\ ratio = \frac{340nm\ signal - (470nm\ signal\ \times\ corr\ factor - constant)}{380nm\ signal - (470nm\ signal\ \times\ corr\ factor - constant)}$$

The "correction factor" and "constant" above respectively describe the slope and y-intercept of the linear relationship between FluoVolt signal at different excitation wavelengths determined in Figure 4.7.

4.3 Methods

4.3.1 Fluorescent noise and upstroke measurement error

A group of cells from the same animal was loaded with FluoVolt as previously described in Chapter 2. The resulting action potential traces recorded were analysed twice, using adjacent averaging, or no filtering at all. The resulting upstroke times were plotted to assess the impact of filtering on the measurement reliability of fast events.

Additionally, square wave traces simulating action potentials trains with <100 µs upstrokes were generated artificially. A range of Gaussian noise typically encountered experimentally (σ = 300 - 1000) was added to the traces and they were analysed identically to experimentally generated APs. The traces were analysed once without any trace processing and once with our optimised adjacent averaging.

4.3.2 Fluorescent noise and APD measurement error

Identically to 1.2.1, the APD_{90} values recorded from the same group of cells were analysed with and without filtering, and the resulting APD values were compared graphically.

4.3.3 Quantifying FluoVolt vs. Fura-4F cross-excitation

Isolated CMs were loaded with FluoVolt as described previously, and incubated at 37°C. The cells were not electrically paced, and consequently only the baseline fluorescence was recorded for each cell. Individual cells (n=25) were exposed to 470 nm light for 2.5s, simulating a voltage recording, and immediately thereafter exposed to the 340nm/380nm alternating wavelength excitation, simulating a calcium recording. The fluorescence detected after each excitation protocol in the same cell permitted the direct comparison of the fluorophore response (signal intensity) of FluoVolt to 470 nm, 340 nm, and 380 nm excitation, respectively. A linear regression was plotted to quantify this effect and to calculate a correction factor for trace deconvolution.

To successfully deconvolve the stray FluoVolt fluorescence from the Fura-4F emission in real time, a triple-excitation protocol was implemented (Figure 4.2).

4.3.4 Fluorophore triple excitation protocol

Excitation of FluoVolt and Fura-4F nearly simultaneously requires rapid, successive turning on and off of the excitation LEDs. Similarly to the ratiometric method used with Fura-4F, an extra step was added to the excitation protocol.

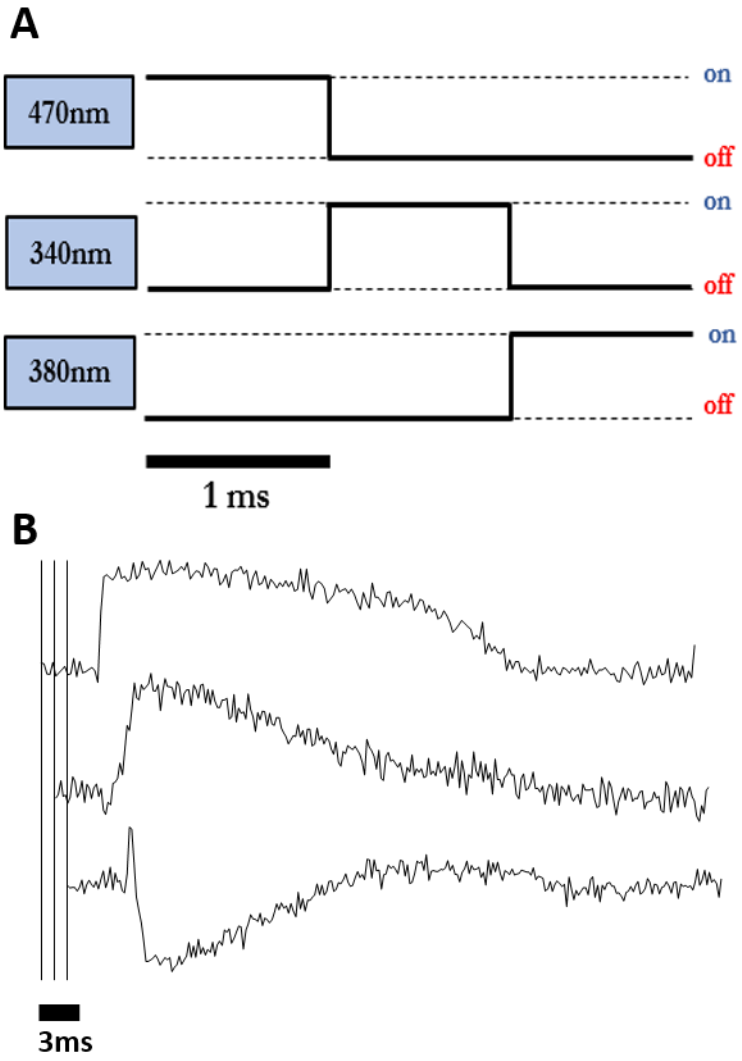

Figure 4.2 Triple excitation protocol. (**A**) Diagram of new excitation protocol for near-simultaneous excitation of FluoVolt and Fura-4F. First the 470nm LED is switched on for 1 ms, followed by the 340nm LED for 1 ms, and finally the 380nm LED for 1 ms. This is repeated for the entire duration of the recording, and consequently allows a sampling rate of 333.3 Hz for voltage and calcium. The recording examples (**B**) are offset by 1 ms from one another.

4.3.5 Semi-automated signal deconvolution using Python 3

The fluorescent transients generated from the triple wavelength excitation protocol were saved to three *.csv* files for subsequent deconvolution using Python program (written by

Quentin Lachaud) using the Spyder integrated development environment (IDE). The files were sequentially opened, and the correction factor was applied where appropriate to each trace. Corrected ratio (340 nm/380 nm) traces were saved to a separate folder and converted to *.mda* (native CellOPTIQ) format, which could then be imported into the CellOPTIQ platform, identically to all other recorded traces (See Appendix).

4.3.6 Impact of fluorescent noise on CellOPTIQ measurement accuracy

Measuring action potential characteristics such as repolarisation duration and upstroke time consistently between cells and experiments relies on a standardised method of trace analysis. This analysis was integrated within CellOPTIQ and specific parameters such as noise filtering must be constant across experiments to ensure comparability between datasets. Due to the variable nature of fluorescent signal noise recorded from dye-loaded cells, the precision with which key voltage characteristics were measured also varied. This was quantified by using a modelled train of action potentials from the Dempster model (Dempster, 2016), onto which gaussian noise representative of experimental conditions was added (Figure 4.5). Artificial trains of five action potentials at 3 frequencies were generated and analysed using standard CellOPTIQ protocol and compared to the modelled noiseless trace.

4.4 Results

4.4.1 TRise and trace filtering

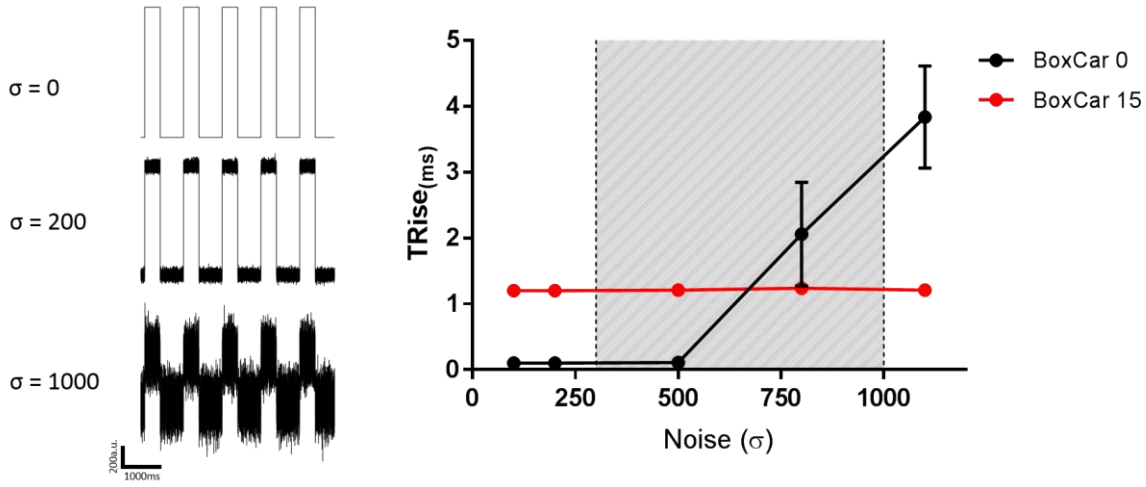

Figure 4.3 Effect of systematic filtering on upstroke resolution. Example of artificial AP trains (N = 10, respectively) with very fast upstroke speed (TRise < 0.1 ms) analysed with a range of gaussian noise artificially applied to the trace. Filtering the trace (Boxcar filtering, 15 pts) artificially prolonged TRise by 1 ms irrespective of initial noise level. Unfiltered traces show increased TRise measurement at noise of 750 S.D. and above. Typical experimental noise S.D. ranges from 300 to 1000 (arbitrary units).

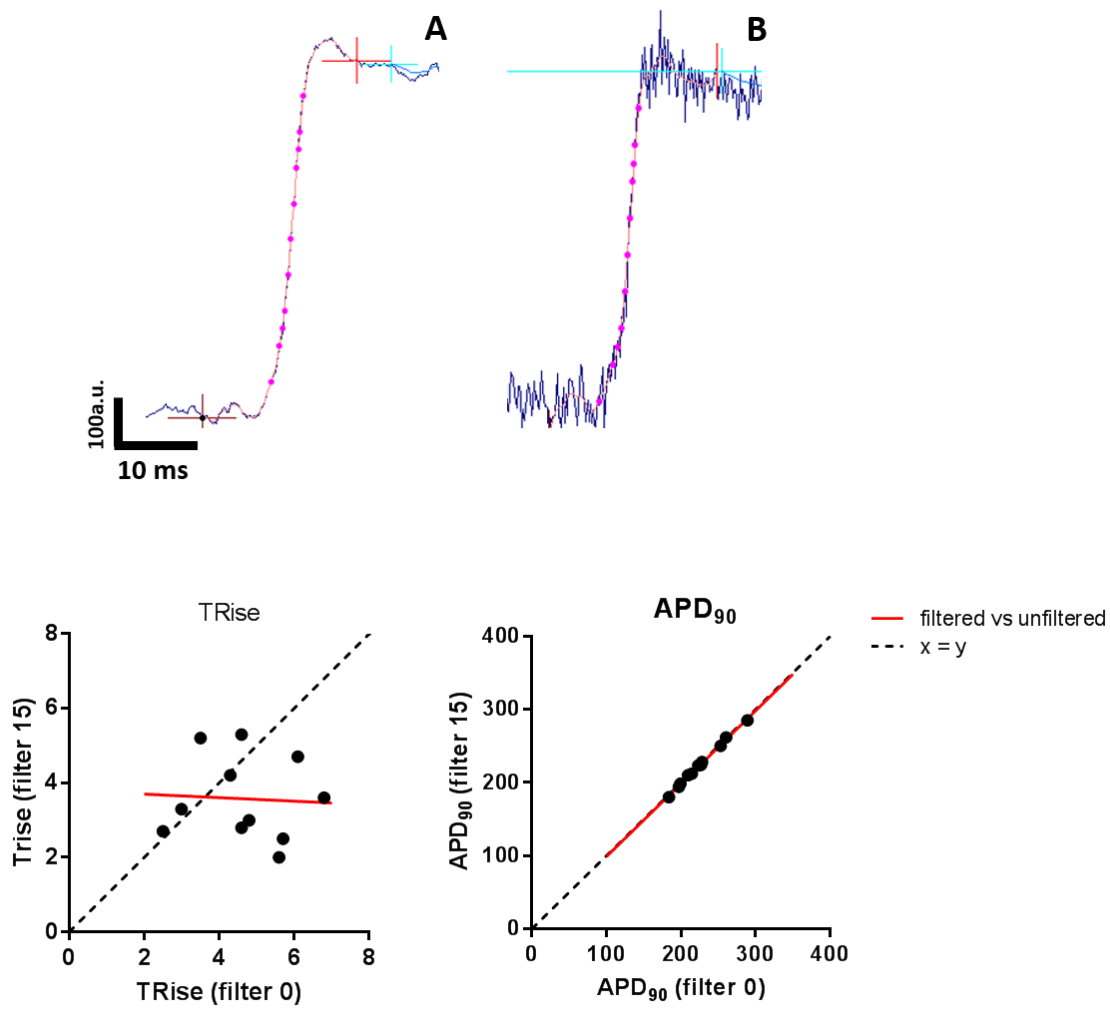

Figure 4.4 Impact of trace filtering on upstroke and repolarisation. Example AP upstroke with smoothing applied (A) and without (B) Pink dots denote % depolarisation from total upstroke amplitude (10-100%). A best fit spline was applied to each trace to determine percentage depolarisation. TRise was calculated as $Upstroke_{90\%}$ – $Upstroke_{10\%}$. Scatter plots of TRise and APD_{90} values derived from the same group of cells. TRise is heavily affected by filtering (see Figure 4.3), while APD_{90} is not. (dotted line for reference; x = y)

Figure 4.4 above shows that applying standard filtering to traces impacts the measurement of action potential upstroke but not APD_{90}. The lack of correlation before and after filtering seen in TRise underlines the difficulty of measuring such a fast event. With minimal or no filtering, the signal noise makes it challenging to detect the beginning and end of depolarisation. With excessive filtering, the beginning and end of depolarisation are straightforward to detect, but the trace becomes artificially slanted due to adjacent averaging. A 15-pass, 3-point filter was determined optimal and applied throughout.

4.4.2 Measuring AP duration with variable noise

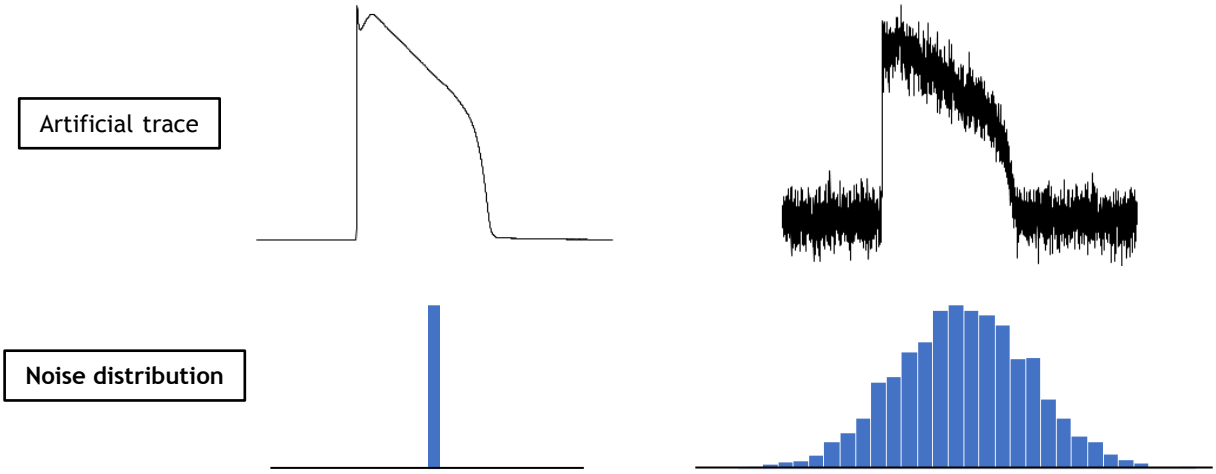

Figure 4.5 Example of simulated artificial fluorescent trace. (left) Simulated action potential (Dempster, 2016) with no added noise and (right) with added gaussian noise using the mean σ encountered experimentally (n = 10).

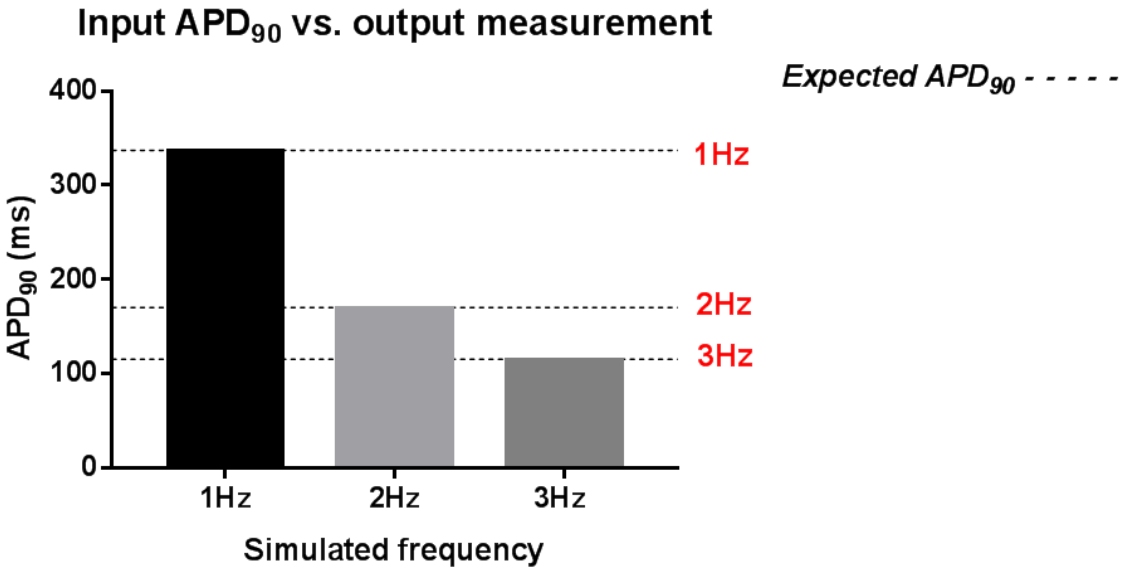

Figure 4.6 Testing CellOPTIQ accuracy. Bar chart comparison of measured AP durations (σ = 300) with theoretical values (dotted lines). Mean and S.D. were plotted but error bars were too small to display (expected values for APD_{90} represent the known duration of artificial APs, before applying signal noise).

Figure 4.6 shows measuring APD_{90} in dye-loaded cells proved highly reliable experimentally, as was not affected significantly by trace filtering. Furthermore, APD_{90}

measurement was very accurate and consistent at a set noise level in artificial action potentials (Figure 4.6). Unlike TRise, typical APD_{90} values can range from 80-800 ms, and therefore are not significantly affected by trace filtering. Nonetheless, standard boxcar (15-pass 3-point) filtering was applied to all traces to standardise analysis.

4.4.3 Trace deconvolution corrective factor calculation

In order to remove stray FluoVolt fluorescence from calcium traces recorded in cells loaded with both Fura-4F and FluoVolt, the relative excitation of FluoVolt using 340nm and 380nm wavelengths was compared to the 470nm LED (used to excite FluoVolt). The percentage excitation achieved relative to the 470nm LED was recorded (see Figure 4.7) and applied in the deconvolution process (see 4.2.4).

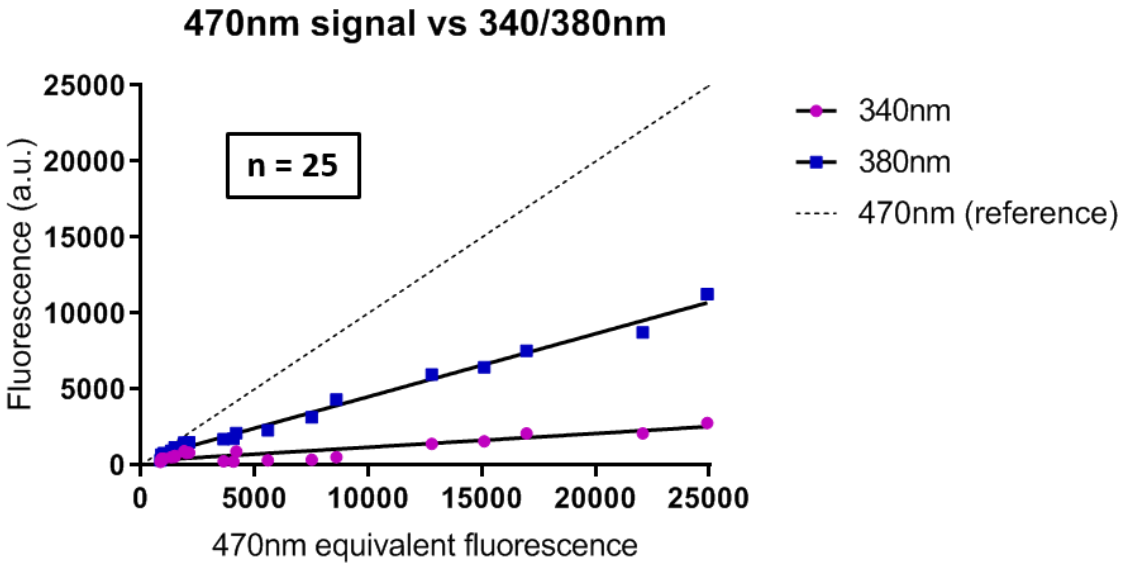

	340 nm	380 nm
Slope gradient	0.09	0.41
Y-intercept	278	354
R^2	0.87	0.98

Figure 4.7 Relative excitation of FluoVolt using Fura-4F excitation wavelengths. Linear regression of FluoVolt excitation using 340nm (purple) and 380nm (blue) LEDs plotted against 470nm excitation (x = y; dotted line). 340nm and 380nm light excites FluoVolt with 9% and 41% efficiency, respectively.

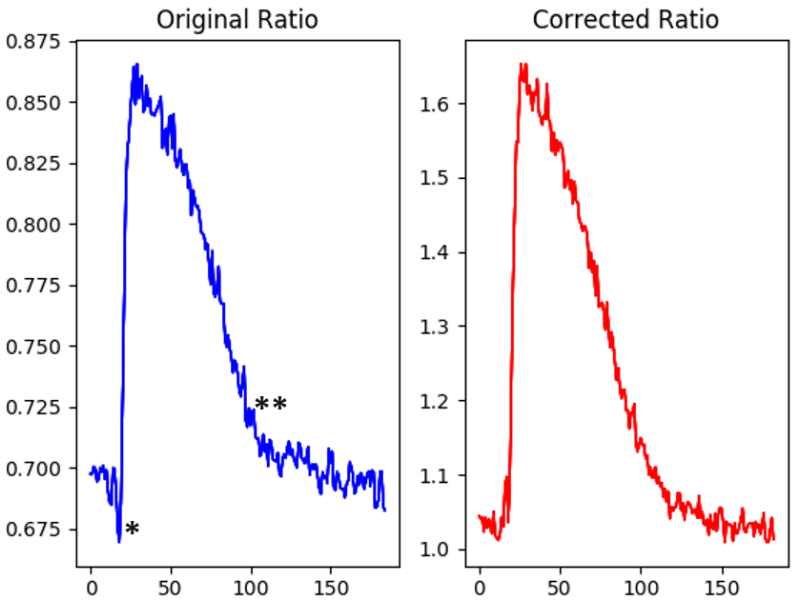

Figure 4.8 Example of Fura-4F signal deconvolution. Example 340nm/380nm ratio trace prior to, and after deconvolution. The negative deflection prior to upstroke (*) and sharp inflection (**), an artefact from AP repolarisation, are diminished after removing the scaled FluoVolt fluorescence from each channel. Note the change in Y-axis scale used.

Figure 4.8 shows the subtle effect of deconvolution on the calcium transient kinetics, removing the negative deflection (*) caused by the action potential upstroke and the abnormally sharp inflection in the decay phase (**). More strikingly, the baseline and amplitude (diastolic and systolic calcium) were increased after deconvolution. This effect was quantified in Figure 4.9.

The Ca^{2+} baseline and peak were both affected by light-contamination (i.e. signal originating from FluoVolt caused by 340/380nm excitation), and subtraction of this stray signal allowed for quantification of absolute concentrations of Ca^{2+} in the cell. For example, 340nm excitation of Fura-4F displays a decrease in fluorescence at the 510nm wavelength when $[Ca^{2+}]$ increases inside the cell. This coincides temporally with an increase in fluorescence from FluoVolt, during the action potential upstroke, creating a compound fluorescence signal.

4.4.4 Effect of deconvolution on calcium metrics

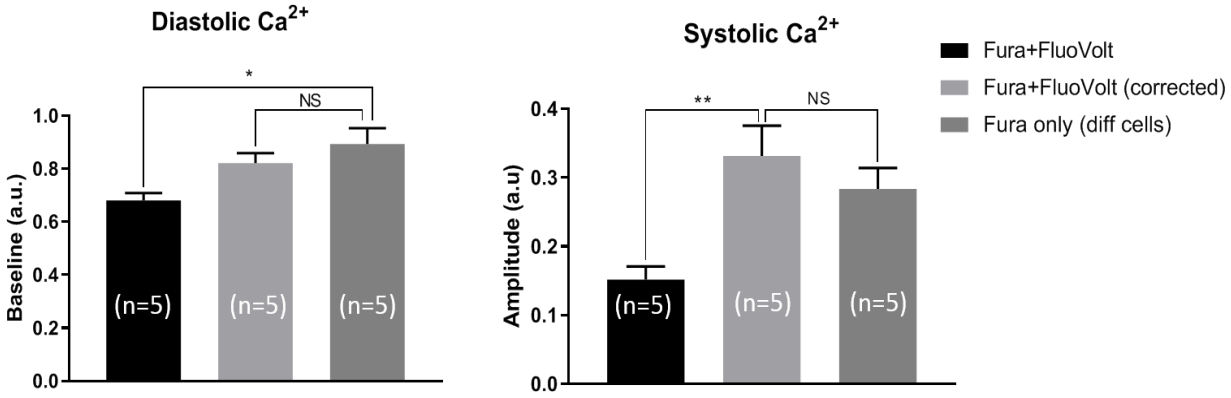

Figure 4.9 Effect of deconvolution on calcium parameters. Comparison of baseline (left) and amplitude (right) of calcium transients before deconvolution and after deconvolution. Both baseline and amplitude are significantly different from control cells (loaded with Fura-4F alone) before deconvolution ($P<0.01$ and $P<0.05$, respectively. Paired t-test). The corrected baselines and amplitudes do not show significant difference from control (Fura-4F-only) cells ($P>0.05$). All cells originated from a single heart (N = 1).

Without the deconvolution step, using the 340nm/380nm excitation protocol would result in both Fura-4F and FluoVolt being excited and emitting in the same wavelength-range. This means the recorded fluorescence would be both a measure of the intracellular calcium within the cell, as well as the membrane potential. After deconvolving the traces, fluorescence analysis allows ratiometric measurements to be made: in other words, it achieves a measure of absolute calcium concentration, free of contamination from other known fluorescent sources. Before deconvolution, both baseline fluorescence (diastolic Ca^{2+}) and peak fluorescence (systolic Ca^{2+}) are significantly different in dual loaded cells from controls loaded with Fura-4F only ($P>0.01$ and $P>0.05$, respectively.). After deconvolution, baseline and peak fluorescence values are no longer statistically different from controls ($P>0.05$).

4.5 Discussion

4.5.1 Action potential upstroke resolution

Measuring the upstroke duration of action potentials using fluorescent signals presents the logistical challenge of finding the optimal signal-to-noise (i.e. Maximizing SNR while avoiding toxic dye concentrations) combined with high signal-sampling rates. Comparing T_{Rise} measurements in "perfect"/noise-free, action-potential-like waveforms demonstrates the limitations of the methodology in quantifying the duration of events in this range. Using patch clamping to measure V_m directly benefits from high sampling rates (~50kHz) as well as very low noise. While indirectly measuring V_m using fluorescence substantially increases experimental throughput, the technique suffers from considerably higher noise. This noise varies from cell to cell and between experiments, as cell size and membrane health may affect how much dye is present in each cell. Assuming membrane turnover is standard from cell-to-cell, variability in cell loading is unlikely to affect experimental SNR. Figure 4.3 shows that a boxcar averaging (15 pass; 3 points) was optimal to measure T_{Rise} consistently, irrespective of noise levels. While the measure of upstroke time is improved following filtering, the absolute duration (0.1-1.5 ms) has been irreversibly and artificially prolonged. Consequently, measures of upstroke time using this method are more relevant to paired experiments comparing a baseline with a transient effect (i.e. drug), rather than reported as absolute values, given the limited resolution of the measurements.

4.5.2 Action potential repolarisation measurement accuracy

In contrast to fast events like AP upstrokes, repolarisation occurs over hundreds of milliseconds and is not nearly as sensitive to trace filtering as T_{Rise}. The systematic filtering applied to traces (boxcar 15) did not affect any measure of repolarisation kinetics such as APD_{90}. Repolarisation kinetics measurement using CellOPTIQ was found to be highly reliable (see Figure 4.6), and not affected by the typical noise encountered experimentally.

4.5.3 Signal deconvolution

By quantifying the relative fluorescent crosstalk of FluoVolt using excitation LEDs meant for Fura-4F excitation, the relative contamination of both 340nm and 380nm channels was used to subtract the stray voltage signal from calcium recordings made using a triple sampling protocol. The effectiveness of this method was tested on a batch of cells from a single heart and was found to restore the ability of the technique to make ratiometric

measurements in these cells, despite the presence of FluoVolt. A shortcoming of this method was the reduction in sampling rate caused by the triple excitation protocol. As mentioned previously, calcium kinetics in whole cell measurements occur in the 10-400 ms range, which does not necessitate sampling in the kHz range to resolve. Alternatively, rapid voltage kinetics such as T_{Rise} will be affected by the low sampling rate tested (333Hz). A solution to this is to record action potentials at 10 kHz, followed by an accurate ratiometric measurement of calcium at 333Hz. This approach used on cells beating at 2 Hz would mean each cell could yield both a measure of voltage and calcium within 5s, maintaining the throughput of the technique, as well as repeated paired measurements in individual cells, as necessitated in drug studies.

Chapter 5: Electrophysiology of MI cell populations

5.1 Background

5.1.1 Regional electrophysiological differences

Cardiomyocytes originating from different regions of the healthy myocardium can have dramatically different action potential shapes and repolarisation profiles. Ion channel protein expression, membrane trafficking, and pore-opening kinetics underlie the differing electrophysiological properties of cells in distinct cardiac regions.

Different electrophysiological properties have been identified across the ventricular wall *in vitro*. Notably through the description of canine M-cells in the 1990s, a subtype of mid-myocardial cells with long AP durations as well as disproportionate AP prolongation at slow heart rates (Pye and Cobbe, 1996; Antzelevitch, 2007), and in response to APD-prolonging agents (Prenner *et al.*, 2016). They have now been found in many species, including guinea pig, rabbit, pig, and humans (Taggart *et al.*, 2001).

Sub-endocardial and sub-epicardial cells also display marked electrophysiological differences. Most notably, Phase 1 of the action potential differs between endocardium and epicardium. Sub-epicardial cells have a characteristic phase 1, indicative of a pronounced transient outward K^+ current (I_{to}), weaker in sub-endocardial cells (Figure 5.1). They also have different AP durations, as the endocardium is typically reported to repolarise slower than the epicardium, indicating a subtly different interplay of repolarising channel expressions and opening kinetics.

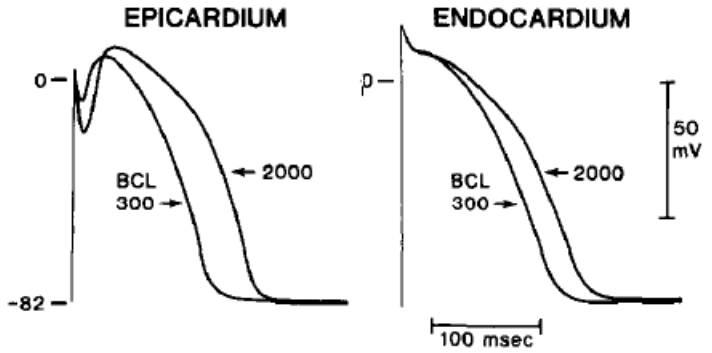

Figure 5.1 Illustrative example of transmural canine action potentials differences. Example of canine epicardial and endocardial action potentials at 300ms and 2000ms cycle lengths, respectively. (Taken from Litovsky & Antzelevitch 1989).The search for transmural repolarisation gradients is not new. Taggart et al., (2001) investigated repolarisation

patterns in the normoxic and hypoxic human heart, and did not find evidence of repolarisation gradients across the ventricular wall at physiological (<200bpm) or bradycardic heart rates (~40bpm). They propose that the presence of cell coupling and electrotonic current flow could mask repolarisation differences between individual cells and regions. The absence of gradients from their experiments could also be explained in part by the degree of pathology present in these experiments. It is possible that ischemia-induced, pro-arrhythmic electrophysiological states (i.e. transmural gradients) only develop acutely and immediately preceding arrhythmic events, prior to which their presence could be masked by cell-cell coupling and to an extent, buffered by the repolarisation reserve in whole hearts. Conversely, other groups have reported transmural repolarisation gradients in ventricular wedge preparations and *in vivo*, although at non-physiological, long cycle lengths (Antzelevitch *et al.*, 1999).

The different AP characteristics encountered throughout the heart actively contribute to normal E-C coupling in health, and are subject to disruptive stimuli in pathology. Cellular death resulting from ischaemic damage (MI) to the heart muscle can slow or prevent signal propagation across cardiac tissue, increasing the probability of re-entry and disrupting cardiac rhythm. Depending on the size of the infarct zone, long-term effects of cellular death can result in tissue remodelling, subtly altering repolarisation uniformity between layers and regions of the ventricle.

5.1.2 Cellular pathophysiology of MI-induced heart failure

Heart failure (HF) is broadly defined as a complex syndrome of physiological responses to the heart's inability to maintain an output sufficient to meet the needs of the organism. The effect of HF on cardiac function has been extensively studied over the past decades. A description of the pathophysiology of HF is beyond the scope of this thesis, so only select aspects of remodelling relevant to this work will be discussed.

Heart failure as a result of remodelling following MI is a major cause of sudden cardiac death (SCD), but the electrophysiological mechanisms underlying it are not clear. In general terms, remodelling-induced HF causes cell hypertrophy, AP prolongation, decreased Ca^{2+} handling, resulting in weaker muscle contraction and depressed cardiac output (Pogwizd *et al.*, 2001). The physical adaptions of the failing heart are manifold, and their manifestation highly variable from individual to individual. As this thesis aims to demonstrate, not only

baseline states can vary between animals but also the remodelling following injury which was explain the broadness of HF-associated effects.

After injury caused by acute or chronic ischaemia, structural and functional changes start to occur. Cellular hypertrophy is one of the key markers of HF, where individual CMs increase in length and width (McIntosh, Cobbe and Smith, 2000), with reports of ~60% lengthening in dilated cardiomyopathy (Beltrami *et al.*, 1995). Hypertrophy is also evident at the organ level, with increases in heart size by 20-30%. Left ventricular hypertrophy on its own can occur through cardiovascular training in athletes, but in the case of pathophysiologically compensated hypertrophy, this adaptation initially aids in maintaining cardiac output following decreased function in the ventricle through cellular loss and impaired Ca^{2+} handling. In severe cases, hypertrophy alone is no longer sufficient, and cardiac output continues to decrease as the heart further dilates. This is referred to as decompensated ventricular hypertrophy, which can further progress to HF.

The physiological mechanisms supporting these adaptations are also complex and multi-faceted. Chronic remodelling following ischemia has been shown to affect Ca^{2+} handling as well as gene and protein expression. For example, a reduction in the number of L-Type Ca^{2+} channels has been reported, with little to no change in $I_{Ca\text{-}L}$ (current), indicating an upregulation of individual channel function (Glukhov *et al.*, 2010). The importance of remodelling in the predisposition to arrhythmia has been outlined in several animals models (Akar and Rosenbaum, 2003; Glukhov *et al.*, 2010).

In this work we investigated the cellular electrophysiological adaptations, using a rabbit model, 8 weeks after ligating a major supply vessel of the LV apex. The degree and severity of remodelling present in the animals used in these experiments is not claimed to represent HF, but it does provide a consistent and comparable stage of compensated LV dysfunction in the mammal heart.

5.1.3 Rabbit model of MI

Several models of disease are current in the study of cardiac pathology. Our study utilised the ligation of the left descending coronary artery (LDA) of the rabbit. The vessel is permanently ligated, and the heart is harvested 8 weeks after ligation. This model provides consistent apical LV infarct formation and early stages of cardiac remodelling, comparable to what is often encountered in human post MI, such as a decreased ejection fraction (see

Figure 5.12), cellular hypertrophy, APD prolongation, and comparable scar formation on the ventricle wall.

5.1.4 Frequency-dependent AP duration and MI model

As heart rate increases, the R-R interval, representing the time between ventricular depolarisations on the ECG trace, becomes proportionately shorter. At the cellular level, faster rates decrease the duration of the action potential across the heart, however this effect is not homogeneous (Litovsky and Antzelevitch, 1989). Due to inherent differences in channel expressions across the cellular subtypes, the AP response to changes in rate across different regions like endocardium and epicardium varies. Data suggests that different expression levels of the transient outward potassium current (I_{to}) between endocardium and epicardium result different degrees of APD shortening following increases in rate (e.g. 0.5 Hz to >3 Hz).

APD prolongation is one of the hallmarks of reported electrophysiological features of heart failure at the cellular level (Wickenden et al., 1998), expressed as prolongation of the QT interval on the ECG trace (Shah et al 2019). The degree of APD prolongation is not uniform across CM subtypes. McIntosh et al. (2000) found that rabbit sub-endocardial cells exhibited markedly longer AP durations than sub-epicardial cells in their controls (sham) animals. Following induced HF, sub-epicardial and mid-myocardial cell AP durations increased, while sub-endocardial cell AP duration decreased. These changes result in the reduction of the endocardium-epicardium APD difference, and reduce left-ventricular heterogeneity (McIntosh, Cobbe and Smith, 2000).

5.1.5 Section Aims

This transmural gradient in AP duration and shape will be investigated at the individual cell level to quantify the heterogeneity of the electrical phenotypes responsible for this average difference between regions, in control and MI hearts.

The data in the literature from which electrophysiological differences were derived comes from many different animals, but from a relatively small number of cells from each animal. Although the average APD differences are reported, the extent of variation across myocyte populations is not known. The hypothesis of this work is that the myocyte electrophysiological phenotype spread contributes to “normal” electrophysiology in healthy hearts, and its alteration could consequently represent a possible explanation for the highly

variable nature of the pro-arrhythmic substrate found *in vivo*. Pharmacological intervention to reverse or inhibit the loss of an electrophysiological phenotype spread could therefore find relevance in the treatment of arrhythmias of the failing and remodelled heart.

The focus of this chapter is to (1) characterise the AP duration of isolated cells populations from the rabbit LV at three different rates, and how these AP durations vary (i) within individual hearts and (ii) between animals (see intra- and inter-animal variation in Figure 5.2). These data were used as a physiological baseline against which cells originating from infarcted hearts (MI model) were compared. (2) To compare intrinsic differences in electrophysiological properties between the inner (sub-endocardial) and outer (sub-epicardial) layers of the left ventricle in control (Sham) and infarcted (MI) tissue.

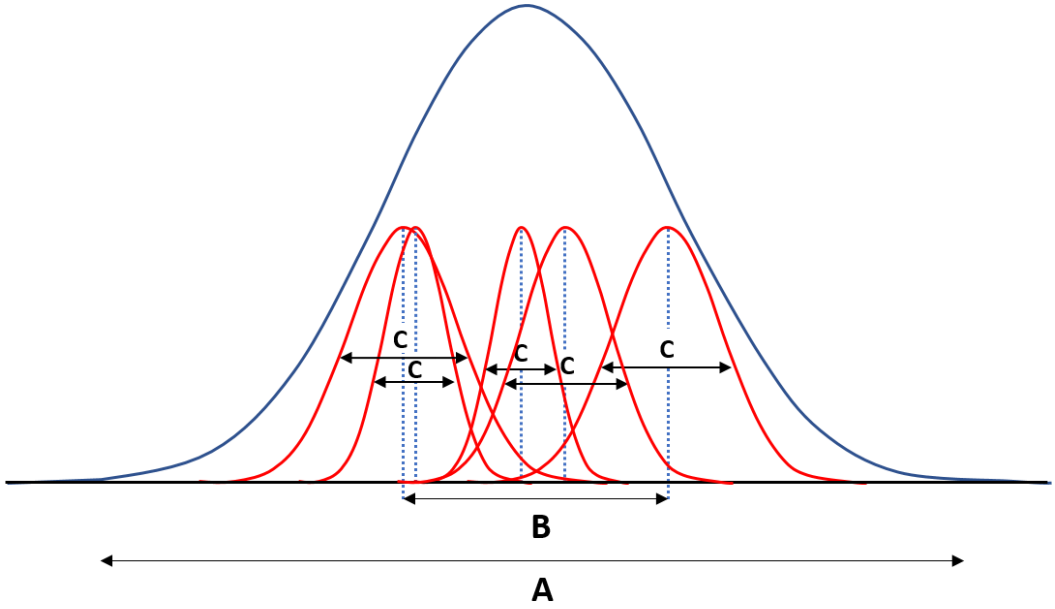

Figure 5.2 Diagrammatic example of hierarchical levels of variation studied A. Compound variation of all cells from every heart sampled. B. Variation between mean APD from each heart. C. Mean variation within each individual heart (requires large cell populations).

5.2 Methods

5.2.1 MI APD response to change in rate

Left-ventricular (LV) cardiomyocytes were isolated from infarcted (MI) and sham-operation (sham) animals and loaded with the voltage-sensitive dye FluoVolt as previously described. The dish was placed in the incubator/stimulator and temperature equilibrated for 10min before initiating pacing equilibration for 5min (2ms pulse, 3 Hz) using a stimulus amplitude of 40V (exceeding depolarisation threshold).

Action potentials from each cell were sequentially recorded at 3Hz, 2Hz and 1Hz, respectively. Approximately 15 beats were allowed after each frequency change for APD to reach steady state (in line with measurement of restitution in whole hearts). This was repeated throughout, and the dish was replaced with fresh cells every 30 min. The experiment was terminated when cells began to show signs of deterioration (i.e. unable to follow 3Hz pacing, membrane blebbing, ectopic beats, hypercontraction).

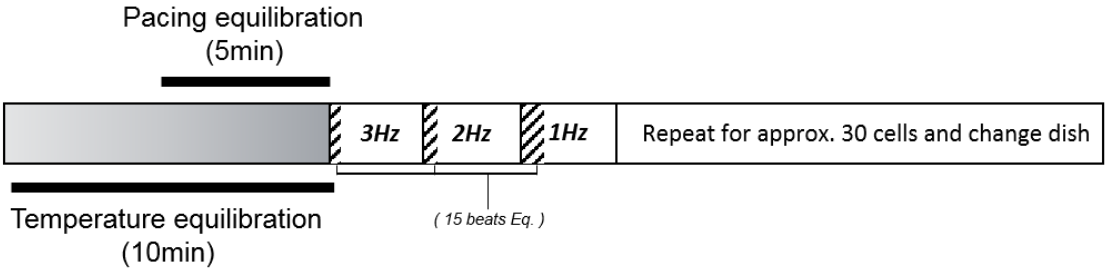

Figure 5.3 Pacing and recording protocol diagram. Multi-frequency recording protocol. Each cell was serially paced at 3Hz, 2Hz and 1Hz. A minimum train of 5 APs was recorded for each frequency.

5.2.2 Transmural comparison of sham and MI hearts

The sub-epicardial and sub-endocardial layers of the left ventricle were dissected (~1 mm thickness) apart and cells were isolated enzymatically and loaded with FluoVolt as previously described. Cells were paced at 500ms cycle length (2 Hz) using field stimulation. This frequency was selected because it was the rate at which ~95% cells would consistently pace, and consequently the most relevant comparison to rabbit physiology attainable through field stimulation.

In infarcted hearts, the infarct (apical) and peri-infarct regions were removed. The same procedure was applied to an approximation of this region location and size in sham hearts.

5.3 Results

5.3.1 Multi-frequency APD response in MI vs sham

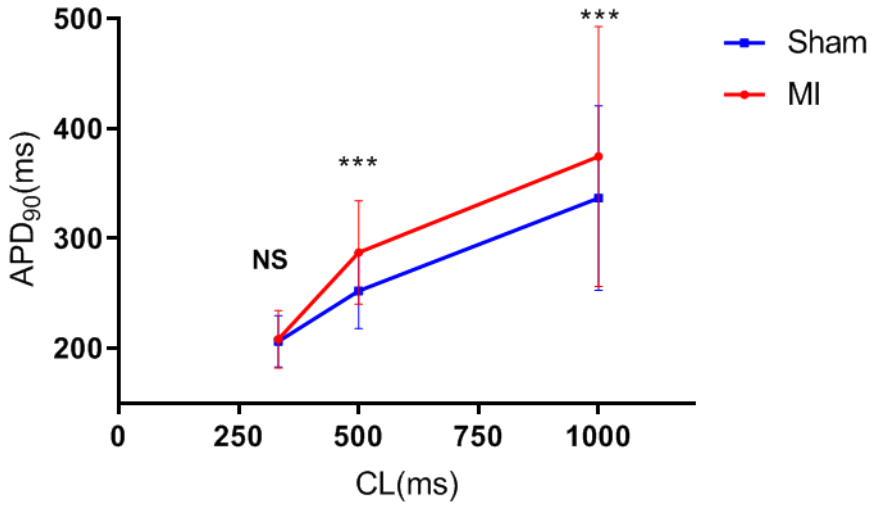

Figure 5.4 Frequency dependence of APD. Relationship between APD90 and pacing frequency in sham and MI cell populations. Data shown as mean ± SD. (n_{1000ms}=233 vs. 170; n_{500ms}=225 vs. 174; n_{333ms}=225 vs. 98, N_{hearts} = 6 vs 3-6*.

As shown in Figure 5.4, the positive relationship between APD and cycle length was evident in both sham and MI groups. No difference between MI and sham was found at 3 Hz (208±10 vs 206±15 ms, respectively; P>0.05, unpaired t-test), however MI APD was significantly longer than sham at 1 Hz (370±13 vs 328±15ms, P<0.001, unpaired t-test) and 2 Hz (277±13 vs 245±15 ms, P<0.001, unpaired t-test). This conventional display of cell populations, using mean ± SD, masks variation present within cell groups, illustrated in Figure 5.5, made using the same datasets.

*Cell groups were sampled from 6 MI animals, 3 of which were not stimulated at 3Hz.

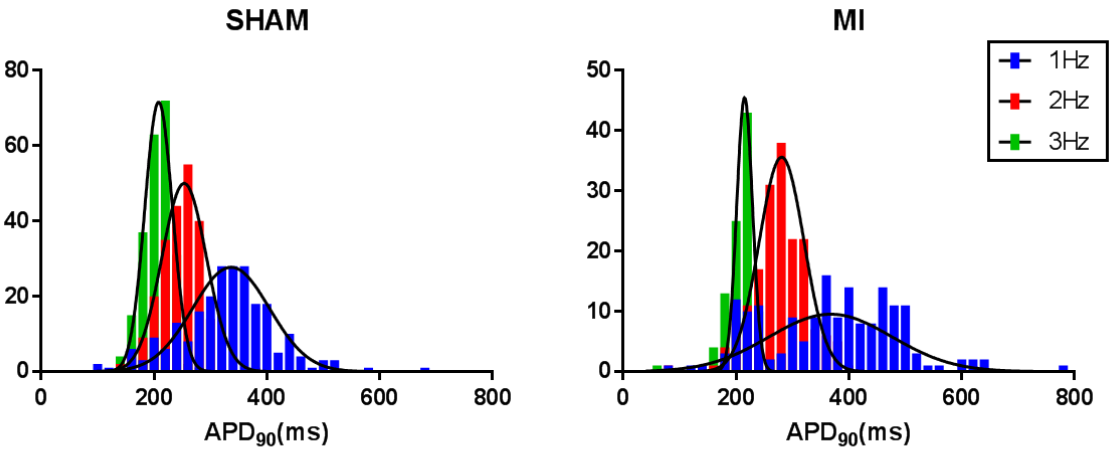

	1Hz	2Hz	3Hz
N	6	6	6
n	233	225	225
Mean	328.5	245.5	206
S.D.	83.98	34.6	23.51
CoV	25.56%	14.09%	11.41%
IQR	91.2	47.3	34.2

	1Hz	2Hz	3Hz
N	6	6	3
n	170	174	98
Mean	370	277.5	208.2
S.D.	118.4	47.07	26.12
CoV	32.01%	16.96%	12.55%
IQR	172.9	56.4	29.5

Figure 5.5 Histogram of cell populations serially paced at 3 frequencies. Frequency distributions of paired measurements in individual cells at 3 Hz (green), 2 Hz (red) and 1 Hz (blue). Sham and MI animals are compared. Gaussian curves were fit to each population of cells at every frequency tested. Three separate measures of statistical variation were used to describe population spread between groups: standard deviation, coefficient of variation, and interquartile range. All three show an increase in variation at all frequencies in MI. All measures of variation measured showed MI APD values were more heterogeneous than in sham.

Displaying these data as mean and standard error can be misleading, as contrasted in Figure 5.5, where each APD_{90} measurement population is shown to largely overlap at all three frequencies, despite heterogeneity decreasing with increases in pacing rate, as described by an increase in kurtosis and a decrease in measures of spread (STD, CoV, IQR). While mean APD_{90} did not differ significantly between groups at 3 Hz, MI cell populations were more variable than sham populations at all rates in three measures of variability, including coefficient of variation (σ/mean), inter-quartile range (75^{th} - 25^{th}% percentile), and standard deviation (σ).

5.3.1.1 Sham vs MI distribution analysis of APD_{90} measurements

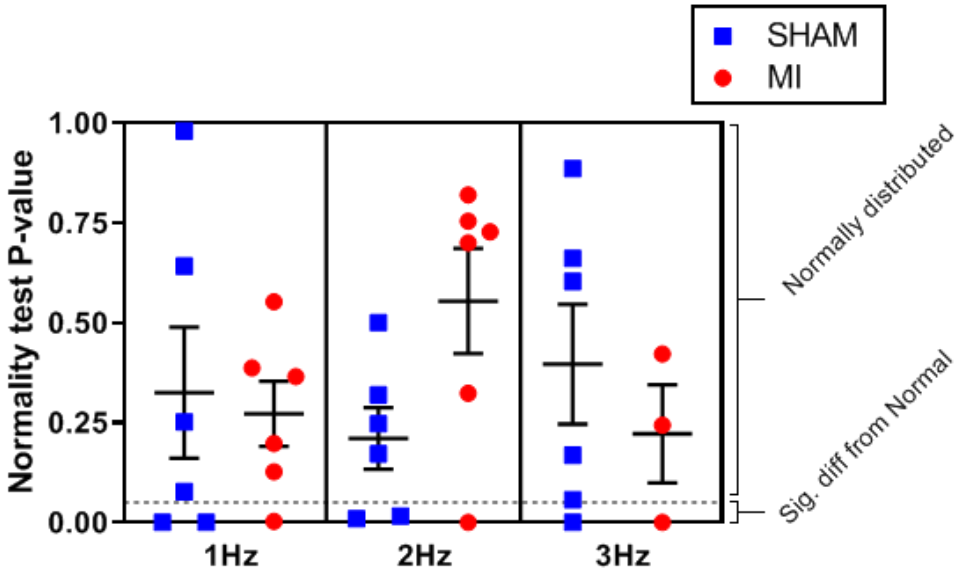

Figure 5.6 Degree of normality comparisons. P-value result of normality testing (D'Agostino & Pearson normality test) on populations of APD_{90} measurements from MI and sham hearts at 3 pacing rates. P-values below 0.05 (dotted line) were significantly different from Gaussian (Unpaired t-test). The majority of APD_{90} measurements were normally distributed. Line and error bars show mean and SEM.

Conventional normality testing on data populations has a binary outcome. This may not be an ideal way to appreciate the degree or extent of distribution normality. Consequently, each cell population from individual animals were subjected to a normality test and its p-value was recorded. If the p-value of the test was greater than 0.05, the distribution was not considered consistent with a Gaussian distribution, and conversely, if the p-value was less than 0.05, the distribution was considered inconsistent with a Gaussian distribution.

The P-values from the normality test of each cell population were plotted and compared between conditions at each frequency tested. No significant differences were found between groups except at 2 Hz ($P<0.05$, t-test). This result shows that pacing frequency did not affect APD_{90} distribution shape significantly, and that MI animals displayed a greater degree of normality at 2 Hz than sham animals (see Figure 5.6), however this is unlikely to carry biological significance.

5.3.1.2 APD, triangulation and upstroke in sham and MI

As discussed previously (Figure 2.11), the triangulation index was calculated as the time (in milliseconds) between APD_{30} and APD_{90}, and scaled for total AP duration (APD_{90}).

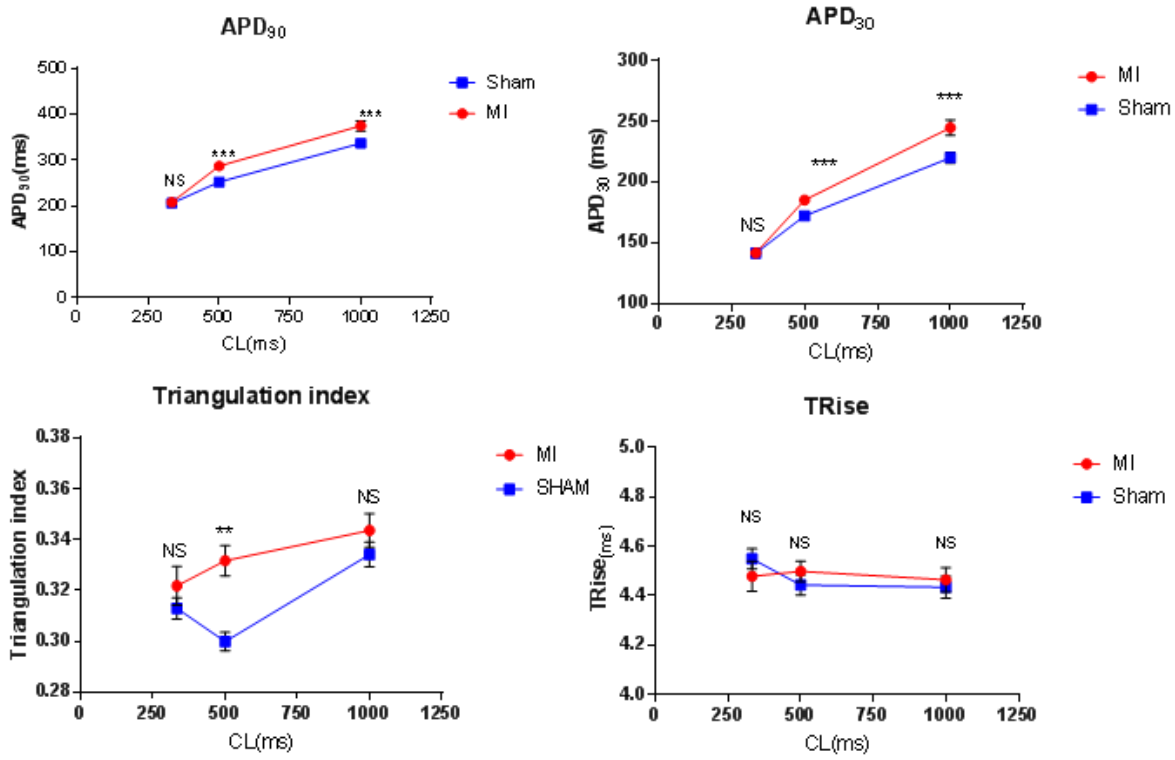

Figure 5.7 Action potential morphology parameters in response to changes in pacing frequency. Relationship between pacing frequency and AP characteristics between sham and MI groups. Data plotted are mean ± SEM. Statistical comparisons between MI and sham at same frequency. (n_{1000ms}=233 vs. 170; n_{500ms}=225 vs. 174; n_{333ms}=225 vs. 98, N_{hearts} = 6 vs 6)

5.3.1.3 Sham vs MI AP characteristics at 3 frequencies

APD_{90} and APD_{30} were both prolonged in MI at slower pacing frequencies (1 Hz and 2 Hz) ($P<0.001$) but not at 3 Hz ($P=0.461$). Triangulation index of action potentials was not significantly different between sham and MI except at 2 Hz ($P<0.01$, unpaired t-test). TRise was not significantly different between groups at any frequency tested (see Figure 5.7).

A prolongation in APD_{90} and APD_{30} in the MI group reflects a loss of hERG in these animals, prolonging the plateau phase of the AP, and delaying repolarisation compared with controls. Triangulation does not appear to vary between groups at 2 of the 3 frequencies tested, indicating the overall shape factor of the action potential remains relatively constant in early stages of HF, compared with controls.

5.3.1.4 Heterogeneity in AP characteristics

The coefficient of variation (CoV) was used to provide a measure of heterogeneity of datasets. Firstly, CoV was calculated for each animal and plotted as the mean ± SEM to describe typical heterogeneity *within* animals (Figure 5.8). Secondly the CoV of all cells (from all animals) was calculated to describe heterogeneity *between* animals. The latter was plotted with mean CoV only as each condition is treated as N = 1 (Figure 5.9).

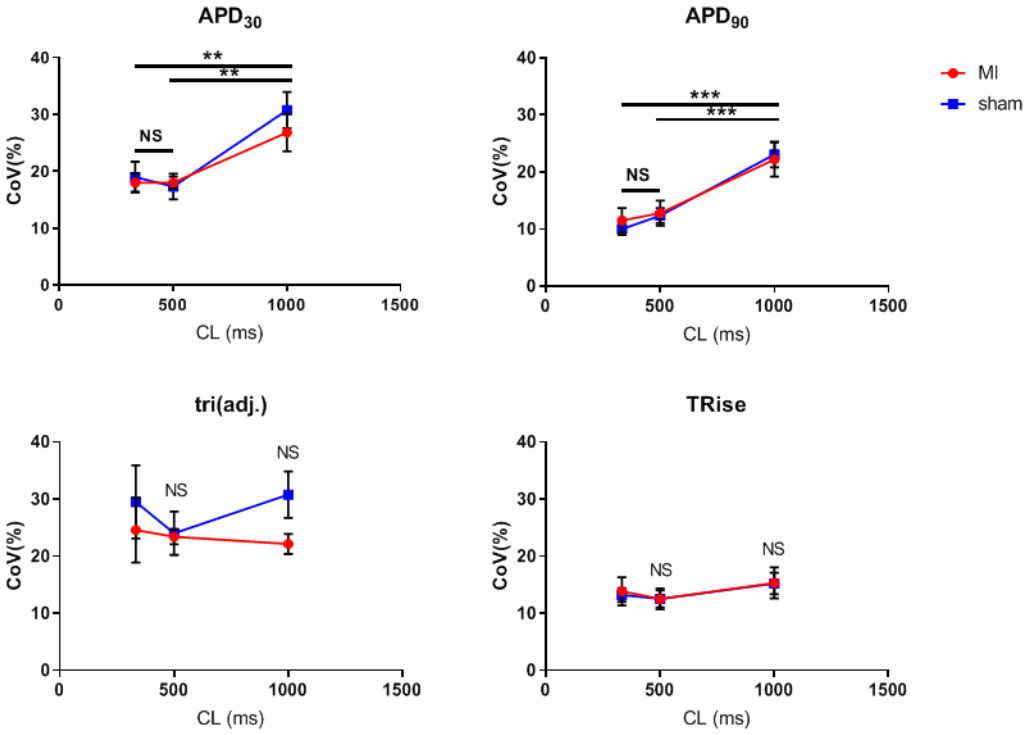

Figure 5.8 Intra-animal variation comparisons. Intra-animal variation. Mean (±SEM) of individual animal coefficients of variation to compare animal-animal across pacing rates. APD_{30} and APD_{90} heterogeneity significantly increases at slower pacing rates. No significant difference was found between sham and MI groups at any frequency. Significance levels displayed on figure describe sham comparisons only (One-way ANOVA, Tukey's multiple comparison test). Frequency groups were not different from one another in MI (Mixed-effects analysis) (n_{1000ms}=233 vs. 170; n_{500ms}=225 vs. 174; n_{333ms}=225 vs. 98, N_{hearts} = 6 vs 3-6).

Figure 5.8 above shows no difference in MI heterogeneity across tested frequencies. One-way ANOVA could not be used due to 3 animals missing the 3Hz group (not tested experimentally).

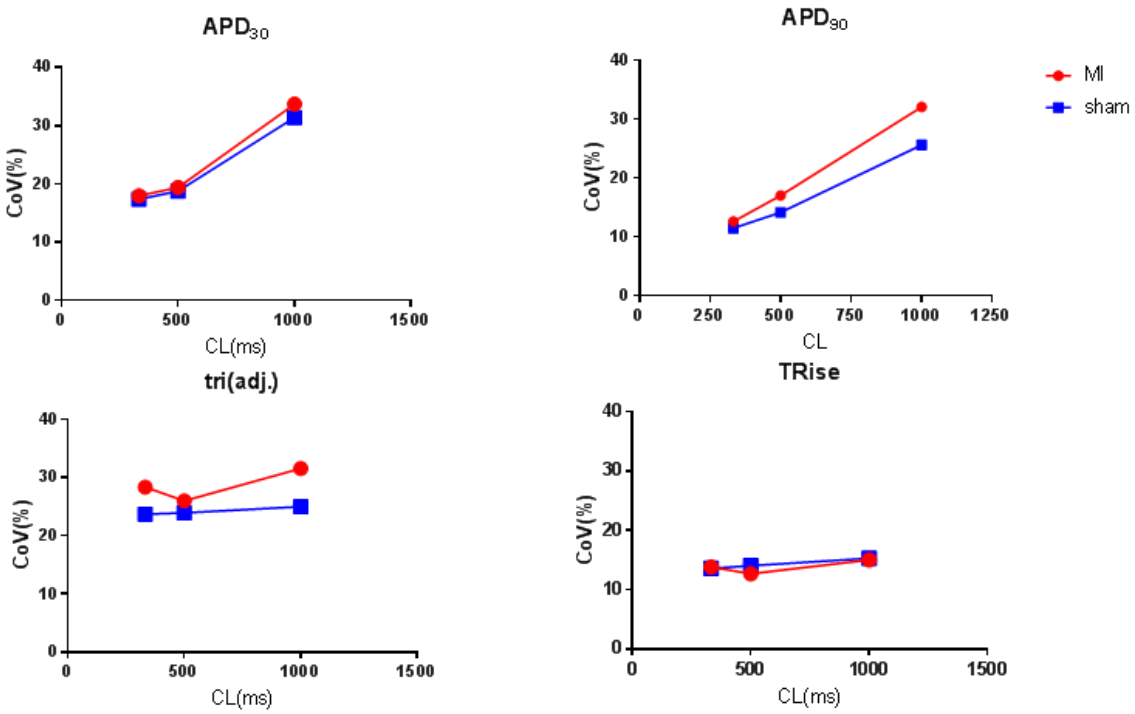

Figure 5.9 Inter-animal variation comparisons. Coefficient of variation of APD_{30}, APD_{90}, TRise and Triangulation index. The coefficient compares all cells from animals as a single population, hence the absence of error bars. Variation decreases as a function of faster pacing frequencies in both groups. MI repolarisation (APD_{30}, APD_{90}, Triangulation) is more variable than sham at all frequencies tested. Upstroke time does not change noticeably between groups or frequencies.(n_{1000ms}=233 vs. 170; n_{500ms}=225 vs. 174; n_{333ms}=225 vs. 98, N_{hearts} = 6 vs 3-6).

5.3.2 Transmural AP morphology in infarcted heart

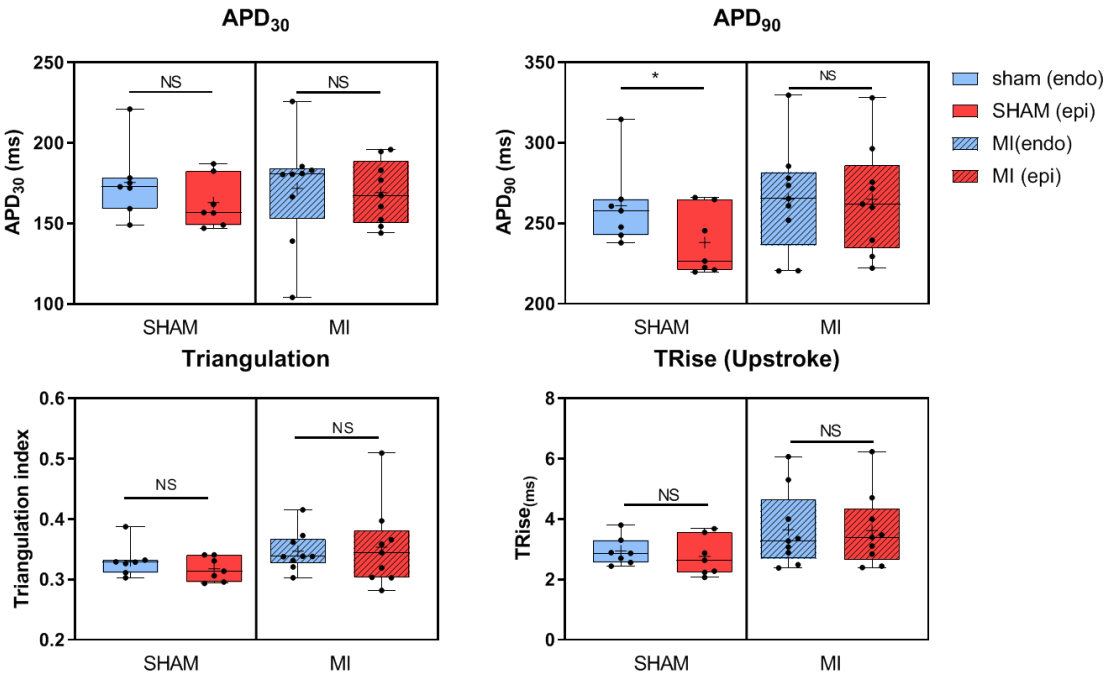

Figure 5.10 Transmural voltage parameter comparisons between sham and MI. Box plots of AP parameters comparing sub-endocardial and sub-epicardial cells in sham and MI animals at 2 Hz pacing frequency. Data points shown are each animal mean. N_{sham}=7, N_{MI}=9)

Hierarchical analysis (Code available in Appendix, p139) was carried out to compare transmural differences in four action potential parameters in sham, and MI animals (Table 1). The early repolarisation duration (APD_{30}) was not significantly different between regions in either sham or MI. Sham animals displayed a significant transmural difference in APD_{90}, which was lost in MI animals. Triangulation index normalised to AP duration was not different transmurally in either condition. Finally, AP upstroke duration was not found to be different between any of the tested groups of animals.

Sham (*N=7*)	Endocardium (n = 632)		Epicardium (n = 652)		Δ Delta (Endocardium-Epicardium)		*Hierarchical test results*	
	Mean	*σ*	*Mean*	*σ*	*Mean*	*S.E.M*	*95% CI*	*P-value*
APD_{30} (ms)	173	37.5	166	34.6	n/a	n/a	(-2.9 , 25.4)	0.1
APD_{90} (ms)	259	37.6	246	38.4	21.4	6.1	(6.8 , 36.0)	***0.01092**
Triangulation	0.334	0.110	0.326	0.087	*n/a*	*n/a*	(-0.01 , 0.05)	0.3189
Trise (ms)	2.69	1.45	2.91	1.40	n/a	n/a	(-0.8 , 0.4)	0.4729
MI (*N=9*)	**Endocardium (n = 608)**		**Epicardium (n = 635)**		**Δ Delta (Endocardium-Epicardium)**		***Hierarchical test results***	
	Mean	*σ*	*Mean*	*σ*	*Mean*	*S.E.M*	*95% CI*	*P-value*
APD_{30} (ms)	181	42.9	175	44.2	*n/a*	*n/a*	(-32.0 , 37.1)	0.8694
APD_{90} (ms)	265	55.7	273	58.7	*n/a*	*n/a*	(-37.4 , 20.5)	0.5166
Triangulation	0.340	0.081	0.336	0.097	*n/a*	*n/a*	(-0.07 , 0.05)	0.7504
Trise (ms)	3.47	2.70	3.52	2.40	*n/a*	*n/a*	(-1.3 , 1.2)	0.9747

Table 1 Transmural voltage parameter comparisons between sham and MI. Sub-endocardial and sub-epicardial action potential parameters in sham and MI animals. Data shown are means and standard deviation. Endo/Epi comparisons and transmural ∆(ms) utilized hierarchical analysis to determine statistical significance.

5.3.3 Transmural analysis of AP morphology in cell populations

Below is an illustrative example of standard statistical analyses (unpaired t-tests) in pooled groups of cell populations from 7 (sham) and 9 (MI) animals.

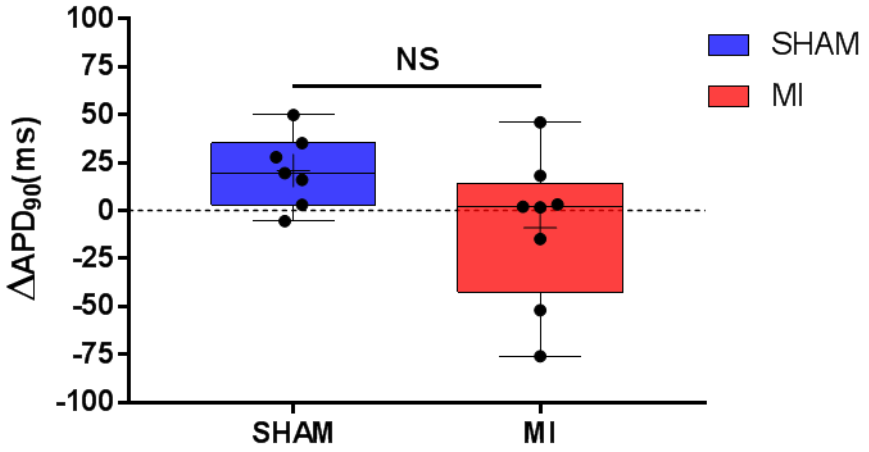

Figure 5.11 Mean endocardium-epicardium APD_{90} difference in sham and infarcted hearts. Mean transmural difference in repolarisation time between sub-endocardium and sub-epicardium of individual animals (each point = $Endo_{APD}$ – Epi_{APD}). The sham group was significantly different from 0 (One-sample t-test; P = 0.026), while MI was not (One-sample t-test; P = 0.536). Sham and MI ΔAPD_{90} were not significantly different from one another (P>0.05).

Figure 5.11 illustrates the importance of hierarchical approaches to clustered datasets. Standard t-test analysis using the mean difference between endocardial and epicardial APD_{90} only provides a limited appreciation of population behaviour, and does not take into account the number of cells sampled to calculate each heart's mean APD_{90}.

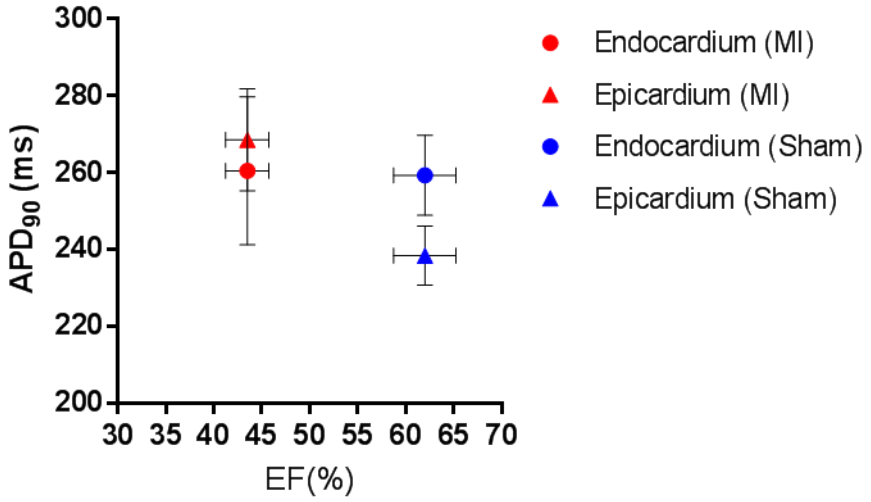

Figure 5.12 Ejection fraction (%) and APD_{90} Mean ejection fraction (%) (±SEM) plotted against the mean APD_{90} of endocardium and epicardium in MI and Sham groups. Endocardium-epicardium gradient is lost in the MI group. (N_{endo}= 6; N_{epi}= 6).

A factor influencing remodelling, and changes in APD gradients across the LV wall is the degree of severity of the infarct. One way of quantifying the extent of LV damage is to assess each animal's ejection fraction (EF%). While this is only an indication of the damage sustained by the muscle, it provides context to the range of transmural APD found in the MI group. The ejection fraction was assessed by echocardiography. Analysis of the echocardiographic data from both groups was blinded.

	ENDOCARDIUM				
	sham		MI		
	Mean	*σ*	*Mean*	*σ*	*P-value*
APD_{30} (ms)	173	37.5	181	42.9	**<0.001*** **
APD_{90} (ms)	259	37.6	265	55.7	**<0.05***
Triangulation	0.334	0.110	0.340	0.081	**0.2876**
TRise (ms)	2.69	1.45	3.47	2.70	**0.001****

Table 2 Region-specific (sub-endocardium) comparison of sham and MI AP parameters. Comparison of sub-endocardial cell AP parameter means in pooled populations of sub-endocardial cells from sham and MI animals (unpaired t-test).

	EPICARDIUM				
	sham		MI		
	Mean	*σ*	*Mean*	*σ*	*P-value*
APD_{30} (ms)	166	34.6	175	44.2	**<0.001*** **
APD_{90} (ms)	246	38.4	273	58.7	**<0.001*** **
Triangulation	0.326	0.087	0.336	0.097	**0.0576**
TRise (ms)	2.91	1.40	3.52	2.40	**0.001****

Table 3 Region-specific (sub-epicardium and sub-endocardium) comparison of sham and MI AP parameters. Comparison of sub-epicardial cell AP parameter means in pooled populations of sub-epicardial cells from sham and MI animals (unpaired t-test).

Statistical comparison between sham and MI sub-endocardial cells found prolongation of APD_{30}, APD_{90} and TRise in MI (+8.1 ms; + 4.3 ms; +0.8 ms, respectively). Triangulation index was unchanged in either region. Sub-epicardial MI cells also exhibited prolonged APD_{30}, APD_{90} and Trise relative to shams (+8.4 ms; + 27.3 ms; +0.6 ms, respectively. The largest change observed in the MI group was APD_{90} prolongation, prominent in the sub-epicardium region, and modest in the sub-endocardium region (+27 ms and +16 ms, respectively).

5.3.4 Transmural action potential heterogeneity

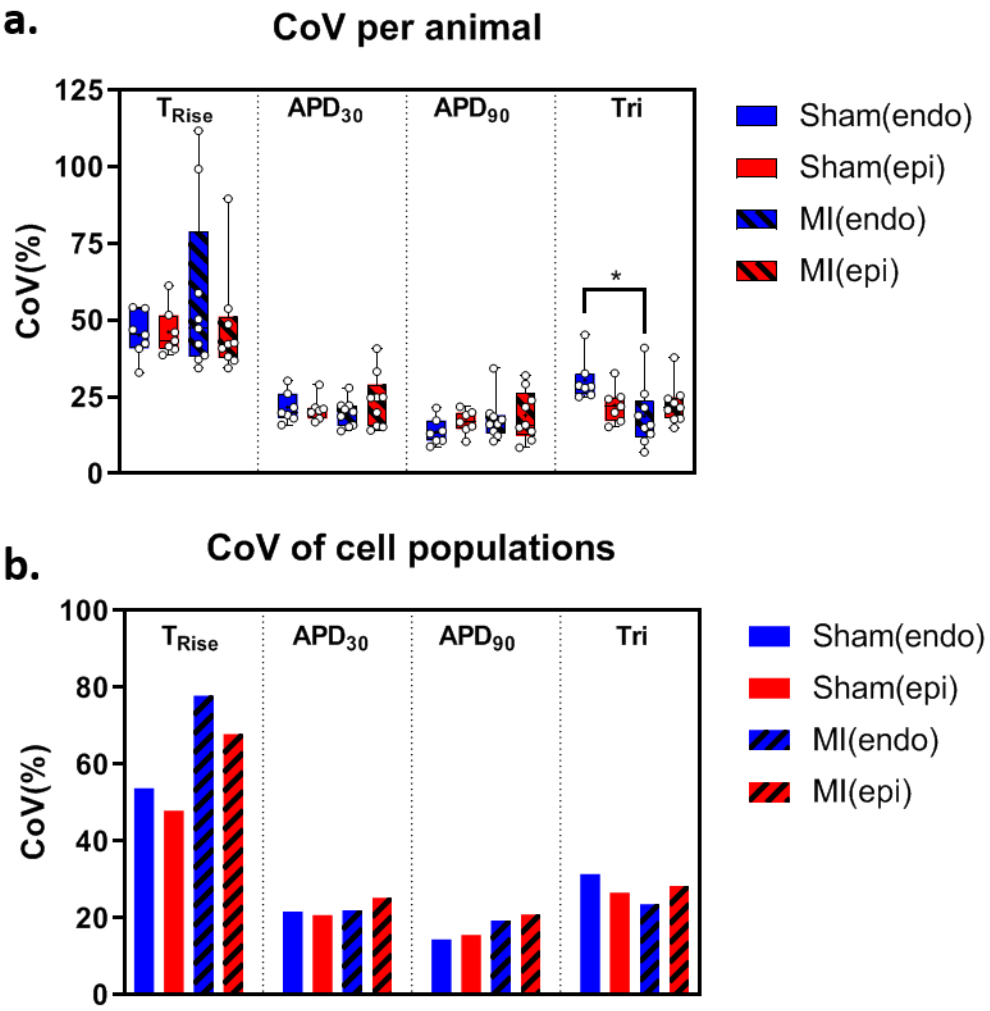

Figure 5.13 Inter- and intra-animal variation comparisons. (a) Box plots of individual animal coefficients of variation during upstroke (TRise) and phases of repolarisation (APD_{90}, APD_{30}, Triangulation index). (b) CoV of all cells sampled from sham and MI hearts (N = 7-9).

The CoV of AP parameters was not significantly different between regions (endocardium/epicardium) or conditions (sham/MI), except for AP triangulation, which was significantly greater in sham endocardium than MI endocardium (One-way ANOVA, P = 0.025). (see Figure 5.13)

Comparing cell populations from all animals showed consistently higher CoV in MI groups in TRise, APD_{30} and APD_{90}, but not triangulation.

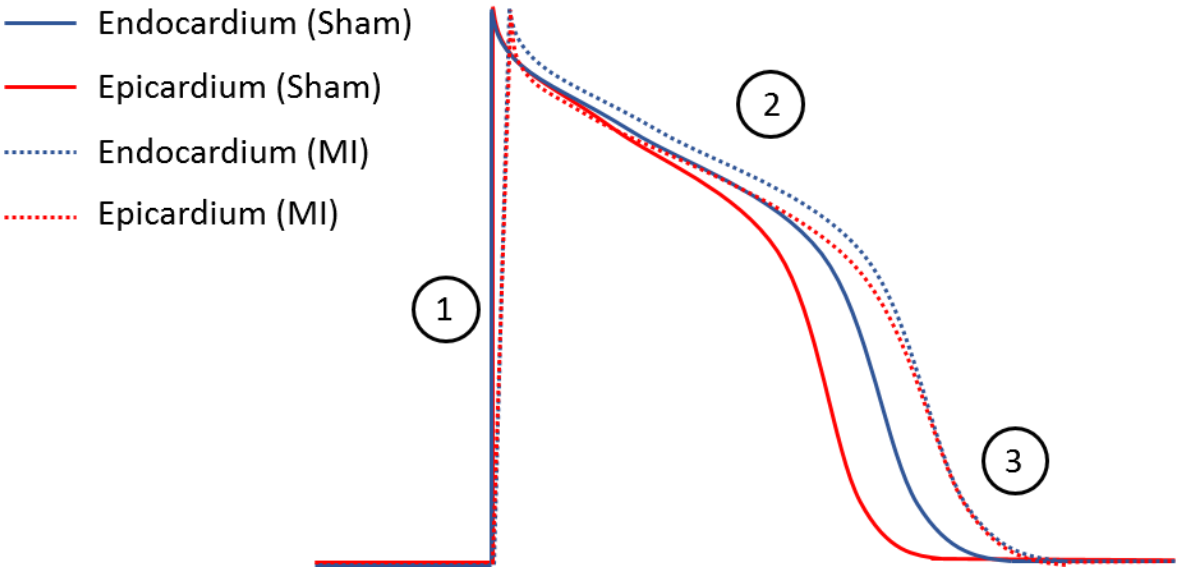

Figure 5.14 Diagram of MI-induced AP changes. Diagrammatic representation of the action potential differences found transmurally between the sham and MI groups.

(1) Both MI endocardium and epicardium have significantly slower upstroke rates than sham in respective regions. (2) APD_{30} increases in both regions, and remains significantly different between endocardium and epicardium in MI. Both endocardium and epicardium show increases in APD_{90}, and do not differ significantly after MI, predominantly due to epicardial APD_{90} increase (see Figure 5.14).

5.3.4.1 Hierarchical analyses

Hierarchical analyses of endocardium-epicardium repolarisation differences within individual animals showed the transmural repolarisation gradient present in sham was lost in MI (Table 1).

5.3.5 Transmural APD_{90} in MI and sham

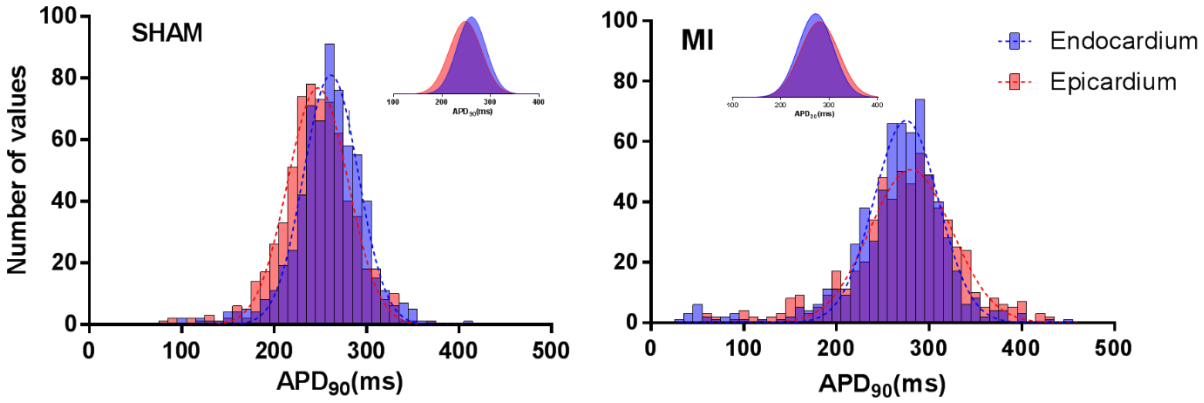

SHAM		
	Endocardium	Epicardium
n	632	652
N	7	7
Mean	259.0	246.1
S.D.	37.6	38.4
CoV	14.5	15.6
IQR	41.8	44.5

MI		
	Endocardium	Epicardium
n	608	635
N	9	9
Mean	265.3	273.3
S.D.	55.0	56.0
CoV	20.8	20.5
IQR	51.1	59.9

Figure 5.15 Histograms of APD_{90} in sub-endocardium and sub-epicardial cells from sham and MI animals. Subplots show gaussian fit of all endocardial/epicardial cells from all animals together. Tables show mean APD_{90} in each group and measures of variation.

Transmural comparison of APD_{90} between sham and MI animals shows a high degree of APD_{90} overlap between cells from the inner and outer layers of the left ventricle. While the shift in distribution is detected statistically using these large datasets, a given cell picked at random would give no indication as to its origin within the LV from its APD alone, once again highlighting the importance of obtaining adequate numbers of observations via increased throughput in studies of this nature.

Sham animals show significantly greater APD in endocardium 259±14 ms vs epicardium 246±15 ms. On average, MI animals show no difference between groups (Hierarchical test, $P = 0.0109$ and $P = 0.516$, respectively.).

5.4 Discussion

5.4.1 Electrophysiology of the left ventricle

5.4.1.1 Action potential upstroke

The speed of action potential upstroke was measured in all cells, and shows no significant change between pacing frequencies ranging from 1 to 3 Hz. Furthermore, no difference in upstroke time was found between cells in populations sampled from the whole ventricle of sham and MI animals. While these measurements may well reflect the underlying physiology (i.e. I_{Na} function), it is likely that measuring fast events in the millisecond range using fluorescent techniques does come with limitations and systematic error (e.g. trace filtering). Such limitations and potential improvements were addressed in Chapter 4. The estimates of TRise derived from these action potential trains may therefore only be relevant in the context of relative comparison between groups measured and analysed using identical filtering.

5.4.1.2 Action potential duration

The APD_{90} measured in MI cell populations from 6 animals confirms earlier work (McIntosh, Cobbe and Smith, 2000), showing no difference in APD between MI and control at fast, pseudo-physiological rates (3 Hz), and an APD difference of +20-30 ms only evident at slower pacing rates (1 Hz and 2 Hz). This work constitutes a significant improvement in cell sampling throughput per animal, using 12 animals (6 sham, 6 MI) versus 39 animals (14 sham, 25 MI) to sample ~200-300 cells. Moreover, increasing the sample size (cells per animal) provided a measure of variability between cells as well as animals in response to different pacing frequencies.

Additionally, the frequency and transmural site-dependence of prolongation was demonstrated previously in a model of LV hypertrophy (McIntosh *et al.*, 1998), which was successfully replicated here.

5.4.1.3 Action potential morphology

Action potential shape was assessed by reducing it to a single number, triangulation index. It constitutes a useful tool to quantify the degree of plateau present on a given AP. It is important to note the triangulation index reported in literature so far has been the duration between APD_{30} and APD_{90}, in milliseconds. This work differs from this convention, by considering the total duration of the AP (Chapter 2) and reporting triangulation as a ratio.

Changes in AP triangulation previously reported may consequently have been positively skewed by comparing AP groups of different durations, potentially overestimating increased triangulation in this way. This normalisation of AP triangulation to AP duration was especially important in this work as the AP durations were increased in MI, spuriously increasing the non-normalized triangulation index.

While AP triangulation was found to be higher in the MI group at only one of the tested pacing frequencies (2 Hz), its heterogeneity among populations showed an increase in MI hearts, at all three frequencies tested.

5.4.1.4 Inter- and intra- animal heterogeneity

The coefficient of variation (σ/μ) was selected as a measure of heterogeneity due to its lower sensitivity to outliers than standard deviation or range, as it is weighted for the mean. CoV was recorded for each animal to determine the degree of cell-cell variation present within individual animals. CoV was also calculated for all animals using all values obtained from individual cells, thus conserving total variation within populations. The main factor affecting heterogeneity in these experiments was a slowing in pacing rate. As the pacing rate approached normal rabbit physiological rates, heterogeneity decreased equivalently between MI and sham cell populations, and no significant difference was found between groups at 3 Hz.

LV heterogeneity increased at slower pacing rates, but was interestingly not found to differ between MI and sham groups. The APD heterogeneity of isolated cell populations is greater than in the whole heart (~2 to 5-fold at equivalent pacing rates, see Appendix, Table 5), principally due to an absence of cellular coupling through gap junctions, as well as intrinsic variation in ion channel expression between individual cells.

Inter-animal heterogeneity was greater in MI than sham in APD_{90}, APD_{30}, and triangulation, but not upstroke time. This was true of all pacing frequencies, and most pronounced at the slowest rate (1 Hz). This is relevant to the reported phenomenon of disparate drug effects observed between males and females, different ethnic groups, and genetically predisposed groups such as LQTS patients (Niemeijer *et al.,* 2015). Given the heterogeneity found in inbred, gender, weight and age-matched rabbits, it is not unreasonable to think other factors such as gender, ethnic group, or pathophysiological profiles would also drive comparable or superior levels of heterogeneity in affected groups.

5.4.2 Transmural comparisons

5.4.2.1 Action potential upstroke

The AP upstroke was not found to differ between sub-endocardial and sub-epicardial cells from the same heart. The upstroke was significantly prolonged in sub-endocardium and sub-epicardium MI (~50%) compared to sham. This slowing in depolarisation time from resting membrane potential has previously been reported in border zone cells (Pinto & Boyden, 1999) and following acute and chronic ischaemia (Rodríguez, Trayanova and Noble, 2006).

It is worth noting that the measurement of upstroke could serve as a quality control of cells sampled, by demonstrating the absence of M-cells. M-cells have faster rates of depolarisation ($\frac{dV}{dt}$max) and distinctly longer APs than other cell subtypes (Antzelevitch *et al.*, 1999; McIntosh, Cobbe and Smith, 2000), and their absence from our cell populations can attest none, or few mid-myocardial cells were present.

Transmural heterogeneity of TRise was much greater than other AP parameters, (CoV 60-70%), approximately two-fold that of the repolarisation indexes. This phenomenon is likely the result of a strong sensitivity of TRise to small changes in sodium channel expression and activation. The maximal rate of depolarisation ($\frac{dV}{dt}$max) of CMs is highly sensitive to the number of active Na^+ channels participating in membrane depolarisation. The resting membrane potential affects the activation state of these channels, potentially prematurely causing some to open if the cell is already slightly depolarised but still below threshold (~-85mV). Furthermore, dV/dt_{max} is inversely proportional to the square of the sodium ion current activation, which explains substantial changes in upstroke time can be caused by small fluctuations in I_{Na} activation.

Na^+ channels have been reported to decrease in number and delocalise from the cell ends following MI, and for the cell resting potential to increase after infarct-induced remodelling. This work showed TRise in MI animals was found to be slower, and display greater heterogeneity than sham, which further supports the concept of subtle changes in sodium channel activity causing asynchrony in cell depolarisation.

5.4.2.2 Action potential duration

Two types of comparisons were made with regards to transmural action potential assessment. Firstly, endocardium-epicardium differences were compared, using a hierarchical approach

to adequately account for the clustering present within individual hearts. Secondly, region-specific comparisons were made between MI and sham groups. The early index of repolarisation APD_{30} was not found to differ between sub-endocardium and sub-epicardium in either sham or MI groups. Later stages of repolarisation (APD_{90}), in contrast, showed a loss of difference in the MI group, retained in sham.

The consequences of the transmural gradient of APD is unknown. Myles *et al.*, (2010) showed APD was directly dependent on activation sequence, by stimulating endocardially and epicardially, showing a reversal in APD gradient. The natural conclusion of this work is that cellular differences in APD are a consequence, and not a cause of the endo-epi position, and may result from the chronic electrical and mechanical differences across the ventricular wall in both health and disease. The loss of transmural difference therefore may reflect different mechanical conditions in the LV wall post MI.

Cell with very short action potentials (<100ms) were rare but did cause an increase in measures of repolarisation heterogeneity, specifically in the MI procedure group (see Figure 5.15). Large reductions in APD have been attributed to the K_{ATP} channel in isolated cells, whereby activation of K_{ATP} leads to AP shortening and decreased cell excitability (Faivre and Findlay, 1990). The opening of a very small fraction of K_{ATP} channels present in CMs (1%) has been shown to cause a 50% decrease in APD (Faivre and Findlay, 1990), and as little as 10% opening causing cell inexcitability altogether (Findlay *et al.*, 1989).

5.4.2.3 Action potential morphology

The index of triangulation was not found to differ transmurally between sub-endocardium and sub-epicardium in sham or MI.

5.4.2.4 Hierarchical analyses

Hierarchical analysis confirms a loss in repolarisation gradient between sub-endocardium and sub-epicardium regions of the MI rabbit model. This technique highlights the potential pitfalls of conventional clustered statistics in multi-condition groups with varying sample sizes.

5.4.3 Conclusions

The study of pathology requires a proper appreciation of the variability of electrophysiology in normal states. The electrical behaviour of isolated CMs exhibits vastly more variability than coupled tissue, where these cellular differences and potential sub-populations of behaviours could go unnoticed. As discussed later, marrying single cell experiments to whole heart studies could help further understand the implication of cell-cell heterogeneity on the overall electrical behaviour of the heart.

Chapter 6: Regional heterogeneity in left ventricle

6.1 Background

6.1.1 Heterogeneous electrical activity of the left ventricle

As discussed previously, electrical phenotypes can vary considerably between different regions of the heart muscle. It has been proposed that electrical gradients above a certain threshold across the myocardium contribute to pro-arrhythmic activity (Maruyama *et al.*, 2011). The exact physiological prerequisites for the generation of these gradients is not currently well-understood. While a measure of repolarisation heterogeneity is expected, too much, or too little, variation could serve as a pro-arrhythmic substrate. Quantification of repolarisation heterogeneity has so far been sampled the at organ level using 2D mapping of the epicardium, as other methods using single cells, such as patch clamping, are not able to sample enough cells to provide meaningful measures of spread.

As would be expected, AP duration in electrically coupled tissue is quite tightly constrained, where any given myocardial area is very well synchronized with its neighbouring tissue, forming the near-homogeneous signal triggering synchronous muscle contraction. The heterogeneity in repolarisation duration of individual cells in isolation is considerably higher. This variation, masked in intact tissue, could reveal previously unknown underlying differences between two hearts with seemingly identical ECG waveforms.

Quantification of heterogeneity between cell populations sampled from discrete regions of the myocardium could therefore provide valuable information about the underlying electrical phenotypes within the ventricle. In this way, two hearts could host very different arrhythmic risk, despite displaying potentially identical electrical phenotypes determined by ECG or optical mapping. Furthermore, cardiac remodelling following a myocardial infarction is known to affect repolarisation duration. The effect of remodelling on cell heterogeneity has not yet been investigated, and could play a key role in arrhythmogenic processes.

Naturally occurring repolarisation variation in specific regions of the myocardium has also not been quantified due to logistical issues encountered with throughput. The primary hypothesis of this study is that the repolarisation heterogeneity present within a single heart by far outweighs any variation encountered between hearts.

Lastly, by sub-sectioning heart regions for individual study we will identify whether the heterogeneity in the whole ventricle stems from (1) homogeneous variation in all regions or (2) islands of high and low variation distributed spatially across the LV wall.

6.1.1.1 Regional specificity of APD of endocardium and epicardium

The characteristics of the action potential across the LV (endocardium-epicardium) was investigated in Chapter 4. While the data agreed with literature with regards to average APD, we found extensive variability across both regions studied. This section will summarise the average electrical behaviour and the degree of heterogeneity present in several sub-divisions of the rabbit LV.

6.1.2 Region-specific IKr inhibition

As discussed earlier, the hERG channel, generating IKr, is the dominant channel responsible for the final stage of repolarisation (phase 3), supplemented by I_{Ks}. Inhibition of IKr in results in increased APD and effective refractory period (ERP). Commonly used drugs targeting IKr include dofetilide and clofilium, which are widely prescribed for the management of tachyarrhythmias. Dofetilide is particularly effective in the treatment of atrial fibrillation (AF) and flutter (Jaiswal and Goldbarg, 2014). Unlike many other compounds, dofetilide is highly specific in its inhibition of IKr, leaving other channels involved in AP regulation unaffected (INa, I_{Ks}, ICa-L). In this study we used dofetilide at a sub-maximal concentration (30 nM) to partially inhibit IKr in select sub-populations of isolated cardiomyocytes from the sub-epicardial layer of rabbit hearts.

6.1.3 Region-specific L-type Ca^{2+} channel inhibition

The L-type Ca^{2+} channel is a voltage-dependent Ca^{2+} channel responsible for E-C coupling of skeletal, smooth and cardiac muscle. In cardiac myocytes, it acts by allowing extracellular Ca^{2+} to enter the cytoplasm upon depolarisation, thus modulating both contraction through available Ca^{2+} inside the cell, as well as membrane potential. $I_{Ca\text{-}L}$ is responsible for the plateau (phase 2) of the action potential, opposing repolarising outward K^+ channels, and slowly de-activating as the AP repolarises. Inhibition of $I_{Ca\text{-}L}$ causes AP shortening, by offering no resistance to IKr and I_{Ks}, which quickly restore the cell membrane potential to its resting state. Nifedipine is a L-type channel blocker commonly used to treat high blood pressure (Olivari *et al.*, 1979). Nifedipine reduces Ca^{2+} concentration inside the cytoplasm, thereby inhibiting muscle contraction.

6.1.4 Aims and hypotheses

This chapter focuses on quantifying mean AP duration and repolarisation profiles of isolated rabbit myocytes originating from discrete cardiac regions both in healthy animals and in the rabbit MI model.

To compare APD heterogeneity between heart regions, large samples of cells are required from each region to draw meaningful conclusions from population analyses. In this section, the mean behaviour and variability of action potential populations will be compared at several levels. Namely, the whole left-ventricle, endocardium and epicardium along the entire ventricle (transmural), and finally the epicardial basal and apical regions. These subdivisions of the heart muscle were chosen to maximise cell yield, irrespective of the isolation quality (i.e. cell survival %), by digesting large enough portions of tissue. This choice also allowed the clear delimitation of regions from one another, as the mid-myocardium was discarded, and well as the central part of the epicardial surface to avoid any overlap between compared regions.

6.2 Methods

6.2.1 Transmural APD variation

Cells were isolated as previously described (Chapter 2). The left ventricle was dissected into endocardium and epicardium layers (~2 mm thick), and the mid-myocardium was discarded. Stock and sham rabbits were used for regional comparisons, specified where relevant.

6.2.2 Sub-epicardial base and apex comparison

The epicardium was dissected and separated in three parts, namely the base, middle, and apex. Cells were loaded with FluoVolt and paced at 2Hz at 37°C, as previously described.

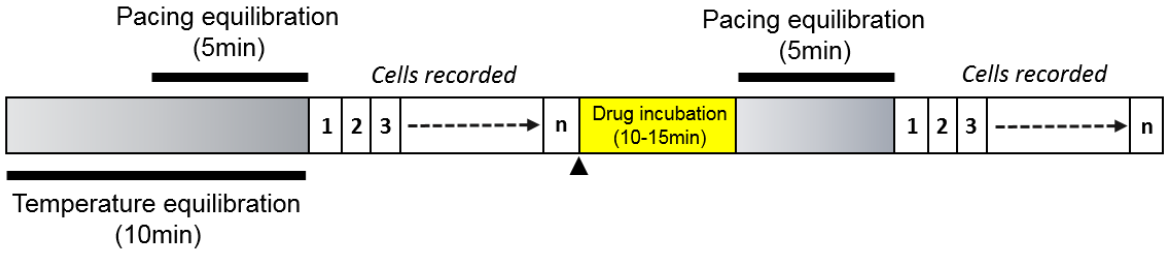

Figure 6.1 Drug incubation and cell recording protocol. Timeline of drug effect protocol for isolated cells.

Dish temperature was brought from RT to 37°C, and pacing at 2Hz was maintained for 5 min (2ms pulse, 40 volt). Action potential trains of 2.5s were recorded from each cell, after which pacing was halted and the drug was introduced to the medium. Drug incubation was carried out by replacing 10% of the total dish volume (200 µl) with 10X drug solution. Pacing was restored for 5 min, and action potential trains were again recorded from the same cells (see Figure 6.1). Cell locations were saved as XY coordinates in order to record the cell post-drug, using a computer-controlled stage.

6.2.3 Pharmacological blockade of L-type Ca^{2+} and hERG channels

All drugs used were prepared in 100% DMSO. Final DMSO concentration was kept low, at 0.05%. hERG blockade was achieved using the specific IKr-blocker dofetilide. A concentration of 30 nM (0.05% DMSO) was used throughout. This sub-maximal concentration was selected to cause a robust AP prolongation at a pacing rate of 2 Hz. A

concentration of 30nM prolonged the AP and minimise the number of cells with APs prolonged beyond the cycle length (500 ms).

L-type Ca^{2+} channel blockade was achieved using Nifedipine. A concentration of 1 μM (0.05% DMSO) was selected to achieve 50% blockade of the channel.

All results shown as net effect after subtraction of vehicle effect (0.05% DMSO) if significant.

6.3 Results

6.3.1 AP parameters throughout left ventricle sub-regions

Cardiac sub-region		APD_{30} (ms)	APD_{90} (ms)	Triangulation index	Trise (ms)
LV (N = 20)	**Mean ± σ**	182.8 ± 38.9	268 ± 49	0.3 ± 0.1	5.7 ± 4.0
n = 949 cells	***CoV (%)***	21.3	18.3	29.0	70.4
Endocardium (N = 6)	**Mean ± σ**	173 ± 37.5	259 ± 37.6	0.3 ± 0.1	2.7 ± 1.4
n = 632 cells	***CoV (%)***	21.7	14.5	31.4	53.8
Epicardium (N = 6)	**Mean ± σ**	166 ± 34.6	246 ± 38.4	0.3 ± 0.1	2.9 ± 0.1
n = 652 cells	***CoV (%)***	20.8	15.6	26.6	48.0
Basal epicardium (N = 12)	**Mean ± σ**	159 ± 43.6	244 ± 53.0	0.4 ± 0.1	3.6 ± 2.5
n = 691 cells	***CoV (%)***	27.4	21.7	27.2	71.4
Apical epicardium (N = 12)	**Mean ± σ**	171 ± 43.4	266 ± 51.9	0.4 ± 0.1	3.1 ± 1.6
n = 646 cells	***CoV (%)***	25.4	19.5	26.0	52.4

Table 4 Summary of AP parameters across 5 major regions of the rabbit LV. Action potential duration at 30%, 90% repolarisation, triangulation index and upstroke time in whole left ventricle, transmurally (sub endocardium/sub-epicardium) and apicobasally.

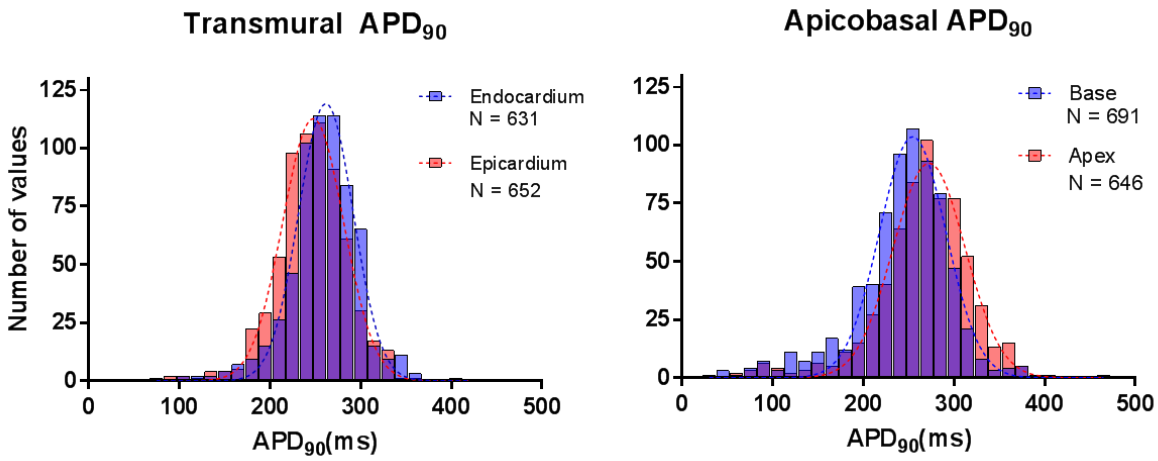

Figure 6.2 Histogram of transmural and apicobasal differences. Histogram of APD_{90} recorded across the LV wall in sub-endocardial and sub-epicardial cells (N=6) (left). Histograms of epicardial apical and basal cell APD_{90} (N=12) (right).

Cardiac subregion comparisons (see Figure 6.2 and Figure 6.3) show extensive overlap of action potential durations between populations of cells, endocardium vs epicardium and epicardial base vs epicardial apex, with equivalent heterogeneity between groups, irrespective of region size (i.e. base and apex of epicardium vs entire epicardium).

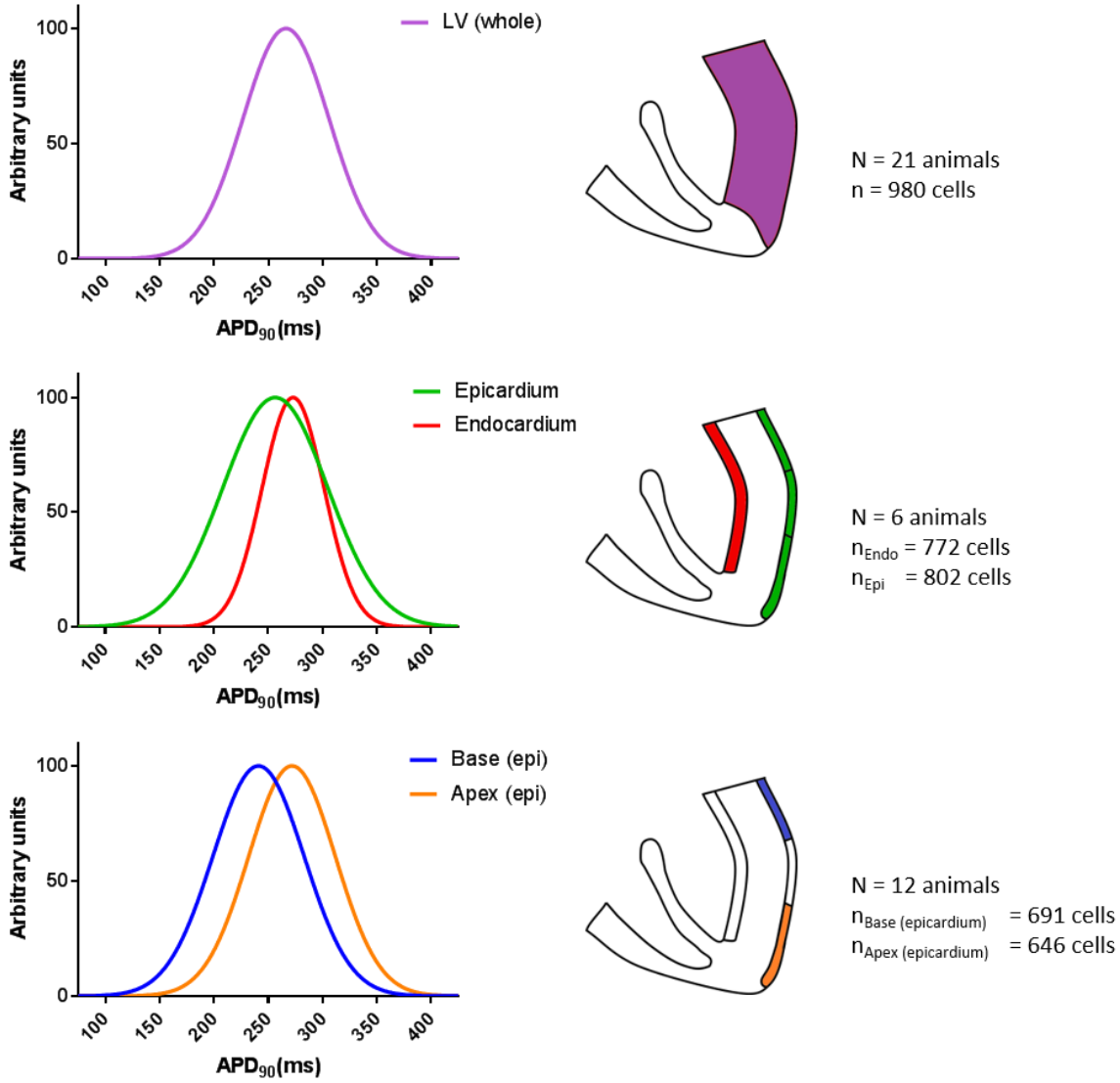

Figure 6.3 Heterogeneity in the left ventricle Gaussian fit generated using the mean APD_{90} and mean standard deviation obtained from populations of animals.

Figure 6.3 shows the electrophysiological heterogeneity present within the myocardium is extensive, despite selecting reasonably small sub-regions (epicardial base and apex).

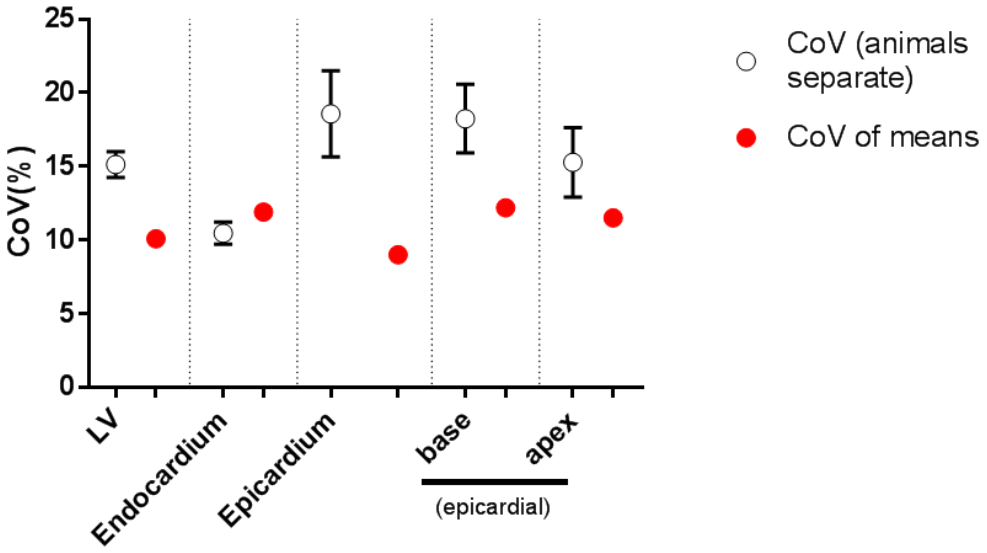

Figure 6.4 Intra-animal variation vs. inter-animal variation Intra-animal variation (open circles) shows the mean variation found within individual cell populations, and inter-animal variation (red circles) show the coefficient of variation of animal means, using the same datasets.

Obtaining large numbers of cells from individual animals allows the accurate assessment of intra-heart variation (Mean variation present within each heart). This is not possible using lower-throughput techniques. Conventionally, the mean of each animal APD_{90} is sampled, and the variation *between means* is used to describe population variation. As shown in Figure 6.4, this both underestimates the heterogeneity present, and additionally causes loss of inter-animal variation: there is no error on the mean.

6.3.2 Region-specific $I_{Ca\text{-}L}$ block using Nifedipine

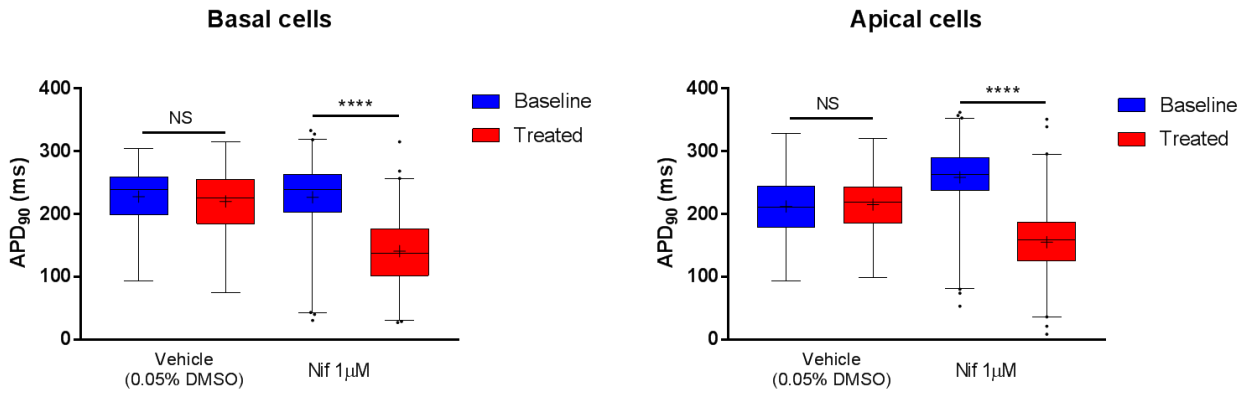

Basal cells (N = 6)		
	Baseline	Nifedipine (1uM)
N	6	6
n	303	302
Mean	227	140.7
S.D.	55.69	54.5
IQR	60.1	74.7
CoV	24.54	38.73

Apical cells (N=6)		
	Baseline	Nifedipine (1uM)
N	6	6
n	308	302
Mean	258.5	155.2
S.D.	46.45	47.99
IQR	52.8	62.1
CoV	17.97	30.92

Figure 6.5 Effect of $I_{Ca\text{-}L}$ block on APD_{90} in sub- endocardium and sub-epicardium. Box plots of APD_{90} in populations of cells sampled from apex and base of the sub-epicardial surface before (baseline) and after treatment with 1 μM nifedipine. Both regions display significant decrease in mean APD_{90} after drug treatment (Paired t-test, P<0.001). Vehicle (DMSO) shows no significant change.

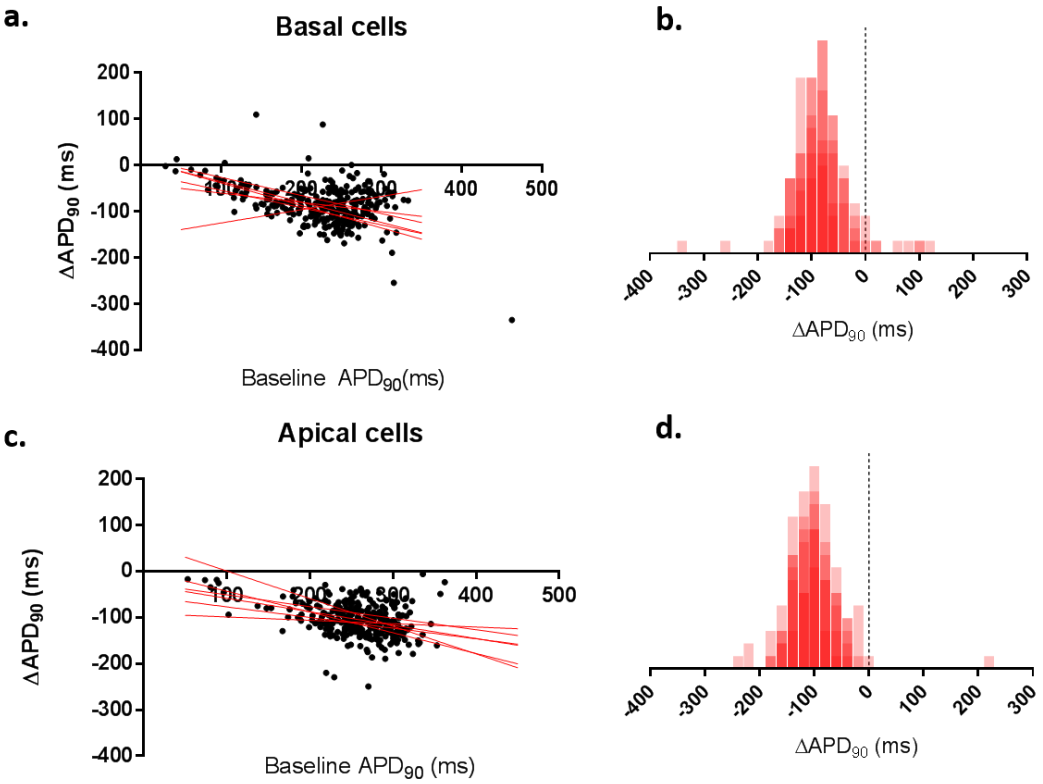

Figure 6.6 Net APD effect of 1 μM nifedipine on APD_{90}. Scatter plot of net drug effect on APD_{90} against baseline APD_{90}. (a) Basal cells. (c) Apical Cells. A linear regression was fitted to each cell population to determine the relationship between starting APD and observed drug effect (red). 5/6 basal cell populations and 6/6 apical cell populations displayed a negative linear correlation with a mean gradient of -0.26x±11 and -0.31x±7, respectively. (b) Overlapping histograms of APD_{90} change after drug in basal cells and (d) apical cells.

Not all cells experienced APD shortening, although the vast majority did. The APD-shortening effect appears to be non-uniform in both regions. The APD-shortening effect was positively correlated with baseline AP duration in 11 out of 12 animals between both basal and apical cells, indicating drug effect was influenced by the initial baseline state of each cell, rather than imposing a constant change across all cells.

6.3.3 Region-specific hERG block using Dofetilide

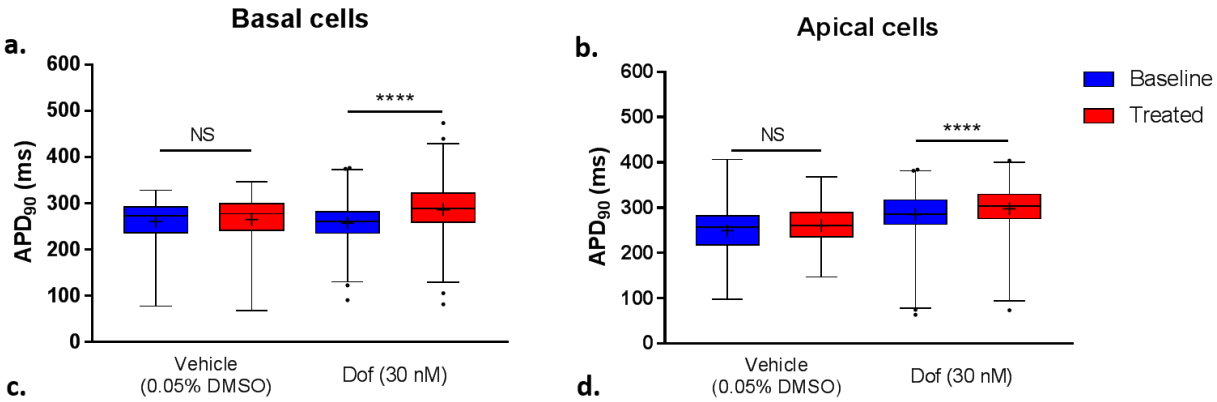

Basal cells	Baseline	Dofetilide (30nM)
N	6	6
n	272	244
Mean	258	283.5
S.D.	40.4	49.0
IQR	46.5	61.6
CoV	15.7	17.5

Apical cells	Baseline	Dofetilide (30nM)
N	6	6
n	256	199
Mean	285	305
S.D.	52.4	45.3
IQR	53.5	51.2
CoV	18.4	15.3

Figure 6.7 Effect of IKr block on APD_{90} in sub- endocardium and sub-epicardium Box plots of APD_{90} in populations of cells sampled from apex and base of the sub-epicardial surface before (baseline) and after treatment with 30 nM dofetilide.

Both regions display significant increase in mean APD_{90} after drug treatment (Paired t-test, $P<0.001$). Vehicle (DMSO) shows no change. Note the APD of cells whose AP prolonged beyond the pacing cycle length (500 ms) could not be quantified. The net APD prolonging effect seen here is therefore likely an under-estimation (discussed in p124).

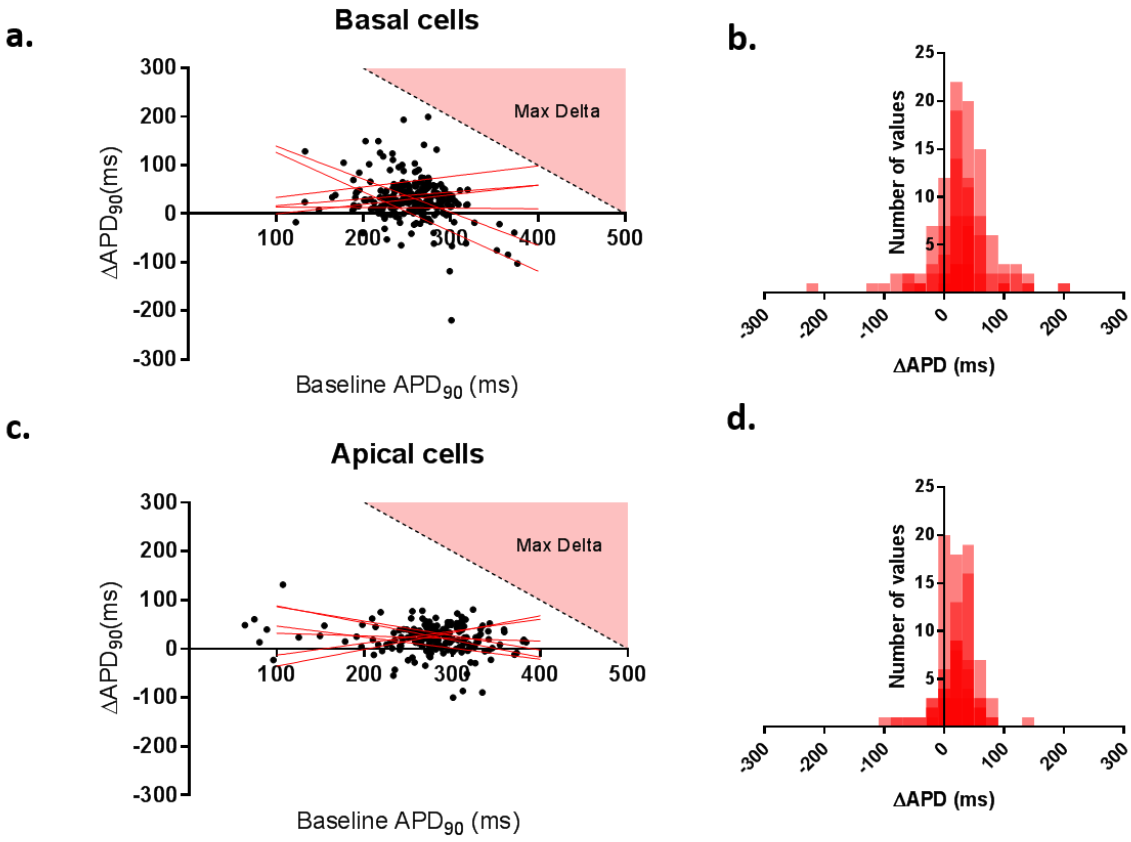

Figure 6.8 Net effect of 30 nm treatment on APD_{90}. Scatter plot of net drug effect on APD_{90} against baseline APD_{90} by individual cells (paired) in response to 30 nM dofetilide. The scatter plots show the theoretical maximum measurable Δ while pacing at 2 Hz (red area). (b) Overlapping histogram of APD_{90} change (paired) after drug in basal cells and (d) apical cells.

The APD-prolonging effect of dofetilide appears to be uniform in both regions. The vast majority of cells (> 85%) experienced AP prolongation following treatment. There was no strong evidence of correlation between baseline and recorded effect on APD, as 6/12 cell populations showed no correlation ($p>0.05$). Of the remaining 6 cell populations with linear regressions significantly deviating from zero, 4 were negative and 2 positive. As discussed later, a proportion of cells (hyper-responders, see Figure 6.9) experienced APD prolongation beyond 500 ms, and their APD could therefore not be measured.

6.3.3.1 Hyper-responders

Following 30 nM dofetilide treatment, mean APD_{90} increased by 30±2ms in basal cells, and by 21±2 ms in apical cells (Paired t-test; P<0.001, respectively). The ΔAPD_{90} (net change following dofetilide) was plotted against baseline APD_{90} to determine whether this effect was uniform across cells. The APD prolongation appeared uniform, and consequently was not dependent on baseline APD. Sub-groups of cells (up to 50%) from each heart region experienced AP prolongation to values beyond the pacing cycle length (>500ms). The mean baseline APD_{90} from these cells was not significantly different from normal-responders (*Base*: 277±9 ms vs. 282±4 ms; *Apex*: 299±5 ms vs. 290±4 ms respectively; Unpaired t-test, P > 0.05).

While the APD_{90} for these hyper-responders could not be determined (APD > CL), we calculated the minimum ΔAPD_{90} they had to have experienced to reach an APD ≥ 500 ms. The ΔAPD_{90} for each cell was calculated as:

$$CL\ (ms) - APD_{90(\text{Baseline})}\ (ms)$$

Using the minimum Δ from the hyper-responders, the mean APD increase in basal and apical cells are calculated to be 55±4 ms and 56±5 ms, compared to 36±3 ms a and 21±4 ms, respectively. This measure of mean prolongation can only serve as a conservative estimate, and we can confidently assert this is the minimum effect observed, and likely to be higher, however the absolute value cannot be inferred from these data alone.

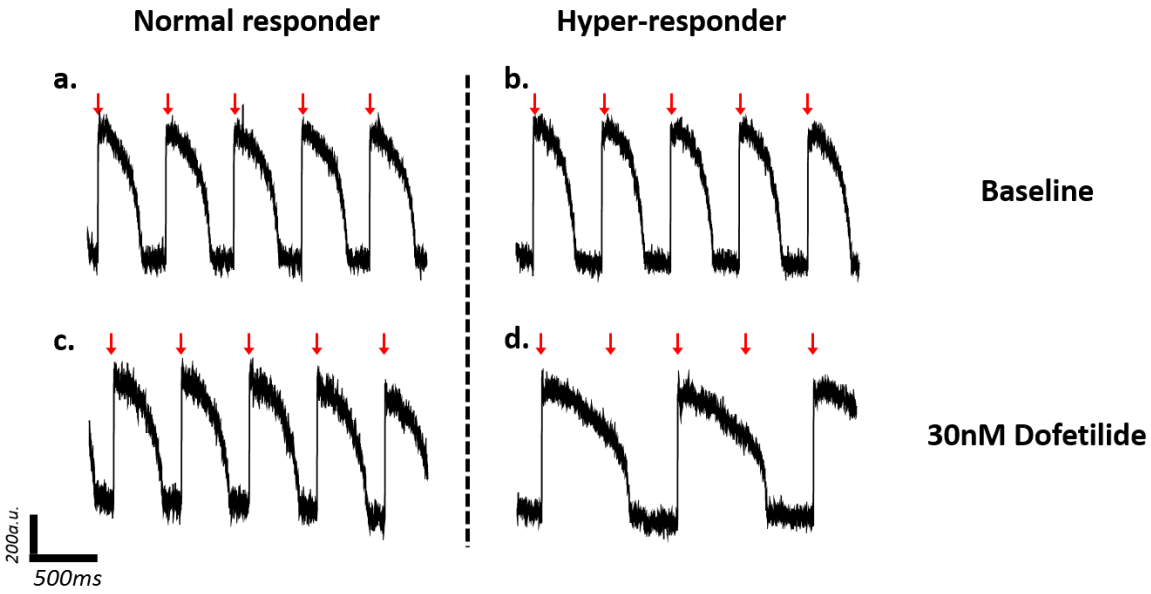

Figure 6.9 Example of a typical responder and a hyper-responding cell AP train. (**a**) Normal and (**b**) hyper-responding cells prior to drug treatment. (**c**) Cell AP train following incubation with 30 nM dofetilide. The pacing stimulus (red arrows) shows when the cell was electrically stimulated. (**d**) The hyper-responder AP exceeded the protocol pacing interval (500ms) and consequently depolarised every second beat (1:2). No EADs were seen in either group.

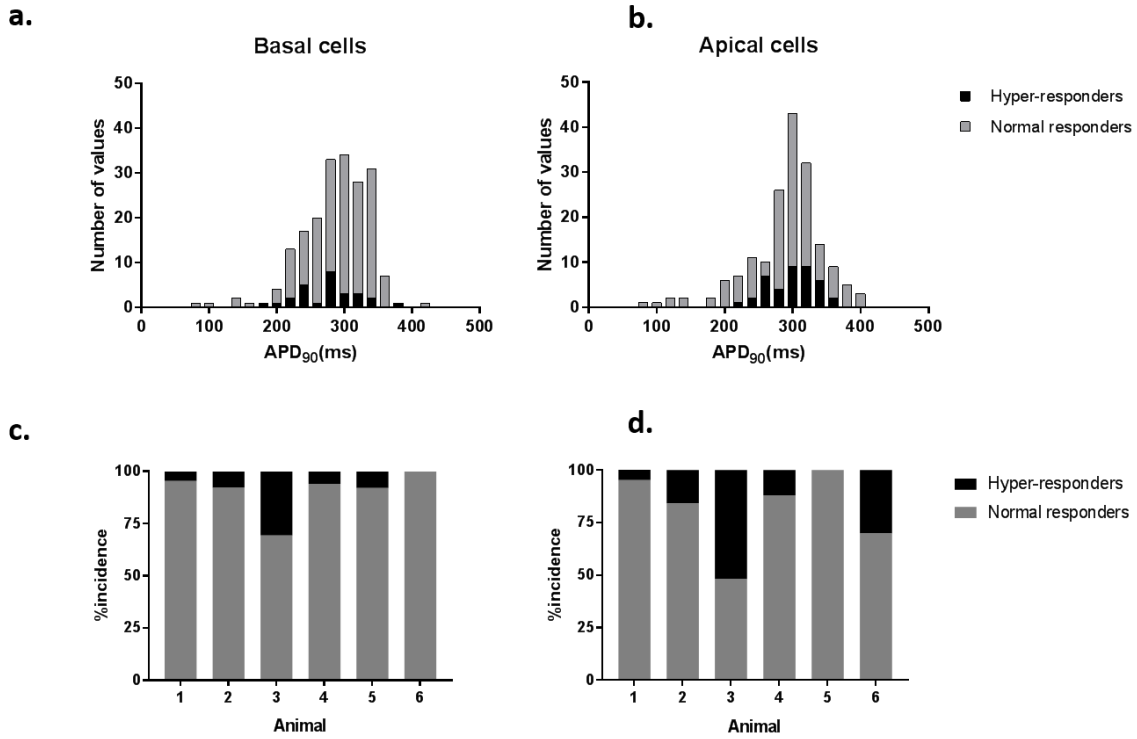

Figure 6.10 Comparison of normo- versus hyper-responding cell baseline AP duration. Normal responders (grey) and hyper-responders (black) are not significantly different (P=0.31 and P=0.051, respectively.) and appear to follow the same distribution pattern.

The percentage incidence of hyper-responders ranged from none to 50% from animal to animal at the same drug concentration.

The incidence of hyper-responders varied considerably between animals, and between regions (see Figure 6.10). The average incidence of hyper-responders in basal cells was 9.5±4%, and 19.2±4% in apical cells.

Conclusions

6.4 Transmural variation

Repolarisation heterogeneity was investigated both along the transmural and longitudinal axes of the rabbit myocardium. Measures of variation used were standard deviation, interquartile range and coefficient of variation. These were selected to complement their respective sensitivity to outliers, giving a better picture of heterogeneity than any individual measure could. Variation was assessed at three levels: (1) within a single region of myocardium, (2) between regions of the same heart and (3) between hearts. The intrinsic variation present in isolated cells is vastly greater than in electrically coupled tissue. Interestingly, the spread of APD_{90} observed in any region of the myocardium, irrespective of its relative size/volume (e.g. basal sub-epicardium), appears to be comparable in repolarisation *heterogeneity* to the whole ventricle in healthy tissue. This suggests different electrophysiological behaviours across the LV wall are exhibited as a mean shift, with comparable spread of cell-specific behaviour, irrespective of the cell's location in the wall.

6.5 APD modulation in epicardial sub-regions

6.5.1 Nifedipine

Using nifedipine to shorten the action potential was done to assess the homogeneity of response on a cell to cell basis. As hypothesized, the net drug effect was not homogeneous among cell populations. Rather than produce an average shortening in APD applicable to all cells, $I_{Ca\text{-}L}$ block produced a graded effect, where cells with "long" APs experienced more pronounced AP shortening than cells with intrinsically "shorter" APs. This effect was significant in 5/6 animals.

Moreover, blocking $I_{Ca\text{-}L}$ should always shorten APD. Interestingly, a very small number of cells from each sample experienced modest AP *prolongation* following drug treatment.

Although cell damage could play a role in this, it is likely to have been caused by APD variation of the second measurement. This requires investigation of repeat-measurement variability over time in a large group of control cells (Time control).

While this effect may be an artefact of intrinsic variation as a result of the technique, current models taking an agnostic approach to experimental dataset calibration are not incorporating this variable (i.e. $I_{Ca\text{-}L}$ block on a modelled cell will *always* cause AP shortening, by definition). Adding measurement noise (time control) when calibrating models using fluorescence-based experiments may improve current models.

6.5.2 Dofetilide

6.5.3 Hyper-responders

Mean APD following hERG blockade was significantly increased, but this was also not homogeneous across the cell populations tested. Following 30 nM dofetilide treatment, the APD response was either moderate and constant (~10% increase from baseline) or extreme (≥80% increase). The striking feature of these latter hyper-responding cells was that their baseline APD was undistinguishable from other cells prior to drug treatment. Lastly, the incidence of these hyper-responders varied between hearts and between apex and base, accounting for up to 50% of the cell populations sampled from individual animals. These differences in the nature of hyper-responders need to be investigated more systematically. Very few cells failed to respond to the drug treatment, with a select few experiencing APD *shortening*. Negative responders could be explained by an excitatory threshold shift in these cells, causing incomplete APs in response to a constant stimulus (very short duration, smaller amplitude positive voltage deflections). A method for testing for this would be to assess the signal-to-noise of each cell prior to and following drug incubation. Any substantial drop in SNR would indicate the amplitude of the pseudo-action potential results from sub-threshold depolarisation and should be discarded.

Experimentally calibrated model populations have been used recently (Britton *et al.*, 2013) to investigate the mechanisms of variation to drug response in Purkinje fibers. Using wide ion channel conductance limits (up to ±100%), they successfully predicted ΔAPD response to dofetilide in Purkinje fibers. Using these experimental constraints, no evidence for bi-modal response to drug was reported. The experimental sets used to calibrate these models consisted of microelectrode recordings of 6 preparations of Purkinje fibers, although the number of animals used is not specified. It is conceivable that cellular coupling in their

preparations could mask measures of variability, and that sample size contributed negatively to estimates of variation derived from these experiments. Using large sample sizes from several animals could therefore contribute to improving estimates of variation.

Chapter 7 General Discussion

7.1 Summary

The work carried out as part of this thesis was organised into two discrete results categories. The first was the successful leap from low to medium-throughput sampling of simultaneous voltage and calcium information from large sample populations of isolated cells (CMs) from a single animal. The second was the implementation of this new technique to investigate the scale and implications of biological variation on a cell to cell basis following MI, and additionally specific channel blockade using cell populations from small cardiac subregions.

7.2 Electrophysiological findings

The application of a medium-throughput technique allowed the first quantification of heterogeneity on cell populations within the ventricle wall, in healthy animals, and following myocardial infarction. Interestingly, the variation in repolarisation in any given region of the ventricle was found to be considerable, and far outweighed any differences found between discrete regions. This large variation did not limit the ability of the technique to identify small electrophysiological differences due to large sample sizes. This finding strongly suggests that variation in conductance of key ion channels may currently be underestimated by electrophysiological models (Britton *et al.*, 2013), and should be incorporated in current models to better estimate drug response across populations. As mentioned previously, experimentally calibrated model populations have potentially suffered from inconsistent reports of cell-cell and heart-heart variation, where cell groups from multiple hearts were pooled, inadvertently combining inter- and intra-heart variation. Incorporating medium/high-throughput experiments consequently has the potential to improve the predictive power of current models, and additionally by providing a measure of inter-, as well as intra-subject variability.

Following infarction-induced remodelling over several weeks, mean action potential prolongation was observed at slow frequencies (1 Hz and 2 Hz), but was not present at 3 Hz. Heterogeneity between cells was, however, not found to increase significantly in any of the voltage parameters measured. Variation in repolarisation duration between MI animals did not increase significantly between MI and controls, which could reflect a variable response to injury from animal to animal. The relatively small number of animals used could not substantiate this finding (N = 7-9), however it is plausible a small change in cell-cell variation exists, which the study was insufficiently powered to detect. Lastly, the pacing rate

of 2 Hz used throughout may have masked heterogeneity, which could be revealed at slower rates.

Transmural analysis of individual heart electrophysiology following infarction found a loss of the transmural APD gradient, whereby infarcted left ventricles produced sub-endocardial and sub-epicardial cells with prolonged repolarisation durations, blurring the boundary between regions. While action potential duration was significantly increased in both sub endocardial and sub-epicardial cells, the increase was greater in the sub-epicardium. Triangulation, normalised to action potential duration, was not different between regions or following MI, suggesting reports of increased triangulation in literature may in part be positively skewed by comparing APs of different durations. Region-specific remodelling has been reported previously (McIntosh, Cobbe and Smith, 2000; Lou, Li and Efimov, 2011).

Heterogeneity was not found to increase between regions, save for a modest increase in triangulation CoV of the sub-endocardium in MI animals. The AP upstroke was the most variable parameter assessed, attributable to both its sensitivity to Na+ channel variation, as well as measurement error (i.e. millisecond event resolution is at the lower limit of current technique precision).

While no significant difference was found in measures of APD heterogeneity between healthy regions of infarcted and sham animals, a trend increase in variation is visible in the cell populations (all animals pooled). As mentioned, the infarct and peri-infarct tissue were removed in both groups. This served as a robust comparison between remodelled and non-remodelled tissue, but may also give an incomplete representation of variability present in MI. This finding does however support the idea that the cause of increased arrhythmic risk following MI stems from a localised mean change in APD (i.e. loss of transmural gradient) rather than increased heterogeneity in the non-infarcted regions of remodelled myocardium. Inclusion of peri-infarct cells may tell a different story.

7.3 Cell population response to channel block

The action potential duration was modulated through $I_{Ca\text{-}L}$ and I_{Kr} blockade in left-ventricular subregions. The behaviour of cell populations from both regions studied was not homogeneous in response to either prolongation or shortening of the APD. Blockade of L-type Ca^{2+} channels produced a baseline-dependent AP shortening, whereby 80% of animals tested displayed a linear correlation between drug effect and baseline state in paired cells. Blocking I_{Kr} produced moderate APD prolongation in the majority of cells, and revealed a sub-population of cells exhibiting extreme APD prolongation. The type of response was not predictable from baseline APD.

The probable reason for the baseline-dependence of L-type Ca^{2+} blockade, where cells with short APs show the smallest degree of APD shortening, is that these cells have smaller calcium transients. The consequences of having smaller calcium transients are a reduced calcium transient amplitude, which directly translates to reduced fractional shortening. In turn, cells with larger transients can respond more variably to $I_{Ca\text{-}L}$ block, denoted by a wider range of ΔAPD_{90} toward the longer range of baselines than at the short range (Figure 6.6). Future work should aim to compare calcium transient duration and amplitude together with APD and fractional shortening in response to pharmacological intervention.

Contrasting the above, hERG blockade using dofetilide did not produce baseline dependent APD prolongation. The highly variable spread of ΔAPD_{90} in response to treatment suggests a large physiological range of hERG expression in cardiomyocytes, irrespective of their APD. A curious feature was the sub-group of "hyper-responding" cells with a very different response, despite having the same baseline as normal responders. The reason behind this sub-population is not known. A possible mechanism is that cells with large hERG expression also have small $I_{Ca\text{-}L}$ expression, which would result in comparable APD at rest, but disproportionate APD prolongation in response to I_{Kr} block. Under these conditions, similar fractional inhibition of hERG could produce disparate effects on APD. The Sobie group found increasing IKs in several computational models increased heterogeneity in CM populations. They also tested IKs contribution to EAD propensity in models with a wide range of $I_{Ca\text{-}L}$ expression, and found high levels of IKs was protective against EAD generation.

To test this hypothesis, comparing calcium transients and fractional shortening with APD in these two cell groups is a necessity. Another approach to testing this is using computational

modelling to simulate the response of a population of cells with a wide range of ion channel expression to an identical fractional inhibition of IKr. This will test whether this behaviour is simply a product of the inherent variability present in isolated cell ion channel expression. In the event that hyper-responding cells are in fact physiological, then what contribution this sub-population makes to the overall response to hERG block needs to be investigated. Finally, in pathology, after remodelling of the myocardium, the range of electrophysiological phenotypes may have been altered, potentially also affecting hyper-responding cells.

7.4 Inter-heart and intra-heart variation in APD

The technique used in this permitted large groups of cells to be sampled from individual hearts, quantifying variation (SD, CoV) accurately. In this way it became possible to study the magnitude of variation present between normal and pathological conditions caused by MI. Furthermore, it also allowed inter-heart and intra-heart variation to be assessed separately.

Isolated cell publications commonly mix these two variables and report mixed SEM and SD values. Table 5 summarises and contrasts some of the literature on rabbit APD in single cell and intact myocardium. The latter includes detailed optical measurements from a current unpublished study (C. Alexander, personal communication, see Table 5).

Single cell data from endocardial and epicardial sites suggests an intra-heart APD CoV of 15-20%. Based on the mean APD from each animal, the inter-heart APD was ~10%. These numbers span the estimates of CoV based on published data (Table 5). The CoV from the combined data (all cells from all animals as is conventionally done) is approximately 15%.

This compares with data from the intact myocardium which suggests that intra-heart variation is considerably less than that seen in single cells. The variation from region to region in each heart is approximately 3-4%, (i.e. ~20% of that seen in single cells). This reduced variation is due to the electrical coupling between cells, which minimises differences. The inter-heart differences are approximately the same value. The smaller spread may also be due to lower APD values in intact hearts at equivalent rates (i.e. ~170 ms vs ~270 ms at 2Hz).

Combining the CoV from intra-heart and inter-heart variation, to predict the global CoV value is complex. Estimates of the predicted value were based on modelling theoretical values using random variation of APD values. The relationship between the two is shown in the appendix (Table 6). These indicate that for an intra-heart CoV of ~10%, and an inter-heart of ~15%, the global CoV will be ~18.5%, which closely matches the value of 18.4% measured in this study. Interestingly, the relationship between inter- and intra-heart variation shows that the very small CoV observed within intact hearts would mean that global (all cells pooled) CoV is dominated by the inter-heart variation rather than the intra-heart CoV. In contrast to studies in single cells. This strongly suggests a hierarchical statistical approach is essential for analysis of these data, as advised in a recent publication (Sikkel *et al.*, 2017).

		Source	Heart region	Pacing frequency (Hz)	Mean APD_{90}(ms)	CoV (INTRA)	CoV (INTER)	Compound CoV	Predicted variation
Rabbit	*Isolated cell*	*(de Groot et al., 2003)*	Whole LV	2	235		--	**23.4 %**	
		(McIntosh, Cobbe and Smith, 2000)	sub-endocardium	1	220		15.7 %	**--**	
				2	210		16.5 %	**--**	
			sub-epicardium	1	170		15.4 %	**--**	
				2	175		15.0 %	**--**	
		(Saegusa, Garg and Spitzer, 2013)	Sub-epicardium	0.5	414		--	**13.5 %**	
		(Wei et al., 2012)	Whole LV	1	215		--	**13.7 %**	
		Q. Lachaud	LV	2	268	15.3 %	10.1 %	**18.4 %**	~18.5 %
			Sub-endocardium	2	259	12.2%	11.9 %	**14.5 %**	~16.8 %
			Sub-epicardium	2	246	17.7 %	9.0%	**15.6 %**	~20.0 %
			Epicardial base	2	244	18.2 %	12.2 %	**21.7 %**	~21.7 %
			Epicardial apex	2	266	15.3 %	11.5 %	**19.5 %**	~19.2 %
	Coupled tissue	*(Myles et al., 2010)*	Endocardium	2.86	152		--	**8.0 %**	
			Epicardium	2.86	165		--	**6.1 %**	
		(Idriss and Wolf, 2004)	Endocardium (wedge)	1	190	**2.6 %**	--	**--**	
				2	177	**4.2 %**	--	**--**	
			Epicardium (wedge)	1	160	**3.1 %**	--	**--**	
				2	156	**4.7 %**	--	**--**	
		(Kettlewell, 2002)	Whole heart	2.86	120	**7.6 %**	--	**--**	
				2.2	130	**7.3 %**	--	**--**	
		(Wei et al., 2012)	LV wedge	1	216	**2.3 %**	--	**--**	
		C. Alexander*	LV (Epicardium)	2	167	**3.3 %**	7.8 %	**7.8 %**	~8 %
Human	Isolated cell	*(Coppini et al., 2013)*	Whole LV	1	350	**--**	--	**35.7 %**	
	Tissue	*(de Groot et al., 2003)*	wedge LV	0.5	383	**--**	--	**12.3 %**	
		(Koller et al., 2005)	endocardium	1.6	270	**--**	--	**9.0 %**	
		(Koncz et al., 2011)	Epicardium tissue	1	243	**--**	--	**15.8 %**	

Table 5 Literature reports of APD_{90} variation in isolated cells and coupled tissue
**Personal communication*

7.5 Technique achievements, limitations and improvements

The methodology developed in this thesis is now capable of recording transient changes in membrane voltage, calcium concentration, and contraction kinetics in large populations of isolated cells from single animals. The novel aspect of this method over available commercial technology is a combination of elements: (1) a highly sensitive, high sampling rate fluorescence-recording apparatus, (2) a custom-built microscope stage incubator/stimulator combined with a bright fluorophore and (3) a proprietary, flexible software platform controlling the hardware, and providing user-controlled, tailored trace analysis. The combination of these main components constitutes a significant improvement on the methodologies used prior in the field of fluorescence-based electrophysiology, by improving signal sensitivity, temporal resolution, increasing experimental throughput, and coincidentally reducing animal usage.

The current limitations of this method involve spectral overlap of the various dyes used, and concomitant limitations with regards of wavelength bands which can be sampled from simultaneously without requiring changes in hardware, such as wavelength filters or excitation sources. The top-end sampling limits of the system, while comparatively very high, have been identified and optimised to increase recording consistency and repeatability, specifically pertaining to very fast events like the action potential upstroke. In other words, the upstroke of the action potential is still challenging to accurately measure. Using consistent filtering techniques helped make comparative measurements, but accurately quantifying the absolute duration of the upstroke still requires faster sampling rates.

The next logical step for this technique is automating the last aspect of human involvement. Visually inspecting cell health and manually enclosing the FOV onto individual cells is the most time-consuming and subjective step of the protocol. Removing this step has the potential to increase the throughput of the technique a further 3 to 10-fold. A possible workaround for this is a systematic recording of all cells identifiable in the dish using lower magnification (x5-x10) and image analysis to identify isolated cell locations and map them. Once the isolated cell positions are recorded, CellOPTIQ could then systematically record all available metrics (action potentials, calcium transients, contraction kinetics, cell size) in all cells and a *post hoc* quality assessment can be carried out by a human.

Conversely, at the expense of sampling rate, a CCD camera could be used to record fluorescence continuously from a large FOV, and fluorescence analysis can be carried out *post hoc*.

7.5.1 Future work

The next steps in the development of this powerful technique can be divided in two parts: (i) further improving the sampling throughput from single hearts, by automating cell targeting and (ii) integrating isolated cell experiments with whole heart studies. Improving throughput is currently limited by human input. Using live image analysis could allow the identification of viable cells automatically in the dish, and the systematic recording of fluorescent signals. Pairing medium throughput cell studies with whole heart or wedge experiments would enable pairing whole organ information (ECG, epicardial and transmural APD dispersion) with isolated cell information (region-specific Ca^{2+} and voltage information). A further step would be to pair functional (contraction, voltage and calcium) measurements with protein assessment of individual cells which could yield further insight into the relationship between ion channel expression ratios and APD heterogeneity between cells and individuals.

Appendix

8.1 Trace deconvolution Python 3 code

```
import numpy as np
from matplotlib import pyplot as plt
import glob
import os

home = 'C:/Users/Quentin Lachaud/Desktop/Deconvolution_traces/'

#Define correlation function variables:
factor2 = 0.5
factor1 = 0.09
constant1 = 278
constant2 = 354

#define corrective function
def correct(AP,Ca,factor,constant):

    corr = Ca-(AP * factor + constant)
    return corr

#look in each channel folder for csv files
ca1 = glob.glob(home + 'Ch1/*.csv')
ca2 = glob.glob(home + 'ch2/*.csv')
V1 = glob.glob(home+ 'ch4/*.csv')

#assign channel to array from files
for i in range(len(ca1)):
    ch1 = np.loadtxt(ca1[i], delimiter = ',')
    ch2 = np.loadtxt(ca2[i], delimiter = ',')
    ch4 = np.loadtxt(V1[i], delimiter = ',')

#correct each channel and remove non-overlapping timeseries to calculate ratios
    ratio = ch1[:,1]/ch2[:,1]
    corr1 = correct(ch4[2:,1],ch1[1:-1,1],factor1, constant1)
    corr2 = correct(ch4[2:,1],ch2[:-2,1],factor2, constant2)
    corr_ratio = corr1/corr2

#Create corrected ratio folder and analysis folder
    ratio_folder_path = home + 'ratio/'
    corr_folder_path = home +'corr_ratio/'
    corr_analysis = home + 'ratio_analysis/'
    if not os.path.exists(ratio_folder_path):
        os.makedirs(ratio_folder_path)
    if not os.path.exists(corr_folder_path):
        os.makedirs(corr_folder_path)
    if not os.path.exists(corr_analysis):
        os.makedirs(corr_analysis)

#Save corrected ratios to new folder
    np.savetxt(ratio_folder_path + 'ratio'+str(i)+'.csv', ratio)
    np.savetxt(corr_folder_path +'ratio'+str(i)+'.csv', corr_ratio)

#look inside corrected ratios folder and load their data into "trace" to plot
sequentially
corrected_ratios = glob.glob(corr_folder_path + '*.csv')
ratios = glob.glob(ratio_folder_path + '*.csv')


for i in range(len(corrected_ratios)):
    corr_trace = np.loadtxt(corrected_ratios[2])
    old_trace = np.loadtxt(ratios[2])

#make comparative figures side by side
    plt.subplot(1,2,1)
```

```
    plt.title('Original Ratio')
    plt.plot(old_trace, 'b', linewidth = 1)

    plt.subplot(1,2,2)
    plt.title('Corrected Ratio')
    plt.plot(corr_trace, 'red', linewidth = 1)

#plt.show()
```

8.2 Hierarchical analysis using R

The following code and use instructions were taken from Sikkel *et al.*, 2017. The script was adjusted to an example file analysed in this thesis.

```
library(lmerTest) #If told 'there is no package called 'lmerTest', run 'install
.packages("lmerTest")'

## Loading required package: lme4

## Loading required package: Matrix

##
## Attaching package: 'lmerTest'

## The following object is masked from 'package:lme4':
##
##     lmer

## The following object is masked from 'package:stats':
##
##     step

require(readxl) #If told 'there is no package called 'readxl', run 'install.pac
kages("readxl")'

## Loading required package: readxl
```

This prevents scientific notation for p values unless they are very small.

```
options(scipen=999)
```

Now we load the excel spreadsheet into the variable 'input data'.

```
file_location = "C:\\Users\\Quentin Lachaud\\Desktop\\PhD\\R scripts for hierar
chical stats\\Hierarchical MI_APD90.xlsx"
input_data <- read_excel(file_location)
#This loads the excel spreadsheet into the variable 'input data'
```

Here we rename the column of our condition (e.g. heart failure or not) to 'Condition', and the grouping variable (e.g. rat) to 'Group'.

We then ensure that the condition and group columns are treated as categorical variables (factors) rather than a continuous numerical value.

Finally, we create an empty results table.

```
names(input_data)[1] <- "Rabbit"
names(input_data)[2] <- "Region"

input_data[2] <- as.factor(unlist(input_data[2])) #Ensure the Condition group i
```

```
s treated as a categorical variable (distrinct groups) rather than continuous n
umerical values
input_data$Rabbit <- factor(input_data$Rabbit) #Ensure the Rat group (Group) is
treated as a categorical variable (distrinct groups) rather than continuous num
erical values

df_output <- data.frame() #Create an empty main results table
df_output_lsmeans <- data.frame() #Create an empty results table for least squa
red means
df_output_pairwise <- data.frame() #Create an empty results table for the pairw
ay comparisons
```

This is the main 'loop' of the code, which runs once for each dependent variable in our spreadsheet.

```
for(APD90 in names(input_data[,3:ncol(input_data)])) { #This for loop ensures t
he indented code between the curly braces runs once for each column (dependent
variable) from the 3rd column onwards
  # STEP 1. Fit a NON-Hierarchical model (equivalent to a t-test)
  #Fit a model, calculate the standard error, p value, and -2 log Likelihood
  NON_hierarchical_model <- glm(get(APD90) ~ Region, data=input_data) #This fit
s a generlised linear model for each dependent variable and the output column (
HF_or_control; the presence or not of heart failure) and stores it in the varia
ble named NON_hierarchical_model
  se_NON_hierarchical_model <- summary(NON_hierarchical_model)$coefficients[, 2
][1] #This extracts the standard errors from the model and stores it in a new v
ariable named se_NON_hierarchical_model
  p_NON_hierarchical_model <- summary(NON_hierarchical_model)$coefficients[, 4]
[1] #This extracts the standard errors from the model and stores it in a new va
riable named p_NON_hierarchical_model
  goodness_of_fit_NON_hierarchical_model <- logLik(NON_hierarchical_model)*-2 #
We calculate a goodness of fit using the -2 logLikelihood of the model and save
it in a new variable named goodness_of_fit_NON_hierarchical_model

  # STEP 2. Fit a Hierachical model
  # Step 2a. Fit a model, calculate the standard error, p value and -2 log Like
lihood
  hierarchical_model <- lmer(get(APD90) ~ Region + (1 + Region|Rabbit), REML=FA
LSE ,data=input_data) #We now fit a linear mixed effects (hierarchical) model a
nd store that in the variable named hierarchical_model. We fit each dependent v
ariable against the Output column, with 'Rat' as a group effect
  se_hierarchical_model <- summary(hierarchical_model)$coefficients[, 2][1] #As
previously, extract the standard errors and store them in a variable
  p_hierarchical_model <- summary(hierarchical_model)$coefficients[ ,5][1] #As
previously, extract the p values and store them in a variable
  goodness_of_fit_hierarchical_model <- logLik(hierarchical_model)*-2 #As previ
ously, calculate a goodness of fit and store it in a variable

  # STEP 2b. Calculate amount of clustering, defined as the intraclass correlat
ion, a value between 0 and 1
  table_of_variances <- as.data.frame(VarCorr(hierarchical_model)) #Create a da
taframe (table) of the covariance parameters called 'table_of_variances'
  variance_of_means <- table_of_variances$vcov[2] #Extract the variance of the
mean from the 'table_of_variances' and store it in a variable names 'variance_o
f_means'
  variance_of_individual_datapoints <- (table_of_variances$vcov[2] + table_of_v
ariances$vcov[1]) #The total variance is also extracted, as defined as the vari
ance of the rat model plus the residual variance
  icc <- variance_of_means / variance_of_individual_datapoints #The intra-class
correlation (ICC) is calculated and defined by the variance of the model divide
d by the total variance

  # STEP 2c. Calculate goodness of fit and see if higher for hierarchical model
  improvement_in_goodness_of_fit <- goodness_of_fit_NON_hierarchical_model - go
```

```
odness_of_fit_hierarchical_model #We calculate the difference between thepreviously-calculated goodness of fit for both the non-hierarchical and hierrachical models; this difference is stored in the variable improvement_in_goodness_of_fit
  betterfit <- 1-pchisq(improvement_in_goodness_of_fit[2],df=1) #The p value for whether the hierarchical model is a significant improvement is calculated using the Chi-squared distribution with 1 degree of freedom
  p_betterfit <- ifelse(betterfit<0.0001,"<0.0001",round(betterfit,digits=4)) #If the p value calculated above is very small, we just replace it with "<0.0001"
  superiorp <- ifelse(improvement_in_goodness_of_fit>0 & betterfit < 0.05,paste("Y (", p_betterfit ,")",sep=""),paste("N (", betterfit, ")",sep="")) #If there is an improvement in the goodness of fit and the p value is less than <0.05, we set the variable 'superiorp' to "Y", otherwise "N"

  # STEP 3 Calculate least squares means for each group of the outcome variables, and the pairwise comparisons
  lsmean <- lsmeansLT(hierarchical_model) #We calculate the least squares means, standard errors and confidence intervals for the different outcomes (e.g. presence and absense of heart failure)
  row.names(lsmean) <- paste(APD90,row.names(lsmean),sep=" - ") #Add the current variable in question to the row name
  difflsmean <- difflsmeans(hierarchical_model) #We test for significance between the different outcome levels
  row.names(difflsmean) <- paste(APD90,row.names(difflsmean),sep=" - ") #Add the current variable in question to the row name

  df_output <- rbind( #We add the results to our main results table in this function
    df_output,
    data.frame(
      CommonSE=round(se_NON_hierarchical_model,digits=3), #Add the standard error of the non-hierarchical model
      Commonp=ifelse(p_NON_hierarchical_model<0.0001,"< 0.0001",toString(round(p_NON_hierarchical_model,digits=4))), #Add the p value of the non-hierarchical model; if it's very small, replace it with "< 0.0001""
      ICC=paste(round(icc*100,digits=1),"%",sep=""), #Add the intraclass correlation of the hierarchical model
      MixedSE=round(se_hierarchical_model,digits=3), #Add the standard error of the hierarchical model
      Mixedp=ifelse(p_hierarchical_model<0.0001,"< 0.0001",toString(round(p_hierarchical_model,digits=4))), #Add the p value of the hierarchical model; if it's very small, replace it with "< 0.0001""
      Superioryn=superiorp #Add a column indicating if the hierarchical model is a statistically significantly better fit (Y or N) and the actual p value
    )
  )

  df_output_lsmeans <- rbind( #We add the results to our ls squares results table in this function
    df_output_lsmeans,
    lsmean
  )

  df_output_pairwise <- rbind( #We add the results to our pairwise comparisons results table in this function
    df_output_pairwise,
    difflsmean
  )

  row.names(df_output)[nrow(df_output)] <- APD90 #Set the name of the row to th
```

```
e dependent variable in questions
}
```

Finally, we specify the column headings here and print the table.

```
names(df_output) = c("Common test (SE)","Common test (p)","Group-level clusteri
ng (ICC)","Group-level (SE)","Group-level (p)","Superior fit (p)") #Set the col
umn headings
print(df_output) #Output the summary table
```

Here we output a table containing the least squares means and confidence intervals for each outcome, grouped by each dependent variable.

```
cols.dont.want <- c("DF", "t-value", "p-value")
df_output_lsmeans <- df_output_lsmeans[, ! names(df_output_lsmeans) %in% cols.d
ont.want, drop = F]
print(df_output_lsmeans) #Output the results table for LS means
```

Here we output the pairwise comparisons. P values are multiplied by the number of comparisons to maintain a type 1 error rate of 5% (Bonferroni correction) The results are rabbited for each output variable (left column), with each combination of outcomes undergoing significance testing.

```
cols.dont.want <- c("DF", "t-value", "Lower CI","Upper CI")
df_output_pairwise <- df_output_pairwise[, ! names(df_output_pairwise) %in% col
s.dont.want, drop = F] #Remove the unwanted headings from the table
df_output_pairwise$`p-value` <- df_output_pairwise$`Pr(>|t|)` * ( nrow(df_outpu
t_pairwise) / length(names(input_data[,3:ncol(input_data)])) ) #Multiply the p
values by the number of comparisons per dependent variable
names(df_output_pairwise)[names(df_output_pairwise)=="p-value"] <- "Bonferroni
p-value" #Change the column heading
df_output_pairwise[df_output_pairwise$`Bonferroni p-value` > 1,"Bonferroni p-va
lue"] <- 1 #Change any p value above 1 to 1
print(df_output_pairwise) #Output the results table for the pairwise comparison
s
```

Intra-heart CoV	Inter-heart CoV (%)																							
	2	3	4	5	6	7	8	9	10	11	12	13	14	15	16	17	18	19	20	21	22	23	24	25
2	2.8	3.6	4.5	5.4	6.3	7.3	8.2	9.2	10.2	11.2	12.2	13.1	14.1	15.1	16.1	17.1	18.1	19.1	20.1	21.1	22.1	23.1	24.1	25.1
3	3.6	4.2	5	5.8	6.7	7.6	8.5	9.5	10.4	11.4	12.4	13.3	14.3	15.3	16.3	17.2	18.2	19.2	20.2	21.2	22.2	23.2	24.2	25.2
4	4.5	5	5.7	6.4	7.2	8.1	8.9	9.8	10.8	11.7	12.6	13.6	14.6	15.5	16.5	17.4	18.4	19.4	20.4	21.4	22.3	23.3	24.4	25.3
5	5.4	5.8	6.3	7	7.8	8.6	9.4	10.3	11.2	12.1	13	13.9	14.9	15.8	16.8	17.7	18.7	19.7	20.6	21.6	22.5	23.6	24.5	25.5
6	6.4	6.7	7.1	7.8	8.5	9.2	10	10.8	11.7	12.5	13.4	14.3	15.3	16.2	17.1	18	19	19.9	20.8	21.8	22.8	23.8	24.7	25.7
7	7.2	7.6	8.1	8.6	9.2	9.9	10.6	11.4	12.2	13.1	13.9	14.7	15.6	16.5	17.5	18.3	19.3	20.2	21.2	22.1	23.1	24	25	26
8	8.3	8.4	8.8	9.3	9.9	10.6	11.2	12	12.8	13.7	14.4	15.3	16.1	17	17.8	18.7	19.7	20.6	21.5	22.5	23.4	24.4	25.3	26.3
9	9.2	9.4	9.9	10.2	10.9	11.4	12.1	12.7	13.4	14.1	15	15.8	16.6	17.5	18.3	19.2	20.1	21	21.9	22.8	23.7	24.7	25.6	26.6
10	10.2	10.4	10.7	11.1	11.5	12.1	12.8	13.4	14.1	14.9	15.5	16.4	17.2	17.9	18.9	19.7	20.5	21.5	22.4	23.2	24.1	25.1	26	26.9
11	11.2	11.4	11.7	12	12.4	13	13.6	14.1	14.9	15.5	16.2	17.1	17.8	18.5	19.4	20.3	21	22	22.7	23.7	24.6	25.6	26.5	27.3
12	12.1	12.3	12.6	12.9	13.3	13.8	14.4	15	15.6	16.3	16.9	17.6	18.4	19.2	20	20.8	21.5	22.5	23.3	24.3	25	25.8	26.9	27.7
13	13	13.3	13.5	13.9	14.4	14.8	15.3	15.8	16.4	16.9	17.7	18.3	19	19.9	20.7	21.3	22.2	23	23.8	24.6	25.5	26.4	27.3	28.2
14	13.9	14.2	14.5	14.8	15.2	15.7	16.1	16.6	17.1	17.8	18.4	19.1	19.8	20.4	21.1	21.9	22.8	23.7	24.4	25.2	26.2	26.9	27.7	28.6
15	15.1	15.3	15.3	15.9	16	16.5	17.1	17.3	18	18.6	19	19.7	20.3	21.2	21.9	22.5	23.4	24.1	24.9	25.7	26.5	27.4	28.2	29
16	16.2	16.2	16.4	16.7	17	17.4	17.8	18.1	18.9	19.2	20	20.5	21.1	21.9	22.6	23.4	24	24.8	25.5	26.3	27.2	28.1	28.7	29.6
17	17.1	17.1	17.5	17.5	18	18.5	18.7	19.1	19.5	20.3	20.7	21.5	21.9	22.6	23.2	23.8	24.6	25.4	26.2	27	27.8	28.6	29.4	30.3
18	18	18	18.3	18.6	19	19.3	19.7	20	20.5	20.9	21.5	22.1	22.6	23.2	24	24.9	25.3	26.2	26.9	27.8	28.4	29.2	29.8	30.7
19	18.9	19	19.3	19.5	19.8	20.2	20.5	21	21.6	21.7	22.5	22.9	23.9	24.1	24.7	25.3	26	26.7	27.4	28.3	29.1	29.7	30.5	31.5
20	19.8	20	20.2	20.6	20.6	21	21.3	22	22.3	22.5	23.3	23.9	24.3	24.8	25.5	26.2	26.9	27.5	28.3	29	29.6	30.4	31.1	32
21	21.3	21.1	21.3	21.5	21.8	22.1	22.4	22.7	23.2	23.4	24.2	24.3	25.2	25.7	26.2	27	27.6	28.3	28.8	29.8	30.5	31.2	32	32.6
22	22	22.1	22.1	22.6	22.6	22.9	23.3	23.5	24.1	24.9	24.9	25.4	26.2	26.5	27.2	27.8	28.3	29	29.7	30.3	30.9	31.8	32.5	33.2
23	23	23	23.2	23.3	23.4	24	24.5	24.7	25.2	25.6	26	26.4	26.9	27.4	28	28.5	29	29.7	30.9	31	31.9	32.6	33	33.8
24	24.2	24.1	24.2	24.3	24.5	24.9	25.2	25.6	25.7	26.3	26.7	27.3	27.4	28.1	28.7	29.3	30.1	30.6	30.9	31.8	32.4	33.2	33.9	34.9
25	25	25.1	25	25.4	25.4	25.8	26.4	26.5	26.8	27.8	27.6	28	28.4	29.1	29.5	30.2	30.8	31.5	31.7	32.6	33	34	34.3	35.2

Table 6 Modelled predicted influence of intra- versus inter- animal variation on compound CoV of cell population
Modelled relationship between inter- and intra-animal variation relative to compound variation of mean APD_{90}. This table shows the modelled compound CoV is always less than the sum of inter + intra CoVs.

References

Akar, F. G. and Rosenbaum, D. S. (2003) 'Transmural electrophysiological heterogeneities underlying arrhythmogenesis in heart failure.', *Circulation research*, 93(7), pp. 638–45. doi: 10.1161/01.RES.0000092248.59479.AE.

Al-khatib, S. M. *et al.* (2017) 'Guideline for managment of patients with ventricular arrhythmias and the prevention of sudden cardiac death', *To appear in JACC*. doi: 10.1016/j.jacc.2017.10.054.This.

Allingham, J. S., Smith, R. and Rayment, I. (2005) 'The structural basis of blebbistatin inhibition and specificity for myosin II', *Nature Structural and Molecular Biology*, 12(4), pp. 378–379. doi: 10.1038/nsmb908.

Anderson, J. L. and Prystowsky, E. N. (1999) 'Sotalol: An important new antiarrhythmic', *American Heart Journal*, 137(3), pp. 388–409. doi: 10.1016/S0002-8703(99)70484-9.

Antzelevitch, C. *et al.* (1991) 'Heterogeneity within the ventricular wall. Electrophysiology and pharmacology', *Circulation Research*, 69, pp. 1427–1449.

Antzelevitch, C. *et al.* (1999) 'The M cell: its contribution to the ECG and to normal and abnormal electrical function of the heart.', *Journal of cardiovascular electrophysiology*, 10(8), pp. 1124–52. Available at: http://www.ncbi.nlm.nih.gov/pubmed/10466495 (Accessed: 28 May 2019).

Antzelevitch, C. (2007) 'Heterogeneity and cardiac arrhythmias: An overview', *Heart Rhythm*. Elsevier, 4(7), pp. 964–972. doi: 10.1016/j.hrthm.2007.03.036.

Bardy et al., 2005 (2005) 'New England Journal', *The New England journal of medicine*, 351(15), pp. 1493–1501. doi: 10.1056/NEJMoa1402685.

Bartos, D. C., Grandi, E. and Ripplinger, C. M. (2015) 'Ion Channels in the Heart.', *Comprehensive Physiology*. NIH Public Access, 5(3), pp. 1423–64. doi: 10.1002/cphy.c140069.

Bell, R. M., Mocanu, M. M. and Yellon, D. M. (2011) 'Retrograde heart perfusion:

The Langendorff technique of isolated heart perfusion', *Journal of Molecular and Cellular Cardiology*. Elsevier Ltd, 50(6), pp. 940–950. doi: 10.1016/j.yjmcc.2011.02.018.

Belles, B. *et al.* (1988) '"Run-down" of the Ca current during long whole-cell recordings in guinea pig heart cells: role of phosphorylation and intracellular calcium', *Pflügers Archiv European Journal of Physiology*. Springer-Verlag, 411(4), pp. 353–360. doi: 10.1007/BF00587713.

Beltrami, C. A. *et al.* (1995) 'The cellular basis of dilated cardiomyopathy in humans', *Journal of Molecular and Cellular Cardiology*. Academic Press, 27(1), pp. 291–305. doi: 10.1016/S0022-2828(08)80028-4.

Berecki, G. *et al.* (2010) 'Re-evaluation of the action potential upstroke velocity as a measure of the Na+ current in cardiac myocytes at physiological conditions.', *PloS one*, 5(12), p. e15772. doi: 10.1371/journal.pone.0015772.

Bers, D. M., Lederer, W. J. and Berlin, J. R. (1990) 'Intracellular Ca transients in rat cardiac myocytes: role of Na-Ca exchange in excitation-contraction coupling', *American Journal of Physiology-Cell Physiology*, 258(5), pp. C944–C954. doi: 10.1152/ajpcell.1990.258.5.C944.

Bioquest, A. (2018) *Fura-2-AM*. Available at: https://www.aatbio.com/products/fura-2-am-cas-1089.

Blinova, K. *et al.* (2018) 'International Multisite Study of Human-Induced Pluripotent Stem Cell-Derived Cardiomyocytes for Drug Proarrhythmic Potential Assessment', *Cell Reports*. Cell Press, 24(13), pp. 3582–3592. doi: 10.1016/J.CELREP.2018.08.079.

Bootman, M. D. *et al.* (2013) 'Ca2+-sensitive fluorescent dyes and intracellular Ca2+imaging', *Cold Spring Harbor Protocols*, 8(2), pp. 83–99. doi: 10.1101/pdb.top066050.

Brack, K. E. *et al.* (2013) 'The mechanical uncoupler blebbistatin is associated with significant electrophysiological effects in the isolated rabbit heart',

Experimental Physiology. Wiley-Blackwell, 98(5), pp. 1009–1027. doi: 10.1113/expphysiol.2012.069369.

Britton, O. J. *et al.* (2013) 'Experimentally calibrated population of models predicts and explains intersubject variability in cardiac cellular electrophysiology', *Proceedings of the National Academy of Sciences*. National Academy of Sciences, 110(23), pp. E2098–E2105. doi: 10.1073/pnas.1304382110.

Burton, F. L., McPhaden, A. R. and Cobbe, S. M. (2000) 'Ventricular fibrillation threshold and local dispersion of refractoriness in isolated rabbit hearts with left ventricular dysfunction', *Basic Research in Cardiology*, 95(5), pp. 359–367. doi: 10.1007/s003950070034.

Carmeliet, E. (1999) 'Cardiac Ionic Currents and Acute Ischemia: From Channels to Arrhythmias', *Physiological Reviews*, 79(3), pp. 917–1017. doi: 10.1152/physrev.1999.79.3.917.

Chappex, N. *et al.* (2015) 'Sudden cardiac death among general population and sport related population in forensic experience', *Journal of Forensic and Legal Medicine*, 35, pp. 62–68. doi: 10.1016/j.jflm.2015.07.004.

Chugh, S. S. *et al.* (2008) 'Epidemiology of Sudden Cardiac Death: Clinical and Research Implications', *Progress in Cardiovascular Diseases*, 51(3), pp. 213–228. doi: 10.1016/j.pcad.2008.06.003.

Cooper, J. *et al.* (2011) 'Considerations for the use of cellular electrophysiology models within cardiac tissue simulations', *Progress in Biophysics and Molecular Biology*. Elsevier Ltd, 107(1), pp. 74–80. doi: 10.1016/j.pbiomolbio.2011.06.002.

Coppini, R. *et al.* (2013) 'Late Sodium Current Inhibition Reverses Electromechanical Dysfunction in Human Hypertrophic Cardiomyopathy', *Circulation*. Lippincott Williams & WilkinsHagerstown, MD, 127(5), pp. 575–584. doi: 10.1161/CIRCULATIONAHA.112.134932.

Coulibaly, Z., Chen-Izu, Y. and Izu, L. T. (2017) 'Avoiding phantasms', *Cardiovascular Research*. Oxford University Press, 113(14), pp. 1703–1704. doi:

10.1093/cvr/cvx195.

Cubeddu, L. X. (2009) ‘Iatrogenic QT Abnormalities and Fatal Arrhythmias: Mechanisms and Clinical Significance’, *Current Cardiology Reviews*. Bentham Science Publishers, 5(3), pp. 166–176. doi: 10.2174/157340309788970397.

Davies, M. R. *et al*. (2012) ‘An in silico canine cardiac midmyocardial action potential duration model as a tool for early drug safety assessment’, *American Journal of Physiology - Heart and Circulatory Physiology*. doi: 10.1152/ajpheart.00808.2011.

Day, C. P., McComb, J. M. and Campbell, R. W. (1990) ‘QT dispersion: an indication of arrhythmia risk in patients with long QT intervals.’, *British heart journal*, 63(6), pp. 342–344. doi: 10.1136/hrt.63.6.342.

Dempster, J. (2016) *APsim*. Available at: https://github.com/johndempster/apsim/tree/master/.

Dessertenne, F. (1966) ‘Archives des maladies du coeur et des vaisseaux’, *Archives des maladies du coeur et des vaisseaux*, 59(2), pp. 263–72. Available at: http://www.ncbi.nlm.nih.gov/pubmed/4956181 (Accessed: 18 April 2019).

Dokos, S., Celler, B. and Lovell, N. (1996) ‘Ion currents underlying sinoatrial node pacemaker activity: A new single cell mathematical model’, *Journal of Theoretical Biology*. doi: 10.1006/jtbi.1996.0129.

Dou, Y., Arlock, P. and Arner, A. (2007) ‘Blebbistatin specifically inhibits actin-myosin interaction in mouse cardiac muscle’, *American Journal of Physiology-Cell Physiology*, 293(3), pp. C1148–C1153. doi: 10.1152/ajpcell.00551.2006.

Drici, M. D. and Clément, N. (2001) ‘Is gender a risk factor for adverse drug reactions? The example of drug-induced long qt syndrome’, *Drug Safety*, 24(8), pp. 575–585. doi: 10.2165/00002018-200124080-00002.

Efimov, I. R., Nikolski, V. P. and Salama, G. (2004) ‘Optical imaging of the heart’, *Circulation Research*, 95(1), pp. 21–33. doi:

10.1161/01.RES.0000130529.18016.35.

Faivre, J.-F. J. and Findlay, I. (1990) 'Action potential duration and activation of ATP-sensitive potassium current in isolated guinea-pig ventricular myocytes', *Biochimica et Biophysica Acta (BBA) - Biomembranes*. Elsevier, 1029(1), pp. 167–172. doi: 10.1016/0005-2736(90)90450-3.

Fast, V. G. (2005) 'Sensitive Dyes', *Electrophysiological Techniques*, pp. 233–255.

Fedorov, V. V. *et al.* (2007) 'Application of blebbistatin as an excitation-contraction uncoupler for electrophysiologic study of rat and rabbit hearts', *Heart Rhythm*, 4(5), pp. 619–626. doi: 10.1016/j.hrthm.2006.12.047.

Fedorov, V. V. (2010) 'Optical mapping of the isolated coronary-perfused human sinus node', 154(11), pp. 2262–2265. doi: 10.1016/j.pain.2013.06.005.Re-Thinking.

Fenichel, R. R. *et al.* (2004) 'Drug-Induced Torsades de Pointes and Implications for Drug Development', *Journal of Cardiovascular Electrophysiology*. John Wiley & Sons, Ltd (10.1111), 15(4), pp. 475–495. doi: 10.1046/j.1540-8167.2004.03534.x.

Findlay, I. *et al.* (1989) 'Effects of activation of ATP-sensitive K+ channels in mammalian ventricular myocytes', *American Journal of Physiology-Heart and Circulatory Physiology*. American Physiological Society, 257(5 Pt 2), pp. H1551–H1559. doi: 10.1152/ajpheart.1989.257.5.H1551.

Fluhler, E., Burnham, V. G. and Loew, L. M. (1985) 'Spectra, membrane binding, and potentiometric responses of new charge shift probes.', *Biochemistry*. United States, 24(21), pp. 5749–5755. doi: 10.1021/bi00342a010.

Fukano, T., Shimozono, S. and Miyawaki, A. (2008) 'Development of microscopic systems for high-speed dual-excitation ratiometric Ca2+imaging', *Brain Cell Biology*, 36(1–4), pp. 43–52. doi: 10.1007/s11068-008-9033-8.

Gibbons, W. R. and Fozzard, H. A. (1975) ‘Relationships between voltage and tension in sheep cardiac Purkinje fibers.’, *The Journal of general physiology*. Rockefeller University Press, 65(3), pp. 345–65. doi: 10.1085/JGP.65.3.345.

Gizak, A. *et al.* (2009) ‘Muscle FBPase is targeted to nucleus by its 203 KKKGK 207 sequence’, *Proteins: Structure, Function, and Bioinformatics*. John Wiley & Sons, Ltd, 77(2), pp. 262–267. doi: 10.1002/prot.22506.

Glukhov, A. V. *et al.* (2010) ‘Transmural Dispersion of Repolarization in Failing and Nonfailing Human Ventricle’, *Circulation Research*, 106(5), pp. 981–991. doi: 10.1161/CIRCRESAHA.109.204891.

Gong, J. Q. X. and Sobie, E. A. (2018) ‘Population-based mechanistic modeling allows for quantitative predictions of drug responses across cell types’, *npj Systems Biology and Applications*. Springer US, 4(1). doi: 10.1038/s41540-018-0047-2.

González, J. E. and Tsien, R. Y. (1997) ‘Improved indicators of cell membrane potential that use fluorescence resonance energy transfer’, *Chemistry and Biology*, 4(4), pp. 269–277. doi: 10.1016/S1074-5521(97)90070-3.

Grandi, E., Pasqualini, F. S. and Bers, D. M. (2010) ‘A novel computational model of the human ventricular action potential and Ca transient’, *Journal of Molecular and Cellular Cardiology*. doi: 10.1016/j.yjmcc.2009.09.019.

de Groot, J. R. *et al.* (2003) ‘Intrinsic heterogeneity in repolarization is increased in isolated failing rabbit cardiomyocytes during simulated ischemia.’, *Cardiovascular research*, 59(3), pp. 705–14. Available at: http://www.ncbi.nlm.nih.gov/pubmed/14499872 (Accessed: 26 April 2019).

Grunnet, M. (2010) ‘Repolarization of the cardiac action potential. Does an increase in repolarization capacity constitute a new anti-arrhythmic principle?’, *Acta Physiologica*. John Wiley & Sons, Ltd (10.1111), 198(SUPPL. 676), pp. 1–48. doi: 10.1111/j.1748-1716.2009.02072.x.

Grynkiewicz, G., Poenie, M. and Tsien, R. Y. (1985) ‘A new generation of Ca2+

indicators with greatly improved fluorescence properties.', *The Journal of biological chemistry*, 260(6), pp. 3440–50. Available at: http://www.ncbi.nlm.nih.gov/pubmed/3838314 (Accessed: 16 April 2019).

Herron, T. J., Lee, P. and Jalife, J. (2012) 'Optical imaging of voltage and calcium in cardiac cells & tissues', *Circulation Research*. NIH Public Access, 110(4), pp. 609–623. doi: 10.1161/CIRCRESAHA.111.247494.

Hodgkin, A. L. and Huxley, A. F. (1952) 'A quantitative description of membrane current and its application to conduction and excitation in nerve.', *The Journal of physiology*. Wiley-Blackwell, 117(4), pp. 500–44. Available at: http://www.ncbi.nlm.nih.gov/pubmed/12991237 (Accessed: 16 April 2019).

Hohnloser, S. H., van de Loo, A. and Baedeker, F. (1995) 'Efficacy and proarrhythmic hazards of pharmacologic cardioversion of atrial fibrillation: Prospective comparison of sotalol versus quinidine', *Journal of the American College of Cardiology*, 26(4), pp. 852–858. doi: 10.1016/0735-1097(95)00286-5.

Hondeghem, L. M., Carlsson, L. and Duker, G. (2001) 'Instability and Triangulation of the Action Potential Predict Serious Proarrhythmia, but Action Potential Duration Prolongation Is AntiarrhythmicHondeghem, L. M., Carlsson, L., & Duker, G. (2001). Instability and Triangulation of the Action Potential Pred', *Circulation*, 103(15), pp. 2004–2013. doi: 10.1161/01.CIR.103.15.2004.

Idriss, S. F. and Wolf, P. D. (2004) 'Transmural Action Potential Repolarization Heterogeneity Develops Postnatally in the Rabbit', *Journal of Cardiovascular Electrophysiology*. John Wiley & Sons, Ltd (10.1111), 15(7), pp. 795–801. doi: 10.1046/j.1540-8167.2004.03622.x.

Inada, S. *et al.* (2009) 'One-dimensional mathematical model of the atrioventricular node including atrio-nodal, nodal, and nodal-His cells', *Biophysical Journal*. doi: 10.1016/j.bpj.2009.06.056.

Jaiswal, A. and Goldbarg, S. (2014) 'Dofetilide induced torsade de pointes: Mechanism, risk factors and management strategies', *Indian Heart Journal*. Elsevier Ltd, 66(6), pp. 640–648. doi: 10.1016/j.ihj.2013.12.021.

Jensen-Urstad, K., Saltin, B. and Jensen-Urstad, M. (1997) 'Pronounced resting bradycardia in male elite runners is associated with high heart rate variability', *Scandinavian Journal of Medicine & Science in Sports*, 7(5), pp. 274–278. doi: 10.1111/j.1600-0838.1997.tb00152.x.

Jost, N. (2009) *Transmembrane ionic currents underlying cardiac action potential in mammalian hearts*. Available at: https://www.researchgate.net/publication/249962676 (Accessed: 30 May 2019).

Jou, C. J., Spitzer, K. W. and Tristani-Firouzi, M. (2010) 'Blebbistatin Effectively Uncouples the Excitation-Contraction Process in Zebrafish Embryonic Heart', *Cellular Physiology and Biochemistry*, 25(4–5), pp. 419–424. doi: 10.1159/000303046.

Kallergis, E. M. *et al.* (2012) 'Mechanisms, Risk Factors, and Management of Acquired Long QT Syndrome: A Comprehensive Review', *The Scientific World Journal*, 2012, pp. 1–8. doi: 10.1100/2012/212178.

Kannankeril, P. J. and Roden, D. M. (2007) 'Drug-induced long QT and torsade de pointes: recent advances', *Current Opinion in Cardiology*, 22(1), pp. 39–43. doi: 10.1097/HCO.0b013e32801129eb.

Kannankeril, P., Roden, D. M. and Darbar, D. (2010) 'Drug-Induced Long QT Syndrome', *Pharmacological Reviews*, 62(4), pp. 760–781. doi: 10.1124/pr.110.003723.

Kettlewell, S. (2002) *The electrophysiological and mechaniscal effects of gap junction uncoupling in cardiac tissue*. University of Glasgow.

Khairy, P. *et al.* (2014) 'PACES/HRS Expert Consensus Statement on the Recognition and Management of Arrhythmias in Adult Congenital Heart Disease', *Canadian Journal of Cardiology*, 30(10), pp. e1–e63. doi: 10.1016/j.cjca.2014.09.002.

Khairy, P. (2016) 'Ventricular arrhythmias and sudden cardiac death in adults with congenital heart disease', *Heart*, 102(21), pp. 1703–1709. doi:

10.1136/heartjnl-2015-309069.

Killeen, M. J. *et al*. (2007) 'Arrhythmogenic mechanisms in the isolated perfused hypokalaemic murine heart', *Acta Physiologica*, 189(1), pp. 33–46. doi: 10.1111/j.1748-1716.2006.01643.x.

Kolega, J. (2004) 'Phototoxicity and photoinactivation of blebbistatin in UV and visible light', *Biochemical and Biophysical Research Communications*, 320(3), pp. 1020–1025. doi: 10.1016/j.bbrc.2004.06.045.

Koller, M. L. *et al*. (2005) 'Altered Dynamics of Action Potential Restitution and Alternans in Humans With Structural Heart Disease', *Circulation*. Lippincott Williams & Wilkins, 112(11), pp. 1542–1548. doi: 10.1161/CIRCULATIONAHA.104.502831.

Koncz, I. *et al*. (2011) 'Electrophysiological effects of ivabradine in dog and human cardiac preparations: Potential antiarrhythmic actions', *European Journal of Pharmacology*. Elsevier, 668(3), pp. 419–426. doi: 10.1016/J.EJPHAR.2011.07.025.

Kornick, C. et al. (2003) 'QTc interval prolongation associated with intravenous methadone', *Pain*, 105(3), pp. 499–506. doi: 10.1016/s0304-3959(03)00205-7.

Kovács, M. *et al*. (2004) 'Mechanism of blebbistatin inhibition of myosin II', *Journal of Biological Chemistry*, 279(34), pp. 35557–35563. doi: 10.1074/jbc.M405319200.

Kriklerl, D. M. *et al*. (1976) 'Torsade de pointes, an atypical ventricular tachycardia', *British Heart Journal*. BMJ Publishing Group, 38(2), pp. 117–120. Available at: https://www.ncbi.nlm.nih.gov/pmc/articles/PMC482981/ (Accessed: 16 April 2019).

Kruppenbacher, J. P. *et al*. (1993) 'Cardiomyocytes of adult mice in long-term culture', *Naturwissenschaften*. Springer-Verlag, 80(3), pp. 132–134. doi: 10.1007/BF01131017.

Li, L. S. (2007) ‘Fluorescence probes for membrane potentials based on mesoscopic electron transfer’, *Nano Letters*. American Chemical Society, 7(10), pp. 2981–2986. doi: 10.1021/nl071163p.

Litovsky, S. H. and Antzelevitch, C. (1989) ‘Rate dependence of action potential duration and refractoriness in canine ventricular endocardium differs from that of epicardium: Role of the transient outward current’, *Journal of the American College of Cardiology*. Elsevier Masson SAS, 14(4), pp. 1053–1066. doi: 10.1016/0735-1097(89)90490-7.

Lou, Q., Li, W. and Efimov, I. R. (2011) ‘The role of dynamic instability and wavelength in arrhythmia maintenance as revealed by panoramic imaging with blebbistatin vs. 2,3-butanedione monoxime’, *American Journal of Physiology-Heart and Circulatory Physiology*, 302(1), pp. H262–H269. doi: 10.1152/ajpheart.00711.2011.

Louch, W. E., Sheehan, K. A. and Wolska, B. M. (2011) ‘Journal of Molecular and Cellular Cardiology Methods in cardiomyocyte isolation , culture , and gene transfer’, *Journal of Molecular and Cellular Cardiology*. Elsevier Ltd, 51(3), pp. 288–298. doi: 10.1016/j.yjmcc.2011.06.012.

Mahajan, A. *et al.* (2008) ‘A Rabbit Ventricular Action Potential Model Replicating Cardiac Dynamics at Rapid Heart Rates’, *Biophysical Journal*, 94(2), pp. 392–410. doi: https://doi.org/10.1529/biophysj.106.98160.

Maier, L. S., Bers, D. M. and Pieske, B. (2000) ‘Differences in Ca2+-handling and sarcoplasmic reticulum Ca2+-content in isolated rat and rabbit myocardium’, *Journal of Molecular and Cellular Cardiology*, 32(12), pp. 2249–2258. doi: 10.1006/jmcc.2000.1252.

Marelli, A. J. *et al.* (2014) ‘Lifetime prevalence of congenital heart disease in the general population from 2000 to 2010’, *Circulation*. doi: 10.1161/CIRCULATIONAHA.113.008396.

Maruyama, M. *et al.* (2011) ‘Genesis of phase 3 early afterdepolarizations and triggered activity in acquired long-QT syndrome’, *Circulation: Arrhythmia and*

Electrophysiology, 4(1), pp. 103–111. doi: 10.1161/CIRCEP.110.959064.

Matiukas, A. *et al.* (2006) 'New near-infrared optical probes of cardiac electrical activity', *American Journal of Physiology-Heart and Circulatory Physiology*. American Physiological Society, 290(6), pp. H2633–H2643. doi: 10.1152/ajpheart.00884.2005.

McComb, J. M., Campbell, N. P. S. and Cleland, J. (1984) 'Recurrent ventricular tachycardia associated with QT prolongation after mitral valve replacement and its association with intravenous administration of erythromycin', *The American Journal of Cardiology*. Elsevier, 54(7), pp. 922–923. doi: 10.1016/S0002-9149(84)80237-4.

McIntosh, M. A. *et al.* (1998) 'Action potential prolongation and potassium currents in left-ventricular myocytes isolated from hypertrophied rabbit hearts.', *Journal of molecular and cellular cardiology*, 30(1), pp. 43–53. Available at: http://www.ncbi.nlm.nih.gov/pubmed/9500863 (Accessed: 16 April 2019).

McIntosh, M. A., Cobbe, S. M. and Smith, G. L. (2000) 'Heterogeneous changes in action potential and intracellular Ca2+ in left ventricular myocyte sub-types from rabbits with heart failure', *Cardiovascular Research*. doi: 10.1016/S0008-6363(99)00360-0.

Meregalli, P. G. *et al.* (2006) 'Diagnostic value of flecainide testing in unmasking SCN5A-related Brugada syndrome', *Journal of Cardiovascular Electrophysiology*, 17(8), pp. 857–864. doi: 10.1111/j.1540-8167.2006.00531.x.

Miller, E. (2016) 'Small molecule fluorescent voltage indicators for studying membrane potential', *Curr Opin Chem Biol.*, pp. 74–80. doi: 10.1038/npg.els.0000182.

Miller, E. W. *et al.* (2012) 'Optically monitoring voltage in neurons by photo-induced electron transfer through molecular wires', *Proceedings of the National Academy of Sciences*, 109(6), pp. 2114–2119. doi: 10.1073/pnas.1120694109.

Mironov, S., Jalife, J. J. and Tolkacheva, E. G. (2008) ‘Role of conduction velocity restitution and short-term memory in the development of action potential duration alternans in isolated rabbit hearts’, *Circulation*, 118(1), pp. 17–25. doi: 10.1161/CIRCULATIONAHA.107.737254.

Molokhia, M. *et al.* (2008) ‘Case ascertainment and estimated incidence of drug-induced long-QT syndrome: Study in Southwest France’, *British Journal of Clinical Pharmacology*, 66(3), pp. 386–395. doi: 10.1111/j.1365-2125.2008.03229.x.

Monahan, B. P. *et al.* (1990) ‘Torsades de pointes occurring in association with terfenadine use.’, *JAMA*, 264(21), pp. 2788–90. Available at: http://www.ncbi.nlm.nih.gov/pubmed/1977935 (Accessed: 18 April 2019).

Morad, M. and Salama, G. (1979) ‘Optical probes of membrane potential in heart muscle.’, *The Journal of Physiology*. John Wiley & Sons, Ltd (10.1111), 292(1), pp. 267–295. doi: 10.1113/jphysiol.1979.sp012850.

Muszkiewicz, A. *et al.* (2016) ‘Variability in cardiac electrophysiology: Using experimentally-calibrated populations of models to move beyond the single virtual physiological human paradigm’, *Progress in Biophysics and Molecular Biology*. Elsevier, 120(1–3), pp. 115–127. doi: 10.1016/j.pbiomolbio.2015.12.002.

Myerburg, R. J. (2002) ‘Scientific gaps in the prediction and prevention of sudden cardiac death.’, *Journal of cardiovascular electrophysiology*, 13(7), pp. 709–23. doi: 10.1046/j.1540-8167.2002.00709.x.

Myerburg, R. J. and Junttila, M. J. (2012) ‘Sudden Cardiac Death Caused by Coronary Heart Disease’, *Circulation*, 125(8), pp. 1043–1052. doi: 10.1161/CIRCULATIONAHA.111.023846.

Myles, R. C. *et al.* (2010) ‘Effect of activation sequence on transmural patterns of repolarization and action potential duration in rabbit ventricular myocardium.’, *American journal of physiology. Heart and circulatory physiology*. American Physiological Society, 299(6), pp. H1812-22. doi: 10.1152/ajpheart.00518.2010.

Neher, E., Sakmann, B. and Neher, E. and Sakmann, B. (1976) ‘Single-channel currents recorded from membrane of denervated frog muscle fibres.’, *Nature*, 260(5554), pp. 799–802. Available at: http://www.ncbi.nlm.nih.gov/pubmed/1083489 (Accessed: 16 April 2019).

Ng, G. *et al.* (1998) ‘Non-uniform prolongation of intracellular Ca2+ transients recorded from the epicardial surface of isolated hearts from rabbits with heart failure’, *Cardiovascular Research*. Narnia, 37(2), pp. 489–502. doi: 10.1016/s0008-6363(97)00255-1.

Niemeijer, M. N. *et al.* (2015) ‘Pharmacogenetics of Drug-Induced QT Interval Prolongation: An Update’, *Drug Safety*. Springer International Publishing, 38(10), pp. 855–867. doi: 10.1007/s40264-015-0316-6.

O’Hara, T. *et al.* (2011) ‘Simulation of the Undiseased Human Cardiac Ventricular Action Potential: Model Formulation and Experimental Validation’, *PLOS Computational Biology*. Public Library of Science, 7(5), pp. 1–29. doi: 10.1371/journal.pcbi.1002061.

Okrainec, K., Banerjee, D. K. and Eisenberg, M. J. (2004) ‘Coronary artery disease in the developing world’, *American Heart Journal*, 148(1), pp. 7–15. doi: 10.1016/j.ahj.2003.11.027.

Olivari, M. T. *et al.* (1979) ‘Treatment of hypertension with nifedipine, a calcium antagonistic agent.’, *Circulation*, 59(5), pp. 1056–1062. doi: 10.1161/01.CIR.59.5.1056.

Orchard, C. H. (1985) ‘Intracellular calcium transients and developed tension in rat heart muscle. A mechanism for the negative interval-strength relationship’, *The Journal of General Physiology*, 86(5), pp. 637–651. doi: 10.1085/jgp.86.5.637.

Pinto, J. M. and Boyden, P. A. (1999) ‘Electrical remodeling in ischemia and infarction.’, *Cardiovascular research*, 42(2), pp. 284–97. Available at: http://www.ncbi.nlm.nih.gov/pubmed/10533567 (Accessed: 13 May 2019).

Pogwizd, S. M. *et al.* (2001) ‘Arrhythmogenesis and Contractile Dysfunction in Heart Failure’, pp. 1159–1167. doi: 10.1161/hh1101.091193.

Ponnaluri, A. V. S. S. *et al.* (2016) ‘Electrophysiology of Heart Failure Using a Rabbit Model: From the Failing Myocyte to Ventricular Fibrillation’, *PLoS Computational Biology*. Edited by A. D. McCulloch. Public Library of Science, 12(6), pp. 1–25. doi: 10.1371/journal.pcbi.1004968.

Prenner, S. B. *et al.* (2016) ‘Repolarization Heterogeneity: Beyond the QT Interval’, *Journal of the American Heart Association*. Wiley-Blackwell, 5(5), p. e003607. doi: 10.1161/JAHA.116.003607.

Priori, S. G. *et al.* (2016) ‘2015 ESC guidelines for the management of patients with ventricular arrhythmias and the prevention of sudden cardiac death’, *Russian Journal of Cardiology*, 135(7), pp. 5–86. doi: 10.15829/1560-4071-2016-7-5-86.

Pye, M. and Cobbe, S. M. (1996) ‘Arrhythmogenesis in experimental models of heart failure: the role of increased load’, *Cardiovascular Research*. Narnia, 32(2), pp. 248–257. doi: 10.1016/0008-6363(96)00080-6.

Reiffel, J. A. and Appel, G. (2001) ‘Importance of QT interval determination and renal function assessment during antiarrhythmic drug therapy’, *Journal of Cardiovascular Pharmacology and Therapeutics*. Sage PublicationsSage CA: Thousand Oaks, CA, 6(2), pp. 111–119. doi: 10.1177/107424840100600202.

Richardson, E. S. and Xiao, Y. (2010) ‘Electrophysiology of Single Cardiomyocytes: Patch Clamp and Other Recording Methods’, in *Cardiac Electrophysiology Methods and Models*. Boston, MA: Springer US, pp. 329–348. doi: 10.1007/978-1-4419-6658-2_16.

Roden, D. M. (2006) ‘Long QT syndrome: Reduced repolarization reserve and the genetic link’, *Journal of Internal Medicine*, 259(1), pp. 59–69. doi: 10.1111/j.1365-2796.2005.01589.x.

Rodríguez, B., Trayanova, N. and Noble, D. (2006) ‘Modeling cardiac ischemia.’,

Annals of the New York Academy of Sciences. NIH Public Access, 1080, pp. 395–414. doi: 10.1196/annals.1380.029.

Romero, L. *et al.* (2009) 'Impact of ionic current variability on human ventricular cellular electrophysiology', *American Journal of Physiology-Heart and Circulatory Physiology*, 297(4), pp. H1436–H1445. doi: 10.1152/ajpheart.00263.2009.

Ronzhina, M. and Cmiel, V. (2012) 'Application of the Optical Method in Experimental Cardiology : Action Potential and Intracellular Calcium Concentration Measurement Application of the Optical Method in Experimental Cardiology : Action Potential and Intracellular Calcium Concentration Mea', 8408(December), pp. 125–137.

Saegusa, N., Garg, V. and Spitzer, K. W. (2013) 'Modulation of ventricular transient outward K+ current by acidosis and its effects on excitation-contraction coupling', *American Journal of Physiology-Heart and Circulatory Physiology*, 304(12), pp. H1680–H1696. doi: 10.1152/ajpheart.00070.2013.

Sakamoto, T. *et al.* (2005) 'Blebbistatin, a myosin II inhibitor, is photoinactivated by blue light', *Biochemistry*, 44(2), pp. 584–588. doi: 10.1021/bi0483357.

Salama, G. (2005) 'Properties of New, Long-Wavelength, Voltage-sensitive Dyes in the Heart', *Journal of Membrane Biology*, 208(2), pp. 125–140. doi: 10.1007/s00232-005-0826-8.

Sarkar, A. X., Christini, D. J. and Sobie, E. A. (2012) 'Exploiting mathematical models to illuminate electrophysiological variability between individuals', *Journal of Physiology*, 590(11), pp. 2555–2567. doi: 10.1113/jphysiol.2011.223313.

Scanziani, M. and Häusser, M. (2009) 'Electrophysiology in the age of light', *Nature*, 461(7266), pp. 930–939. doi: 10.1038/nature08540.

Schaffer, P. *et al.* (1994) 'Di-4-ANEPPS causes photodynamic damage to isolated

cardiomyocytes', *Pflügers Archiv European Journal of Physiology*, 426(6), pp. 548–551. doi: 10.1007/BF00378533.

Schram, G. *et al.* (2002) 'Differential distribution of cardiac ion channel expression as a basis for regional specialization in electrical function', *Circulation Research*, 90(9), pp. 939–950. doi: 10.1161/01.RES.0000018627.89528.6F.

Schwartz, P. J., Woosley, R. L. and Woosley, R. L. (2016) 'Predicting the Unpredictable: Drug-Induced QT Prolongation and Torsades de Pointes', *Journal of the American College of Cardiology*, 67(13), pp. 1639–1650. doi: 10.1016/j.jacc.2015.12.063.

Selzer, A. and Wray, H. W. (1964) 'Quinidine Syncope: Paroxysmal Ventricular Fibrillation Occurring during Treatment of Chronic Atrial Arrhythmias', (July).

Shah, R. R. (2005) 'Drugs, QTc interval prolongation and final ICH E14 guideline: An important milestone with challenges ahead', *Drug Safety*, 28(11), pp. 1009–1028. doi: 10.2165/00002018-200528110-00003.

Shah, S. R., Park, K. and Alweis, R. (2019) 'Long QT Syndrome: A Comprehensive Review of the Literature and Current Evidence', *Current Problems in Cardiology*. Elsevier B.V., 44(3), pp. 92–106. doi: 10.1016/j.cpcardiol.2018.04.002.

Shannon, T. R. *et al.* (2004) 'A mathematical treatment of integrated Ca dynamics within the ventricular myocyte', *Biophysical Journal*. doi: 10.1529/biophysj.104.047449.

Shiels, H. A., Vornanen, M. and Farrell, A. P. (2002) 'The force-frequency relationship in fish hearts - A review', *Comparative Biochemistry and Physiology - A Molecular and Integrative Physiology*, 132(4), pp. 811–826. doi: 10.1016/S1095-6433(02)00050-8.

Sikkel, M. B. *et al.* (2017) 'Hierarchical statistical techniques are necessary to draw reliable conclusions from analysis of isolated cardiomyocyte studies', *Cardiovascular Research*, 113(14), pp. 1743–1752. doi: 10.1093/cvr/cvx151.

Skrzypiec-Spring, M. *et al.* (2007) 'Isolated heart perfusion according to Langendorff-Still viable in the new millennium', *Journal of Pharmacological and Toxicological Methods*, 55(2), pp. 113–126. doi: 10.1016/j.vascn.2006.05.006.

Smith, G. (1983) *A functional and structural study of cardiac muscle subjected to membrane disruption techniques.*, *PhD Thesis*. University of Glasgow.

Sobie, E. A. (2009) 'Parameter sensitivity analysis in electrophysiological models using multivariable regression', *Biophysical Journal*. Biophysical Society, 96(4), pp. 1264–1274. doi: 10.1016/j.bpj.2008.10.056.

Soyka, L. F., Wirtz, C. and Spangenberg, R. B. (1990) 'Clinical safety profile of sotalol in patients with arrhythmias', *The American Journal of Cardiology*, 65(2), pp. 74–81. doi: 10.1016/0002-9149(90)90207-H.

Taggart, P. *et al.* (2001) 'Transmural repolarisation in the left ventricle in humans during normoxia and ischaemia', *Cardiovascular Research*, 50(3), pp. 454–462. doi: 10.1016/S0008-6363(01)00223-1.

Terkildsen, J. R. *et al.* (2008) 'Using Physiome standards to couple cellular functions for rat cardiac excitation-contraction', *Experimental Physiology*, 93(7), pp. 919–929. doi: 10.1113/expphysiol.2007.041871.

Thermo Fisher Scientific (no date) *FluoVolt Membrane Potential Kit*.

Torp-Pedersen, C. *et al.* (1999) 'DOFETILIDE IN PATIENTS WITH CONGESTIVE HEART FAILURE AND LEFT VENTRICULAR DYSFUNCTION', *The New England Journal of Medicine*, 341(12), pp. 857–865. doi: 10.1056/NEJM199909163411201.

Trenor, B. *et al.* (2013) 'In silico assessment of drug safety in human heart applied to late sodium current blockers.', *Channels (Austin, Tex.)*. Taylor & Francis, 7(4), pp. 249–62. doi: 10.4161/chan.24905.

Tse, G. (2016) 'Mechanisms of cardiac arrhythmias', *Journal of Arrhythmia*. No longer published by Elsevier, 32(2), pp. 75–81. doi: 10.1016/J.JOA.2015.11.003.

Tse, G. *et al.* (2017) 'Electrophysiological mechanisms of long and short QT

syndromes', *IJC Heart and Vasculature*. The Authors, 14, pp. 8–13. doi: 10.1016/j.ijcha.2016.11.006.

Volders, P. G. a *et al.* (2000) 'Progress in the understanding of cardiac early afterdepolarizations and torsades de pointes: Time to revise current concepts', *Cardiovascular Research*, 46, pp. 376–392. doi: 10.1016/S0008-6363(00)00022-5.

Wang, D. Y. *et al.* (1988) 'Role of aiNa in positive force-frequency staircase in guinea pig papillary muscle', *American Journal of Physiology-Cell Physiology*. American Physiological Society Bethesda, MD , 255(6), pp. C798–C807. doi: 10.1152/ajpcell.1988.255.6.c798.

Wei, Y. *et al.* (2012) 'Lysophosphatidic acid increases the electrophysiological instability of adult rabbit ventricular myocardium by augmenting L-type calcium current.', *PloS one*. Edited by A. Guerrero-Hernandez, 7(9), p. e45862. doi: 10.1371/journal.pone.0045862.

Wickenden, A. et al D. *et al.* (1998) 'The role of action potential prolongation and altered intracellular calcium handling in the pathogenesis of heart failure', *Cardiovascular Research*, 37(2), pp. 312–323. doi: 10.1016/s0008-6363(97)00256-3.

Wokosin, D. L. L., Loughrey, C. M. M. and Smith, G. L. L. (2004) 'Characterization of a Range of Fura Dyes with Two-Photon Excitation', *Biophysical Journal*. Elsevier, 86(3), pp. 1726–1738. doi: 10.1016/S0006-3495(04)74241-1.

Wolska, B. M. and Solaro, R. J. (1996) 'Method for isolation of adult mouse cardiac myocytes for studies of contraction and microfluorimetry', *American Journal of Physiology-Heart and Circulatory Physiology*, 271(3), pp. H1250–H1255. doi: 10.1152/ajpheart.1996.271.3.H1250.

Woodford, C. (2015) 'Improved PeT Molecules for Optically Sensing Voltage in Neurons', *American Journal of Translational Research*, 8(5), pp. 2354–2364. doi: 10.1021/ja510602z.

Yang, T. *et al.* (2014) 'Screening for Acute I Kr Block Is Insufficient to Detect Torsades de Pointes Liability', *Circulation*, 130(3), pp. 224–234. doi: 10.1161/circulationaha.113.007765.

Zhou, Y.-Y. *et al.* (2000) 'Culture and adenoviral infection of adult mouse cardiac myocytes: methods for cellular genetic physiology', *American Journal of Physiology-Heart and Circulatory Physiology*, 279(1), pp. H429–H436. doi: 10.1152/ajpheart.2000.279.1.H429.

Zhu, R. *et al.* (2016) 'Variability of Action Potentials Within and among Cardiac Cell Clusters Derived from Human Embryonic Stem Cells', *Scientific Reports*. Nature Publishing Group, 6(November 2015), pp. 1–12. doi: 10.1038/srep18544.